UNIVERSIDAD DE CHILE
FACULTAD DE CIENCIAS FÍSICAS Y MATEMÁTICAS
DEPARTAMENTO DE INGENIERÍA ELÉCTRICA

AN ASTROMETRIC PRECISION LIMITATION STUDY USING AN ARTIFICIAL FAR-STELLAR FIELD EXPERIMENT

TESIS PARA OPTAR AL GRADO DE
MAGÍSTER EN CIENCIAS DE LA INGENIERÍA, MENCIÓN ELÉCTRICA

MEMORIA PARA OPTAR AL TÍTULO DE
INGENIERO CIVIL ELÉCTRICO

NÉSTOR NICOLÁS HENRÍQUEZ SEPÚLVEDA

PROFESOR GUÍA:
RENÉ MÉNDEZ BUSSARD

MIEMBROS DE LA COMISIÓN:
DIANA DULIC
MARIO GAI

Este trabajo ha sido parcialmente financiado por FONDECYT Nro. 1240049 y 12220984, FONDEQUIP Nro. EQM140055, y EQM180009, y la Agenzia Spaziale Italiana (ASI) mediante contrato 2018-24-HH.0 y su Addendum 2018-24-HH.1-2022 al Istituto Nazionale di Astrofisica (INAF) Italiano.

SANTIAGO DE CHILE
2024

RESUMEN DE LA TESIS PARA OPTAR AL GRADO DE
MAGÍSTER EN CIENCIAS DE LA INGENIERÍA, MENCIÓN
ELÉCTRICA Y MEMORIA PARA OPTAR AL TÍTULO DE
INGENIERO CIVIL ELÉCTRICO
POR: NÉSTOR NICOLÁS HENRÍQUEZ SEPÚLVEDA
FECHA: 2024
PROFESOR GUÍA: RENÉ MÉNDEZ BUSSARD

ESTUDIO DE LA LIMITACIÓN DE LA PRECISIÓN ASTROMÉTRICA MEDIANTE UN EXPERIMENTO DE CAMPO ESTELAR LEJANO ARTIFICIAL

En astrometría, el límite de precisión de un instrumento que observa un cuerpo celeste es fundamental. Para estudiar este concepto, se ha empleado un esquema de experimento previamente diseñado en el que se compara la *precisión astrométrica empírica* con el *límite teórico*. Además, se sugiere una modificación del experimento.

En primer lugar, se simuló un campo estelar lejano artificial. La localización de las fuentes luminosas puntuales se calculó utilizando cuatro algoritmos comúnmente mencionados en la literatura. El "límite inferior" se calculó utilizando fórmulas presentadas en estudios anteriores. Se realizó un análisis comparativo entre la precisión empírica y su límite teórico. La mejora propuesta para el experimento se implementó en una configuración para probar su rendimiento.

La localización de la estrella se calculó mediante los algoritmos propuestos; su precisión empírica presentó valores cercanos al límite estimado. Se observó que la señal acumulada de un objeto domina al límite inferior en proporcionalidad inversa, en condiciones de bajo fondo. En cuanto a la mejora propuesta, los resultados no fueron satisfactorios debido a la baja reflectancia de la fotomáscara.

Se investigó la relación entre la precisión empírica y su límite teórico. Se concluyó que la precisión máxima alcanzable puede estimarse utilizando información previa comúnmente disponible sobre el instrumento astronómico y el objeto celeste estudiado.

RESUMEN EN INGLÉS DE LA TESIS PARA OPTAR AL
GRADO DE MAGÍSTER EN CIENCIAS DE LA INGENIERÍA,
MENCIÓN ELÉCTRICA Y MEMORIA PARA OPTAR AL
TÍTULO DE INGENIERO CIVIL ELÉCTRICO
POR: NÉSTOR NICOLÁS HENRÍQUEZ SEPÚLVEDA
FECHA: 2024
PROFESOR GUÍA: RENÉ MÉNDEZ BUSSARD

AN ASTROMETRIC PRECISION LIMITATION STUDY USING AN ARTIFICIAL FAR-STELLAR FIELD EXPERIMENT

In astrometry, the precision limit of an instrument observing a celestial body is fundamental. To study this concept, a previously designed experiment scheme was employed comparing *empirical astrometric precision* to *theoretical limit*. Also, a modification is suggested for the experiment.

First, an artificial far-stellar field was simulated. The location of point-like light sources were calculated using four algorithms commonly mentioned in the literature. The "Lower Bound" was calculated using formulas reported in previous studies. A comparative analysis was conducted between the empirical precision and its theoretical limit. The proposed improvement to the experiment was implemented in one setup to test its performance.

The star location was computed through the proposed algorithms; its empirical precision presented values near the estimated limit. It was observed that the accumulated signal of an object dominates the Lower Bound in inverse proportionality, under low background conditions. Regarding the proposed improvement, the results were not satisfactory due to the low reflectance of the photo-mask.

The relationship between empirical precision and its theoretical limit was investigated. It was concluded that the maximum attainable precision can be estimated by using commonly available prior information about the astronomical instrument and the celestial object under study.

Para todos y todas quienes ocupan o han ocupado un lugar en mi corazón y en mis pensamientos.

Acknowledgments

Después de tanto trabajo, esta la parte quizá más difícil. Dedicar unas palabras de agradecimiento a las personas, lugares, situaciones, y problemas que ayudaron a forjarme, quien logró llevar a cabo una tesis de un tema interesante y desafiante: usar la ingeniería para aportar un granito de arena a la astronomía.

Mis padres me enseñaron que primero va la familia y eso es lo que quiero reflejar. Mis padres, Néstor y Carmen, me apoyaron desde pequeño para cumplir mis sueños y mis hermanos, Javier y Aníbal, siempre estuvieron a mi lado para mostrarme que soy suficente a pesar de mis defectos. Ellos son quienes se llevan gran parte del crédito. Mis abuelos, tíos, tías, primos, y primas, con quienes compartir cada junta familiar me daba un respiro de las responsabilidades. También parte de mi familia y quizá quienes más inocentemente me apoyaron: mi perro Rigel y mis gatos Güiña y Adhara, que sin saberlo me sostenieron.

¿Qué habría sido de mi sin mis amigos y amigas? Los últimos años fueron difíciles, con problemas de salud y del corazón, pero quienes lograron mantenerme a flote tienen mi infinito agradecimiento y espero compartir más alegrías y tristezas con ustedes: Dani, Rodrigo, Sol, Leiva, Fran, Contre, Wolvi, Kari, Nico, Isi, Fran V., Alan, Adri, Martín, Pablo, Susana, Kevin, Richard, Valeska, Santiago, Maca, Maxi, Cote, Alfonso, Tabi,...

Luego están las personas que conocí en Turín, mis mentores Mario y Alberto se encargaron de hacerme sentir bienvenido y aceptado en un lugar donde todos son científicos con quienes fue un privilegio trabajar y compartir, también a veces fue intimidante. Además, con quienes logré formar una breve amistad, Federica, Samantha y Francesco, la vida en Italia fue menos solitaria y más enriquecedora con ustedes. Este lugar me ayudó a crecer y ver que la independencia y la libertad, son algo que se construye y por lo que vale la pena trabajar.

Como dije, también quiero agradecer a situaciones y problemas. Muchos dicen que las crisis son necesarias para superarnos y sacar lo mejor de cada uno. Quizá no lo habría logrado sin antes haber vivido estos malos momentos y sentir que debía haber algo más.

Finalmente, una de las personas más importantes en este proceso, mi profesor, mentor y maestro, René. Como profesor me enseñó a tomarme la investigación en serio, como mentor me mostró que soy una persona valiosa y como maestro me dio todas las oportunidades y herramientas que me llevaron a lograr mi meta. Su apoyo fue incondicional incluso cuando yo sentía que no lo merecía. También, Diana fue parte de mi formación y me apoyó en todas las ideas locas que tuve para esta tesis.

Table of Content

List of Tables

List of Figures

Chapter 1

Introduction

In the past century, the field of astronomy has benefited from the contributions of engineering, which has provided new instruments and constant improvements useful for research. These astronomy-related advancement of technology across various engineering disciplines is a recurring phenomenon. For instance, the development of optics has led to the creation of more sophisticated telescopes, while the evolution of electronics has allowed the employment of new detectors with specific astronomical requirements. This can be exemplified by the transition from the photographic plates to discrete electronic detectors, such as charge-coupled devices (CCD) and complementary metal-oxide-semiconductor (CMOS) detectors.

Before presenting the purpose of this thesis, it is necessary to provide a brief definition of astrometry. This branch of astronomy is concerned with the measurement of the positions and distances of celestial bodies. *"Astrometry is one of the oldest branches of astronomy"*[1] and is currently undergoing active development with the aim of expand our understanding of the cosmos. Astrometry has been instrumental in the advancement of various astronomical applications. These include the discovery of binary stars and the monitoring of minor celestial bodies in the solar system, such as asteroids.

1.1 Motivation

In every science and engineering problem, it is fundamental to account for the uncertainty of the quantities measured. In the field of astrometry, one of the most significant uncertainties is directly related to the *experimental astrometric precision*. This metric indicates the degree of precision achieved in the location measurement of celestial bodies based on astronomical observations, which may include artificial satellites, asteroids, planets, stars, and galaxies, among other objects.

Moreover, it is worth to inquire about the theoretical astrometric precision, particularly with regard to its limitations. The subject of study may be formulated as the following question:

"What is the best astrometric precision that is *theoretically* possible to achieve, knowing the telescope characteristics, the detection instrument capabilities, and the observational conditions?"

The aforementioned question is answered by the statistics field through the *Cramér-Rao Lower Bound* (CRLB), which may be interpreted as the best *theoretical astrometric precision* estimated from the detection process parameters. From an experimental standpoint, the *astrometric precision* may be estimated from a set of astronomical observations as the statistical standard deviation of a normal distribution, given by the measured astrometric location from the images captured by the detector. A comparison between the *theoretical* limit and the *experimental* precision will provide insight into the performance of the algorithms and methods used to compute the location of the studied celestial body in known conditions.

1.2 State of the Art

The concepts of "astrometric precision limit" and "experimental astrometric precision" have been addressed previously in many studies for decades, demonstrating their importance in astronomy. This makes it necessary to visit these studies to have an idea of the evolution of our actual understanding in this field, from theoretical and experimental points of view.

1.2.1 Astrometric precision theoretical limit

This section briefly discusses studies that have focused on providing a theoretical background for the astrometric precision limit.

- First, the article by Winnick (1986)[2] presents a seminal work that theoretically explores the two-dimensional Cramér-Rao bound as "a lower limit for the mean-squared error (MSE) of any unbiased position estimator." Concludes that the MSE depends separately on the signal and noise power, and their ratio. It also notes that systems dominated by Poisson noise (and statistics) typically exhibit this behavior.
- The next decade, Adorf (1996)[3] presents a fundamental study showing the application of the CR Minimum Variance Bound (MVB) theorem to predict minimum astrometric and photometric errors. This article shows a way to compute the CRLB, but it is not clear about the method or the quantities involved. As one of the first articles to present real applications, it is more of a suggestion for further investigation. It is also specified here that the Cramér-Rao MVB-theorem "is based on a stochastic model of the observational process", which is exploited in more recent studies, including this thesis.
- The articles by Méndez (2013, 2014)[4][5] investigate the one-dimensional digital detector case. Close-form equations are presented to estimate the CRLB for astrometric (and photometric in the second article) precision in the simplified case of one-dimensional

detectors. For the first article, two cases are of uttermost importance: for high (light source) signal and low background the CRLB goes as $F^{-}1$, and for the opposite case the CRLB goes as B/F^2; the author mentions that this behavior "should still hold in the 2D case." Apart from other issues related to photometry, two other astrometry-related conclusions of the second article must be mentioned. It is concluded that the astrometric precision is proportional to the signal-to-noise ratio of the (light) source, and that the precision may increase when the source location is close to the pixel boundaries. The latter point is not discussed in this thesis. Additionally, it is mentioned that the astrometric precision is quite sensitive to the background brightness.

- From a different perspective, the author in Echeverria (2016)[6], explores the Bayesian Cramér-Rao (BCR) lower bound and the gain in precision compared to the parametric Cramér-Rao (MCR). As it is mentioned in this study, the BCR takes advantage of the use of prior information, resulting in better precision for any scenario. However, the author warns that the BCR must be used with caution, as it has been reported in other studies that it can lead to biased results. The BCR is not addressed in this thesis, but stands out as an interesting perspective to be explored in another instance.

- The article by Bouquillon (2017)[7] is one of the most important for this thesis, as it provides close-form equations to estimate the CRLB in two-dimensional pixel arrays, extending the one-dimensional equations of Méndez (2013, 2014)[4][5]. Different scenarios are examined: "over-, well-, and undersampled pixel scales," and "bright and faint sources." Although the focus is on the astrometric precision limit for moving targets, the stationary case is also treated from a theoretical point of view, which in fact serves as support for this thesis.

1.2.2 Astrometric precision experiments

This section briefly discusses studies that have focused on characterizing the astrometric precision of experimental measurements.

- The first precedent for the experimental setup concept is found in the article by Gai (2001)[8]. This study explores the limits of astrometric precision in a controlled laboratory setting. The idea of creating an artificial far-stellar field as an array of point-like light sources is employed. An important point of the methodology, which is replicated in more recent studies including this thesis, is the use of barycentric coordinates to reduce the observed common-mode motions; this article also demonstrates its advantage. The experimental setup concept supports the design in future studies.

- A second study with a similar experimental concept is presented in the article by Yano (2006)[9]. Here the relative distances of artificial stars in the same focal plane are estimated. The focus was on exploring the correction of the optical distortion of the image by a "photon-weighted means of stars", which turned out to be effective in the astrometric context.

- More recently, San Martin (2021)[10] presented a study using the same experimental concept as this thesis, based on the work of Gai (2001)[8]. Different methods to compute the star locations are tested and compared. The technique of reducing the data with barycentric coordinates is restated. This study provides a starting point for future research in the field. Also, here a CMOS detector was used instead of a CCD, a change that had not been tested before.
- Another approach is presented in the article by Gai (2022)[11], where the experimental data is taken from the already publicly available database of the TESS mission. Here the focus was on investigating the "geometric limiting precision on stellar image location, in terms of CCD pixel fraction." The advantage of applying different tests to already available astronomical images from a well-known instrument, is demonstrated. Another highlight is that the author cites the work of Otero (2021)[12] to suggest that CMOS detectors are becoming an interesting alternative to CCDs due to their "slightly smaller pixels" and "better radiation tolerance".

1.2.3 Centering algorithms and estimators for astrometry

Here are presented studies that have addressed the issues of centering algorithms and the performance of different estimators.

- A seminal work was presented by Stone (1989)[13], in which the author explores various centering algorithms. The one-dimensional case for digital detectors is studied. The performance of different algorithms are compared and some conclusions are still guiding recent research in the field. The "Gaussian-fit centering algorithm" is reaffirmed as an adequate method for a wide range of scenarios. In addition, the process of thresholding images to suppress the background showed an improvement for the astrometric precision and is proposed to be used in different algorithms.
- A comparative study is presented by Lu (1993)[14]. The maximum-likelihood (ML) and two-dimensional Gaussian fitting by least squares (LS) are examined by their performance under different conditions. The advantages and disadvantages of each are described. A number of conditions for determining the best algorithms are mentioned, including the target star brightness and background characteristics.
- The study by Zhai (2011)[15] explores the "micro-pixel accuracy centroid displacement estimation." The author mentions the use of the pixel response function (PRF) to realistically characterize the digital detector behavior and demonstrates a method to calibrate a detector using laser metrology. In addition, it is suggested that these findings may be applied to high-precision astrometry.
- In the article by Lobos (2015)[16], the author investigates the performance of the LS estimator for astrometric observations using digital detectors. A close-form equation is provided to estimate the variance of the LS estimator, which is compared to the CRLB. An important point of this study is that it shows that the LS estimator is "efficient" under low SNR conditions, indicating that it "closely approximates the CRLB".

- In the study of Espinoza (2018)[17], the performance of weighted least-squares (WLS) and ML estimators for astrometry in digital detectors is investigated. Expressions for estimating the variance of WLS and ML estimators are derived, and their performance is compared. One important conclusion is that the ML estimator is "consistently optimal" for astrometry in a wide range of signal-to-noise ratio regimes, and it is therefore proposed that it should be the preferred estimator for high-precision applications.
- One of the last articles in this field was presented by Lin (2021)[18], who compared the Gaussian fitting algorithm with the use of an effective point spread function (ePSF). The author confirms that under certain conditions such as enough stars to adequately reconstruct the ePSF, this method outperforms the Gaussian fitting. However, also the Gaussian PSF is also found to be an adequate and practical model under a variety of scenarios, but certainly not always the best.

1.2.4 Other astrometric applications

Other applications related to astrometric precision have been reported in several articles. A particularly important issue in astrometry is related to GAIA, as mentioned in studies by Altmann (2014)[19], Holl (2010)[20], and Lindegren (2012)[21]. These studies provide a characterization of the astrometric precision from a practical standpoint for monitoring the GAIA satellite itself to the applying of processing techniques to the data collected by GAIA.

1.3 Hypothesis

"Under known conditions of the detection process of point-like light sources in an optical instrument, such as a telescope or similar, the empirical precision of its location approaches to the theoretical limit given by the Cramér-Rao Lower Bound."

The "known conditions" may be listed as the following:

1. Optical system characteristics: its geometry and optical characteristics, along with the light source wavefront, define the Point Spread Function. Here it is assumed a point-like source, and a circular aperture with known diameter.
2. Detection instrument capabilities: these are defined by the electronics and the configuration of the instrument. The known parameters are the following: Gain, Quantum Efficiency, Dark Current, Readout Noise, Pixel size, and Pixel array. All parameters are fixed.
3. Observational conditions: the light source itself defines in part how it is detected in the observation instrument. The Exposure time is the only condition actually known. The following are conditions assumed to be adequately estimated from the observations: Light source flux and Background. Finally, there are two conditions assumed to be negligible: Vibrations and Atmospheric perturbations.

1.4 General objective

Compare experimental astrometric precision and theoretical limit of unresolved point-like light sources on a digital detector with a bi-dimensional pixel array, for different exposure times with equivalent imaging parameters.

1.5 Specific objectives

1. Manufacture a photo-mask using optical lithography to create an array of point-like light sources and test its performance in the optical experiment.
2. Implement an optical experiment to acquire images of an artificial far-stellar field with unresolved point-like light sources.
3. Obtain distributions of star locations by analyzing different datasets of unresolved point-like light sources images.
4. Estimate the Cramér-Rao Lower Bound for the acquired images.

This thesis employs engineering principles to design, prepare, implement, and execute an optical experiment with the objective of expanding the understanding of the astrometric precision limitation from an empirical standpoint, specifically for point-like light sources. The analysis of the data obtained from the experiment is based on an astronomical instrumentation framework derived from astronomy and engineering.

To conduct the comparison between experimental precision and theoretical limit, it was necessary to obtain a sufficient quantity of images of the same point-like light sources, captured under known and controlled conditions. To achieve this, an artificial far-stellar field had to be simulated in order to capture its image with a CMOS detector. Subsequently, the images were processed by different algorithms to determine the location of the simulated stars, which yielded an *experimental astrometric precision*. Conversely, the CRLB was required for each simulated star. This could be estimated using the same observations to determine the necessary quantities, apart from the known optics and electronics characteristics of the experiment. The required prior information to compute the CRLB was in fact available.

The concept behind this optical experiment was not novel; however, an improvement was proposed and tested. This involved the use of a photo-mask manufactured by optical lithography as target mask, which simulated the far-stellar field.

1.6 Overview

The thesis is divided into three topics and the conclusions: “Photo-mask fabrication” is presented in Chapter 2, “Optical Experiment” is presented in Chapter 3, “Astrometric precision limitation” is presented in Chapter 4, and “Conclusions” is presented in Chapter 5.

Chapter 2 presents the design and manufacturing process of the proposed photo-mask. This chapter commences with a statement of purpose and a concise overview of the field of optical lithography and its applications. Subsequently, the "Methodology" section enumerates the requisite equipment and the laboratory protocols that were followed. The "Results" section presents a summary of the characteristics and quality of the photo-masks fabricated, as well as the optimal fabrication parameters derived from the calibration processes. The "Discussion" section provides a concise overview of the fabrication process and the anticipated utility of the obtained results for this study.

Chapter 3 provides a comprehensive account of the images capturing process from the optical experiment. This chapter initiates with a contextualization. The "Experiment Design" section delineates the conceptual framework and enumerates the constituent elements. The "Experiment configuration: optical setup" section provides a detailed account of the three distinct experimental setups employed. The "Experiment configuration: controller" section provides an overview of the system controller concept and details the image acquisition parameters. In the "Results" section, a representative image of each setup is presented to illustrate the kind of images to be processed in the subsequent chapter. Finally, the "Discussion" section provides a brief qualitative description of the quality of the images obtained from the results, with a particular focus on their utility for the purpose of this study.

Chapter 4 contains all the research based on the data from the previous chapter and the underlying theoretical framework of the astrometric precision limitation concept. First, a definition of astrometry is provided, followed by the definition of related concepts. The "Methodology" section describes in detail the methodology employed in processing the data, delineating the specific steps undertaken, from the preparation of the images to the algorithms utilized for determining the star locations, including the method employed to estimate the CRLB. The "Results" section initiates presenting the analysis parameters employed across all datasets. Thereafter, the star location distributions are presented, accompanied by the estimations of the CRLB. The most important results are the distributions standard deviation, here namely "precision", and their comparison to the CRLB. The "Discussion" section presents a comprehensive analysis of the results.

Chapter 5 presents the conclusions, proposed improvements for future developments, and potential applications of each chapter. Additionally, a potential application of the methodology concept employed is presented.

Chapter 2

Photo-mask fabrication

In this astrometric precision limit study, optical lithography technology was employed to investigate a novel approach to far-stellar field simulation. The superior fabrication resolution and precision of the photo-masks enabled the creation of artificial point-like light sources with a diameter of 2 μm or less, offering a significant advantage over mechanical methods such as material removal. These custom-made photo-masks were intended to be used in the optical experiment described in Chapter 3, to create an artificial far-stellar field. The latter was expected to be seen as a set of point-like light sources by a CMOS detector. This objective served as the driving force behind the fabrication target specifications, because it promised a practical solution to create a custom device for a fundamental part of the optical experiment.

2.1 The Optical Lithography Technology

The *Photo-lithography*, or *Optical Lithography* as it is often referred to in the literature, is a modern fabrication technique that has gained considerable recognition within the semiconductor industry. It is employed extensively in the manufacturing of micro- and, more recently, nano-structures, primarily for the production of silicon-based electronic chips from crystalline silicon wafers.[22]

It is important to note that there are several fundamental aspects of photo-lithography that are crucial to the fabrication process of the photo-masks utilized in this study. Therefore, it is essential to have a clear understanding of these aspects before examining the results of this chapter. The following section introduces concepts that are commonly encountered in the context of optical systems, including resolution and depth of focus. In addition, two main parameters must be considered: "defocus" and "dose" are defined and explained, as they are fundamental to the exposure step. But first, two main applications of this technology are briefly explored in order to demonstrate the impact of photo-lithography and to justify its suitability for this experiment. Furthermore, it is shown why this technology is worthy of further investigation in the context of an astrometry study.

2.1.1 Applications

- Silicon chips and photo-masks: the semi-conductor industry is a highly growing field, which is demonstrated by the interest of manufacturers like Intel and Samsung to innovate in this area. In the SPIE article *Chip manufacturers discuss advanced lithography challenges and solutions*, is mentioned that "We're on track to hit a trillion transistors in a packaged product by 2030" and "That projection for at least a 10-fold increase is in line with the historic trend...".[1] The photo-mask, is the "printing master plate on the photo-lithography process", which is used to mass produce the semi-conductor chips from scratch.[23]
- Micro-fluidic structures: different science applications have been proposed and studied in the last few years for micro-fluidic structures made with, but not limited to, photo-lithography techniques. One of the most important applications, the "lab-on-chip" technology is actively being developed, as is treated in the Springer review article: "Microfluidic chips: recent advances, critical strategies in design, applications and future perspectives".

These two examples show the scientific potential of the (optical) lithography and inspired the idea to use it as fabrication process for a fundamental part of the optical experiment: the photo-mask.

2.1.2 Primary parameters

- Defocus: the longitudinal distance between the focal length of the system and the projection surface. Calibration of this parameter is one of the two steps required in the exposure process. In more precise terms, in Mack (2006)[24] the author describes the defocus effect as an "optical aberration". This effect can be described by the Optical Path Difference (OPD), which is a phase error between the ideal wavefront and the resulting wavefront on the surface of the exposed substrate. The OPD can be calculated as follows: $OPD = \delta(1 - \cos\theta) \approx \frac{1}{2}\delta \sin\theta^2$ (for small angles), where θ indicates the position at the exit pupil of the projection lens and δ indicates the defocus.
- Dose: power of the laser projected onto the substrate photo-resist. It is one of the two parameters that must be calibrated during the exposure step. In more precise terms, again, in Mack (2006)[24] the author defines the (Exposure) Dose or Exposure Energy as *"The amount of energy (per unit area) that the photo-resist is subjected to upon exposure by a lithographic exposure system. For optical lithography it is equal to the light intensity times the exposure time. Also called the exposure dose, or simply dose."* It is measured in millijoules per squared centimeter (mJ/cm^2).
- Resolution: every optical system that forms an image is characterized by this parameter. It indicates the ability of the system to resolve or differentiate two objects. In the context of photo-lithography, resolution refers to the ability of the projected light to expose the resin with a high degree of precision. It is mainly defined by the wavelength

[1] Article accessed on the SPIE webpage, on 13 March 2024.

of the light source due to the diffraction.[22] The concept of resolution will be redefined in greater detail within the context of astrometry in Chapter 4.

- Depth of Focus (DoF): as the author explains it in Naulleau (2019)[22], *"the DOF can be defined as the longitudinal distance over which the change in size of a single image point is less than or equal to the minimum size of the image point as set by the diffraction limit."* In this context, the DoF is contingent upon the internal system configuration and cannot be altered directly. However, it is possible that the results may be influenced by the thickness of the photo-resin layer.

2.2 Methodology

The photo-mask fabrication was expected to be a fundamental handwork part of this study and a novel approach to create a custom part that enables the projection of an artificial far-stellar field with the proper equipment. Here are listed all the equipment and supplies needed for the fabrication process, as well as the fabrication processes followed to achieved the desired specifications.

2.2.1 Clean Room Equipment and Supplies

This section lists the required equipment and supplies, the details are in Appendix A.1.1.

- Clean Room
- Maskless Aligner
- Glass Plates
- Substrate Cutting Tool
- Tweezers
- Laboratory Flasks
- Containers
- Compressed air
- Deionized Water
- Developer: Sodium Hydroxide
- Chromium Etchant
- Microscope

2.2.2 Fabrication Protocols

The fabrication procedure for photo-masks involved four distinct processes: Exposure, Development, Etching and Check. Each of these steps are described in detail in Appendix A.1.2, in accordance with established laboratory protocols. Prior to the first step, the target design to imprint on the photo-mask must be in a *.dxf* file created in a CAD software, such as AutoCAD.

Photo-mask check

The photo-masks final result must be checked before proceeding with the experiment. To accept a photo-mask sample, its quality can be described by three requisites:

1. No scratches on the usable surface area.
2. Transparent holes homogeneity, i.e. same diameters and distances.
3. Chromium layer surface homogeneity, i.e. reflectance homogeneity.

In this step, the microscope at the Micro-fabrication Laboratory was used to check the three requisites mentioned above by visual inspection.

2.2.3 Protocols Calibration

The optical lithography process employed to fabricate the photo-masks comprises a series of distinct steps, some of which are inherently chemical in nature. This aspect implies that some parameters, such as chemical concentrations and exposure times, among others, had to be adjusted through a process of trial and error, or calibration. Each of the three protocols utilized required at least one step to be calibrated. The procedures detailed in Appendix A.1.3 describe the specific calibration methods used to adjust the parameters required in each protocol.

Exposure

The exposure process employs the use of the MLA machine to direct a 535-nanometer wavelength laser onto the raw mask. The parameters to calibrate for this process are the *Defocus* and *Dose*, explained in 2.1.2. A standard calibration process, commonly used in optical lithography laboratories, was used before beginning with the photo-masks fabrication. The calibration process followed is detailed in Appendix A.1.3.

The values ranges used in the dose/defocus test are presented in the Table 2.1. The parameters selected in this test were based on recommendations by other laboratory users, with the middle step (Dose: 75 mJ/cm^2 and Defocus: 0) being the most probable successful setup.

Table 2.1: A large range was tested for the Dose series, with the initial recommended guess of 90 mJ/cm^2. The Defocus was centered in 0, there was expected to need no different values.

	Dose	Defocus
Series	30 to 120 mJ/cm^2	-3 to 3
Step Size [X/Y]	6 mm	6 mm
Steps	7	7
Step change	15 mJ/cm^2	1

Development

The development process uses the Developer chemical solution to remove the exposed photoresist; in this study, the Developer used was a Sodium Hydroxide solution (NaOH). The developer must be at the proper concentration to leave enough time to safely develop the substrate. In this process, there is one variable to be calibrated: the development time. This variable is dependent on the developer concentration: lower concentration leads to longer development times. The specific steps followed to calibrate the time variable are presented in the appendix A.1.3.

Three different NaOH developer concentration were tested: 1.5%, 1.0% and 0.8%. A development time of 10 seconds was the target of this calibration.

Etching

The Etching process uses the Chromium Etchant, an acidic solution with the property of removing metals like Chromium, Gold and Copper. Because of its known Etch Rate of 40 Å/s, the etching time is previously known from the laboratory recipe for this specific substrate; its chromium layer thickness is 1100 Å, as seen in A.1.1. No calibration is needed in this case, an etching time between 30 and 35 seconds was enough to completely remove the chromium film in the exposed area. Longer etching times may result in chromium removal of non targeted areas.

2.3 Results

2.3.1 Protocols Calibration

The following results demonstrate the tests conducted to identify the optimal values for each adjusted step.

Exposure

As it is seen in Table 2.1, seven Dose series and seven Defocus series were tested, reaching a total of forty nine different exposures. Figure 2.1 illustrates a diagram representing the pattern array with its different dose/defocus parameters exposed to a raw plate, colored correspondingly to the qualitative result observed; red: not usable, yellow: usable but not ideal, green: good result.

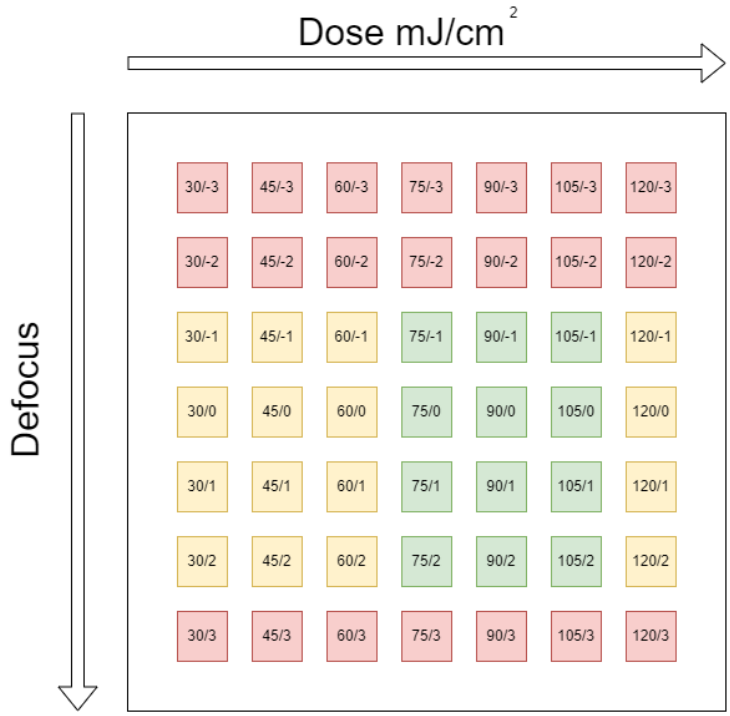

Figure 2.1: Each small square represents one sample pattern iteration with a unique pair of dose and defocus parameters. The dose increases to the right and the defocus increases to the bottom.

The patterns exposed were observed using the integrated camera of the MLA. The camera is capable of obtaining images to visually inspect the exposed area without further treatment of the glass plate. Figure 2.2 illustrates a part of the exposed pattern for the area with 90 mJ/cm^2 Dose and 0 Defocus.

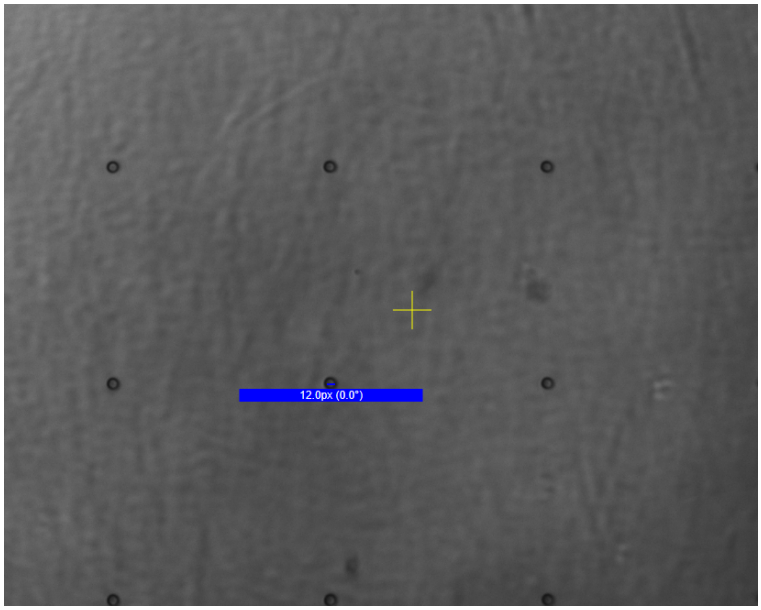

Figure 2.2: A part of the plate exposed area using 90 mJ/cm^2 Dose and 0 Defocus.

Finally, a configuration of 90 mJ/cm^2 Dose and 0 Defocus was selected, based on the Figure 2.1 diagram. The green zone indicates twelve possible choices, but just one was needed. In case that the subsequent development process did not result in a good mask, eleven more choices were able to be tested.

Development

Following the steps described in A.1.3, different development times were tested with a NaOH developer concentration at 1.5%. The parameters used and the corresponding results are presented in Table 2.2 and the developed glass plate is illustrated in Figure 2.3.

Table 2.2: Glass Plates after exposure and development. NaOH Developer at 1.5%.

Sample N°	Time [s]	Observed result
1	10	Correctly developed
2	2	Underdeveloped
3	12	Overdeveloped
4	8	Partially developed

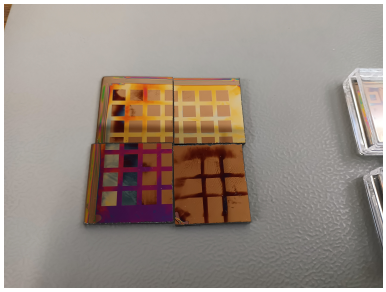

Figure 2.3: Each pattern iteration uses the same dose/defocus parameters, the only change is the development time. There is no pattern in each iteration but a simple plane.

Secondly, along with the dose/defocus calibration, the development time calibration was tested again to fine tune the exact value with a NaOH developer concentration at 1.0 %. The results are presented in Table 2.3.

Table 2.3: Glass Plates after exposure and development. NaOH Developer at 1.0 %. The sample N°2 was developed for a time slightly shorter than 10 s.

Sample N°	Time [s]	Observed result
1	10	Overdeveloped
2	10(-)	Underdeveloped
3	8	Underdeveloped
4	9	Underdeveloped

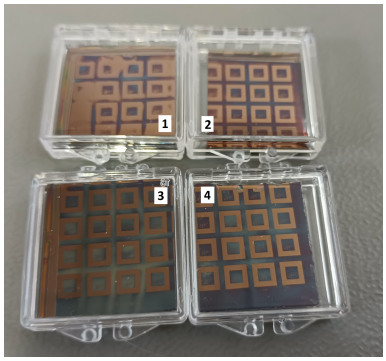

Figure 2.4: Each pattern iteration uses the same dose/defocus parameters, the only change is the development time. Each square have a sample pattern that must be checked under a microscope.

A third calibration process was conducted in the same way as the second one. With a NaOH developer concentration at 0.8 %. The results are presented in Table 2.4.

Table 2.4: Glass Plates after exposure and development. NaOH Developer at 0.8 %.

Sample N°	Time [s]	Observed result
1	9	Partially underdeveloped
2	11	Partially overdeveloped
3	12	Overdeveloped
4	10	Correctly developed

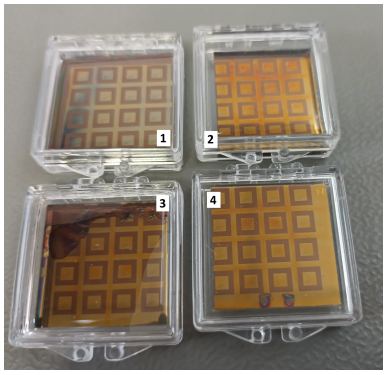

Figure 2.5: Each pattern iteration uses the same dose/defocus parameters, the only change is the development time. Each square have a sample pattern that must be checked under a microscope.

After the three calibration iterations, the inspected masks showed that using the NaOH developer at 0.8 % and 10 seconds, the development achieved an acceptable outcome.

2.3.2 Approved Photo-masks

After the fabrication parameters calibration, a series of masks were manufactured. Some iterations failed due to manipulation mistakes, inaccurate development and etching times, and the unavoidable randomness in the chemical fabrication steps. Six different designs were made, giving multiple choices for the Optical Experiment to be tested.

Test Design

The first design here illustrated is a test design. Circles with different diameters were made on a raw mask to test the capabilities of the fabrication process. Under the microscope, it was possible to verify diameters and homogeneity. Figure 2.6 illustrates one of the same patterns used for the protocols calibrations.

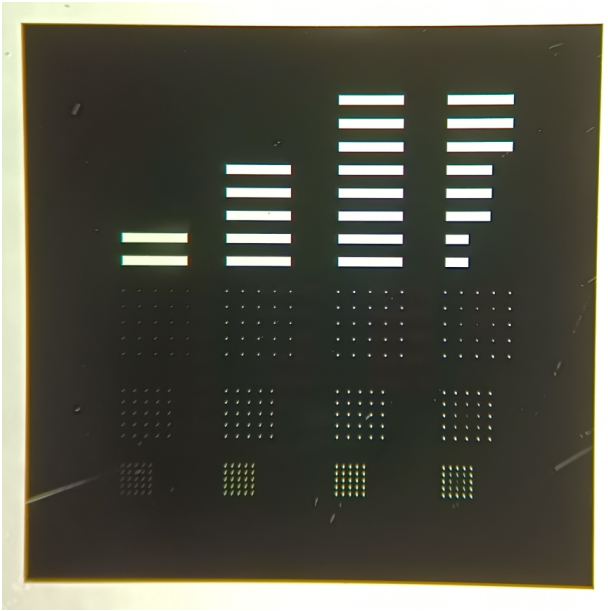

Figure 2.6: In this design are presented, from left to right, transparent circles with diameters of: 2 μm (first column), 5 μm (second column), 10 μm (third column), and the previous three sizes in the same arrays (fourth column). Also, the bars at the top are used as markers to visually verify the exposure, development and etching processes.

Mask 1

A full image of the design is illustrated in Figure A.5 as well as the zoomed image in Figure A.6. The latter presents the transparent points and leaves out the alignment marks. Table 2.5 presents the transparent circles diameters.

Table 2.5: Each array contains 25 circles with equal diameters and equally spaced in a matrix-like shape by 100 μm center-to-center. The number of array goes from bottom to top and from left to right.

Array number	Circles diameter [μm]
1	4
2	8
3	12
4	16
5	20
6	24
7	28
8	32
9	36

Mask 2

A full and a zoomed image of the design are illustrated in Figures A.7 and A.8, respectively. The latter illustrates the transparent points and leaves out the alignment marks.

Table 2.6: Mask 2 parameters. Each array contains 25 circles with equal diameters and equally spaced in a matrix-like shape by 200 μm center-to-center. The number of array goes from bottom to top and from left to right.

Array number	Circles diameter [μm]
1	4
2	8
3	12
4	16
5	20
6	24
7	28
8	32
9	36

Mask 3

A full image of the design is illustrated in Figure A.9.

Table 2.7: Each array contains 9 circles with equal diameters and equally spaced in a matrix-like shape by 2000 μm center-to-center. The number of array goes from bottom to top and from left to right.

Array number	Circles diameter [μm]
1	2
2	4
3	6
4	8
5	10
6	12
7	14
8	16
9	18

2.4 Discussion

2.4.1 Fabrication Process

The fabrication process required specialized equipment: clean room, MLA machine, chromium etchant, glass plates with applied photo-sensitive resin and a chromium layer. The process was not straightforward due to the necessity of extensive calibration processes and time-consuming fabrication procedures. Nevertheless, the potential for custom designs and varying pinhole diameters justifies the resources invested in this preparatory stage of the study.

2.4.2 Photo-masks

The optical experiment presented in the following chapter required the minimum possible diameter for the pinhole. One potential alternative for the photo-mask was a metallic material like copper with drilled pinholes; this technique limited the diameter of the pinhole to a minimum of 60 μm. Conversely, as evidenced by the results of the test design in Figure 2.6, the optical lithography technique employing glass plates permitted the fabrication of photo-masks with pinhole diameters as small as 2 μm.

Mask 1 and Mask 2 share a common design concept: nine 25-pinhole arrays with identical diameters, the sole distinction between them being the varying distances between the pinholes. In the context of the optical experiment, this may result in the formation of artificial stars with a similar brightness but differing distances between them.

Mask 3 followed a slightly different design: nine 9-pinhole arrays with identical diameters and larger pinhole distances of 2000 μm. This results in a larger area to be seen by the detector in the optical experiment.

Chapter 3

Optical Experiment

The second phase of this study consisted of the preparation and execution of the optical experiment. The "Osservatorio Astrofisico di Torino" hosted the experiment within its facilities located in Pino Torinese, Piedmont, Italy.

The primary objective of this experiment was to obtain multiple images of a set of unresolved point-like light sources under controlled conditions, including a stable atmosphere (free from turbulence) and a stable support structure (free from vibrations). The light sources were distinguished by their wavelength, which was identical for all of them. The array of multiple point-like light sources in the experiment was designed to serve as an analog of a far-stellar field observed by a telescope. Two approaches were employed to create the simulated stars: the use of a circular opaque metallic piece with holes and the glass plate with an opaque chromium layer. The fabrication process of the latter was described in Chapter 2.

A secondary objective of this experiment was to test the second approach, which represented a novel idea never previously employed in the laboratory. This approach differed from the first approach, which had been previously utilized in other studies, including those conducted in San Martin (2020)[10].

The Experiment Design section provides a comprehensive account of the components utilized in the experiment, including both hardware and software. The hardware consisted primarily of off-the-shelf components, with the exception of the glass plate photo mask, which was custom-made. A specialized software program was developed to operate the detector using a dedicated computer. The Experiment Configuration section is divided into two subsections. The first subsection is devoted to the optical setup, while the second subsection is dedicated to the control concept. Subsequently, the Image Acquisition Parameters section provides a summary of the configuration utilized by the detector to acquire all images of the artificial far-stellar field. The Results section presents a selection of acquired images to illustrate the data to be analyzed in Chapter 4. Finally, in the Discussion section, the utility of the results is evaluated through a brief qualitative analysis.

3.1 Experiment Design

The data necessary to ascertain the astrometric precision limit was obtained through the experiment here detailed. An artificial optical far-stellar field was created in a laboratory setting on an insulated optical bench. Figure 3.1 illustrates a schematic of the general setup. It must noted that the positions of the aperture lens, objective lens, and CMOS detector remained fixed throughout the acquisition of all images.

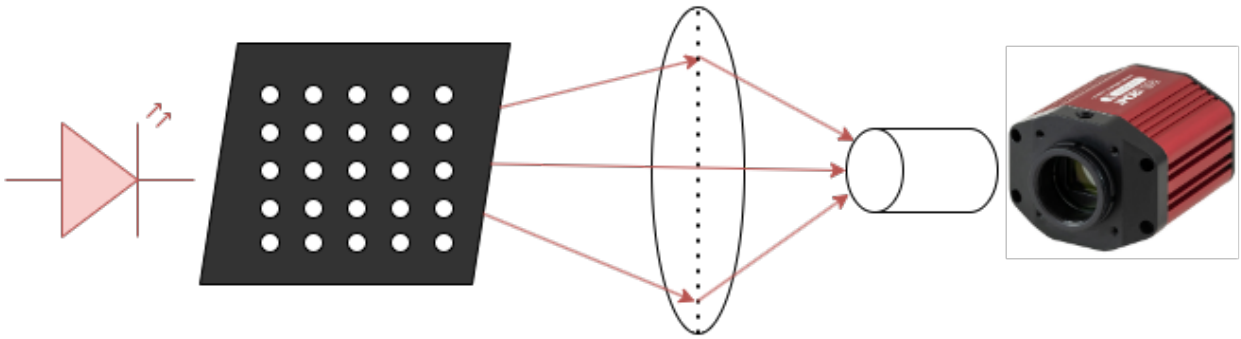

Figure 3.1: from left to right are: light source, photo-mask, aperture lens, objective lens, and CMOS detector.

3.1.1 Hardware components and instruments

This subsection presents a list of the hardware components and instruments, accompanied by the most relevant specifications. More details are presented in Appendix B.1.1.

Light Source

Two ThorLabs mounted LEDs were utilized as light sources, independently. These provide a stable light output during the entire exposure time for each set of images. The pertinent specifications are indicated in the Table B.1 for the red LED ($\lambda = 625$nm)[25] and the Table B.2 for the white LED[26]. Figure B.1a illustrates the M625L4 mounted LED and Figure B.1b illustrates the MWWHL4 mounted LED.

LED Driver

The mounted LEDs require the use of a LED driver. In this instance, a ThorLabs T-Cube LED Driver model LEDD1B[27] was employed. This component provides a stable electrical current supply and an appropriate voltage to operate the LED. Table B.3 presents the technical specifications of the device, while Figure B.2 illustrates the LED driver.

Photo-mask

The first mask employed was the same used in San Martin (2020)[10] as was mentioned earlier. A set of 9 holes in the metallic surface let the light from the LED to pass trough, creating an artificial optical far-stellar field. The second mask employed was a glass plate. Actually, three different designs were tested and their specifications are detailed in the Chapter 2.

Aperture lens

A ThorLabs Achromatic Doublet AC508-400-A[28] was used in the aperture of the optical experiment. Its specifications are summarized in Table 3.1.

Table 3.1: Achromatic doublet specifications.

Specification	Value
Diameter	2in / 51.6mm
Focal length	f = 400mm

Objective lens

An objective lens $(1 : 5,6/30)$ was used to compensate the focal length difference and mitigate optical distortions.

CMOS Detector

A ThorLabs CS235MU CMOS Detector[29] was mounted at the right end. Figure B.3 illustrates the detector. Table B.4 details the sensor specifications and Table B.5 details the detector imaging specifications. The most relevant specifications are presented in the Table 3.2.

Table 3.2: CMOS detector parameters. More details in the appendix Tables B.4 and B.5.

Parameter	Value
Sensor type	CMOS Monochrome
Number of active pixels	1920 (H) X 1200 (V)
Pixel size	5.86 μm x 5.86 μm
Readout noise	$\leq$7.0 e^- RMS

3.1.2 Experiment controller

CMOS detector software

The CMOS Detector was initially controlled using "ThorCam," a scientific imaging software by ThorLabs which is sufficient to utilize the majority of its functionalities. The sole disadvantage is that it cannot be programmed to take a series of images with different parameters. Instead, it allows the user to take a single series of images with the same parameters, after which the task is completed and another one can be initiated. This presents a challenge for the study, which requires the acquisition of multiple images in varying configurations. To achieve this, it is necessary to manually set each series of images to be shot one after another. To address this issue, the ThorLabs Scientific Camera Interfaces, a comprehensive code package in various programming languages with dedicated Application Programming Interfaces (APIs), was employed to develop specialized software. A custom software application was developed in Python to facilitate the acquisition of the images displayed in the Results section. The program flow is illustrated in Figure 3.2.

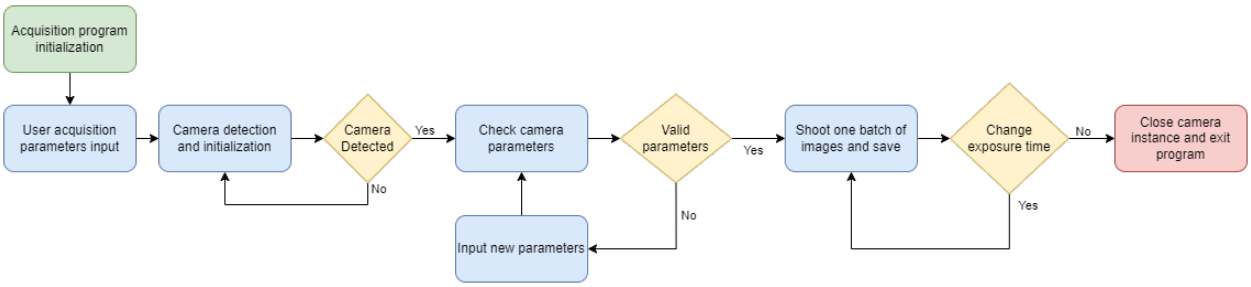

Figure 3.2: The program flow allows the user to take multiple batches of images with varying exposure times, using a single instruction from the controller computer. The actual implementation was developed in Python. A vertical presentation of this image is illustrated in Figure B.4.

Clean room computer

A laptop with Windows 10 operating system was utilized to manipulate the CMOS detector via a USB connection, employing the developed software. This computer is in compliance with the system requirements recommended by ThorLabs on their website. Furthermore, the laptop was connected to the local network of the Observatory via an Ethernet cable. Remote Desktop functionality within the Windows operating system was employed to facilitate remote manipulation of the computer from an office situated outside the clean room where the experiment was conducted.

3.2 Experiment Configuration: Optical Setup

This section presents three optical setups, each of which may yield different results in terms of final image quality. These setups follow to the same design concept illustrated in Figure 3.1, with minor variations.

3.2.1 Setup 1: Original Mask and Red Light

The first configuration aimed to replicate the results from a previous realization as seen in San Martin (2020)[10], where the mask was a circular opaque metallic piece with tiny holes that let the light pass through. The idea was to create an artificial far-stellar field using point-like light sources. As can be seen in Figure 3.3, the experiment components from left to right are:

1. Red LED M625L4.
2. Metallic photo-mask.
3. Aperture lens.
4. Objective lens.
5. CMOS Detector CS235MU.
6. Enclosure containing 1 and 2. 2 prevents that 1 contaminates with background light.

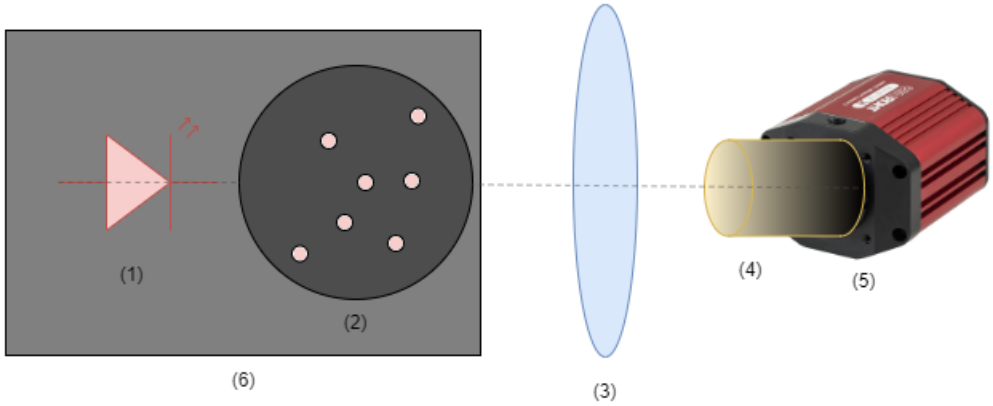

Figure 3.3: Metallic mask with red light experiment.

3.2.2 Setup 2: Original Mask and White Light

A second configuration was set, the only one change: a white LED was used instead of the red one. It was expected to have slightly different images because of the wider spectrum of the light source. Again, as can be seen in Figure 3.4, the experiment components from left to right are:

1. White LED MWWHL4.
2. Metallic photo-mask.
3. Aperture lens.
4. Objective lens.
5. CMOS Detector CS235MU.
6. Enclosure containing 1 and 2. 2 prevents that 1 contaminates with background light.

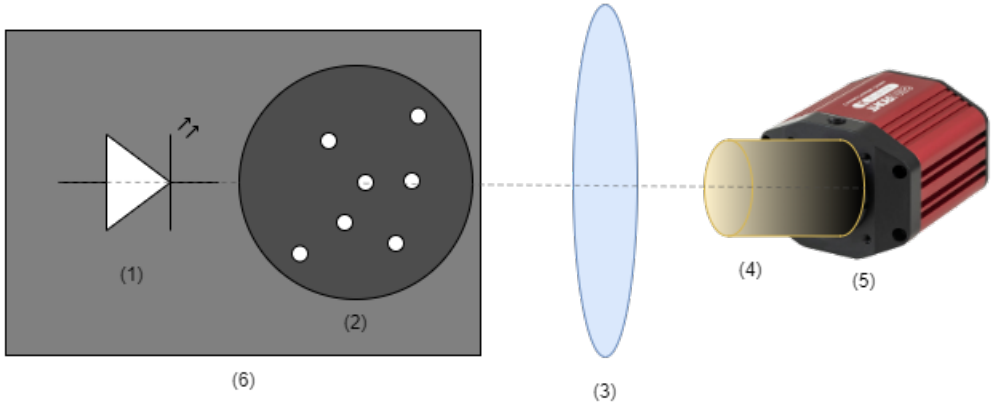

Figure 3.4: Metallic mask with white light experiment.

3.2.3 Setup 3: Glass-chromium mask and Red Light

Finally, the new custom-made photo-mask, composed of a glass plate with a reflective layer of chromium was set in the experiment using a red light source. Figure 3.5 illustrates the experiment setup and its components from left to right:

1. Red LED M625L4.
2. Glass plate photo-mask.
3. Aperture lens.
4. Objective lens.
5. CMOS Detector CS235MU.
6. Enclosure containing 1 and 2. 2 prevents that 1 contaminates with background light.

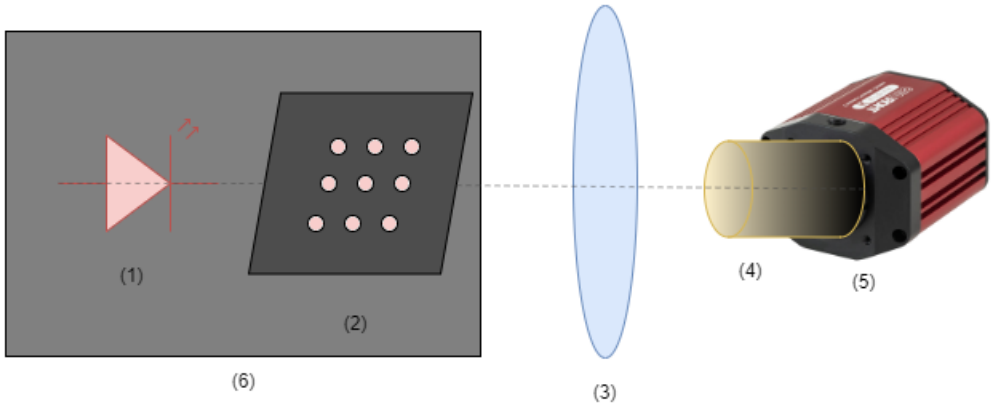

Figure 3.5: Glass-Chromium mask with red light experiment.

3.3 Experiment Configuration: Controller

The experiment was controlled by two components: LED Driver and CMOS PC Controller. A second PC was used from outside the Clean Room, this aimed to avoid physical perturbations to the experiment. Figure 3.6 illustrates the main components and the connections between, as listed below:

1. LED Light Source: corresponds to the M625L4 and MWWHL4 mounted LEDs for each configuration. Inside the Clean Room.
2. DC Current Source: supplies a constant electrical current to (1) that is set manually prior to acquire images. Corresponds to the LEDD1B LED Driver and it is inside the Clean Room.
3. CMOS Detector: corresponds to the CS235MU CMOS Detector, controlled by (4). Inside the Clean Room.
4. CMOS Controller PC: corresponds to a laptop connected to the CMOS Detector. Execute the CMOS Detector controller software and sends the instructions to shot images and acquire the data from the CMOS detector. Sends the images to (5) and is located inside the Clean Room.
5. Remote PC: corresponds to the user PC. Connected to (4) through a local area network (LAN) connection, and a VPN if needed from outside the Observatory; sends the instructions to execute the CMOS Controller software and receives the images acquired. Located at a remote office.

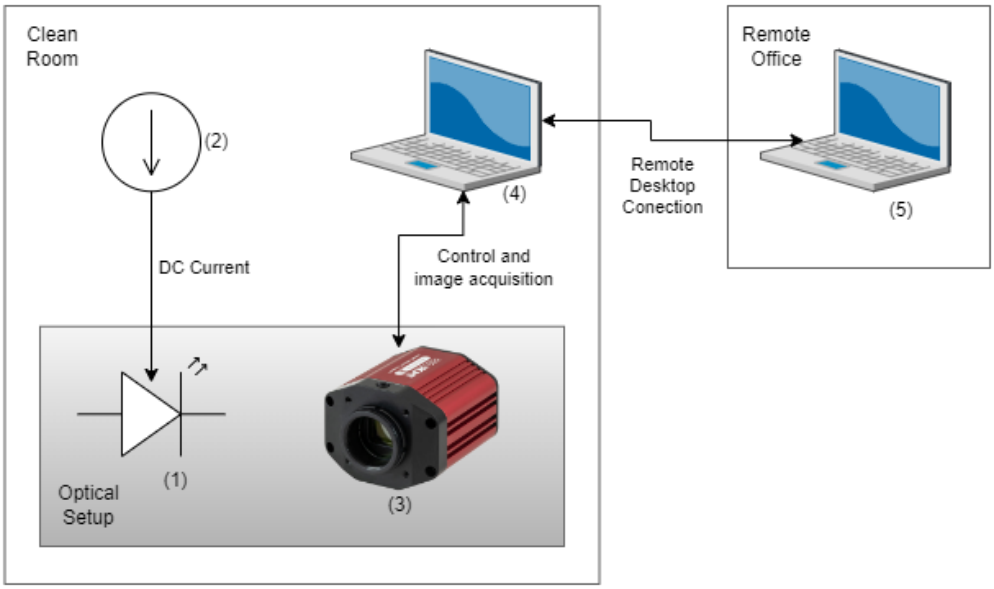

Figure 3.6: Experiment electrical and digital connections.

3.4 Image Acquisition parameters

Each one of the three setups had its own properties, however, the same images were acquired for all of them. Some batches of images were discarded due to detected disturbances during the exposure. The process of acquiring enough images in the same setup with different exposure times required 1 hour typically. This time could be up to 4 hours when using the maximum exposure times allowed by the detector but no benefits were noted from using them, so just a few exposure times were selected. All the remaining detector parameters were the same during the entire experiment; those are detailed in the Table 3.3.

Table 3.3: Image Acquisition parameters. All these parameters were the same for the entire experiment.

Detector Parameter	Value
Image Poll Timeout	100 ms
Gain	0
Black Level	5
Horizontal Binning Level (X)	1 px
Vertical Binning Level (Y)	1 px
ROI	(0,0) to (1919,1199)
Frames	100
LED State	0 (OFF)
Camera Mode	1 (Image shoot)

3.5 Results

3.5.1 Setup 1

The setup 1 was the first attempt to acquire well focused images and figuring out a suitable LED brightness. Figure 3.7 illustrates a slice of the averaged image from the 100 frames stack and Table 3.4 presents basic information of the image.

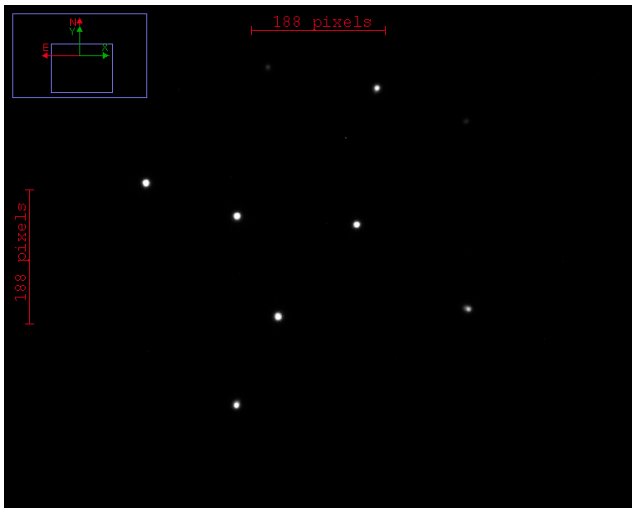

Figure 3.7: Averaged image slice from Setup 1. Exposure time of 500 ms.

Table 3.4: Averaged image slice from Setup 1 data.

Exposure time	500 ms
Max	1737.8400
Min	1.0100
Mean	1.3923
Frames	100

3.5.2 Setup 2

The setup 2 used a white light instead of the red one of the previous setup to acquire images. Figure 3.7 illustrates a slice of the averaged image from the 100 frames stack and Table 3.4 presents basic information of the image.

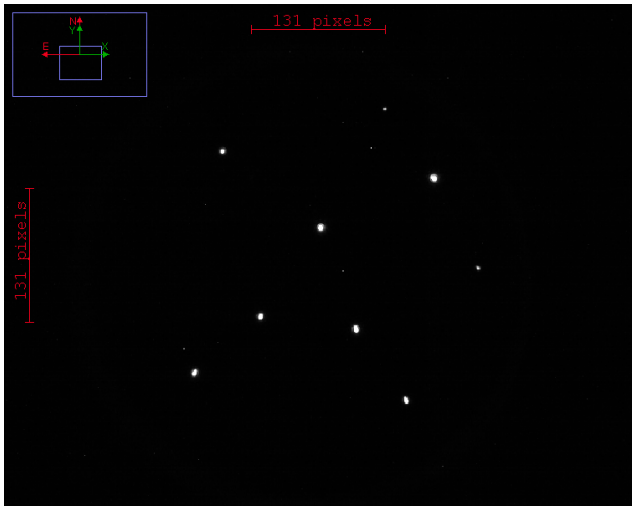

Figure 3.8: Averaged image slice from Setup 2. Exposure time: 100 ms.

Table 3.5: Averaged image slice from Setup 2 data.

Exposure time	100 ms
Max	430.2500
Min	1.0000
Mean	1.1320
Frames	100

3.5.3 Setup 3

The setup 3 used the same red light from the Setup 1 to acquire images. Three different cases were needed to search for a better image quality, which will be discussed further at the end of the chapter. Here is presented a sample of the images obtained for each one.

Setup 3: Case 1

Figure 3.9 illustrates a slice of the averaged image from the 100 frames stack and Table 3.6 presents basic information of the image.

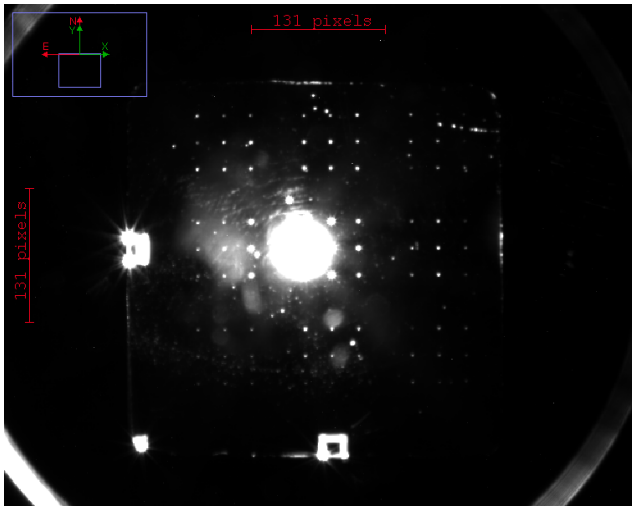

Figure 3.9: Averaged image slice from Setup 3, Case 1. Exposure time: 1 s.

Table 3.6: Averaged image slice from Setup 3, Case 1 data.

Exposure time	1 s
Max	4094.0000
Min	2.8700
Mean	58.8386
Frames	100

Setup 3: Case 2

Figure 3.10 illustrates a slice of the averaged image from the 100 frames stack and Table 3.7 presents basic information of the image.

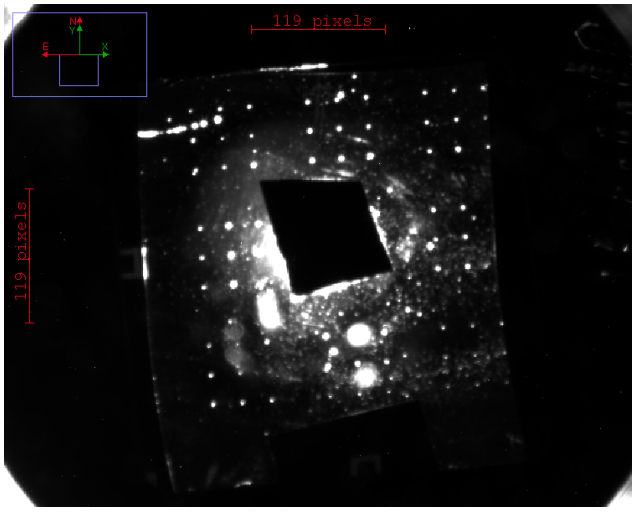

Figure 3.10: Averaged image slice from Setup 3, Case 2. Exposure time: 1 s.

Table 3.7: Averaged image slice from Setup 3, Case 2 data.

Exposure time	1 s
Max	4094.0000
Min	2.3000
Mean	48.7919
Frames	100

Setup 3: Case 3

Figure 3.11 illustrates a slice of the averaged image from the 100 frames stack and Table 3.8 presents basic information of the image.

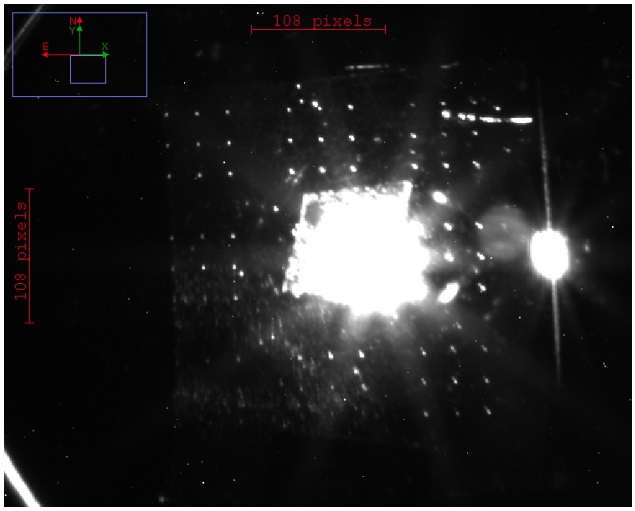

Figure 3.11: Averaged image slice from Setup 3, Case 3. Exposure time of 15 s.

Table 3.8: Averaged image slice from Setup 3, Case 3 data.

Exposure time	15 s
Max	4094.0000
Min	2.6500
Mean	27.5111
Frames	100

3.5.4 Spatial noise

An additional image is illustrated in Figure 3.12. The rendering was adjusted to highlight the spatial noise dominated by random values added to each row of pixels. The typical value observed in each dataset was consistent to the background RMS value around each star.

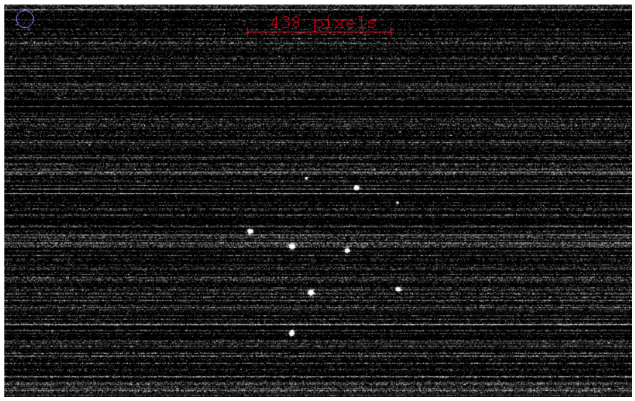

Figure 3.12: Image of Frame 1 / Exposure time: 500 ms. The saturation was adjusted to highlight the spatial noise.

3.6 Discussion

A brief qualitative analysis of the results from each setup is discussed here. The fourth point refers to the issue about the spatial noise.

- The images obtained with the first setup present well-defined light sources. For exposure times below 1 second, the maximum pixel value did not reach the maximum value allowed: 4094. These images are suitable to be used in for the astrometry precision limitations analysis in the Chapter 4.
- Images from the second setup reaches a quality similar to the first setup. However, when these images were processed by the star location algorithms, more extended PSF were detected, indicating a missed detail: the images were not well-focused.
- Images from the third setup, for all photo-masks, presented too much background brightness and irregular patterns from the LED behind the mask. After different approaches trying to find a suitable solution, it was not possible to fix this issue. At the moment of the experiment images acquisition, it was not possible to check if the quality was enough for further analysis.
- The spatial noise evident in images like the one in Figure 3.12, was present in all the images. The RMS value was low but it was expected to see its effects in the star location results: a higher location error or dispersion in the data obtained for the vertical coordinate Y.

Chapter 4

Astrometric precision limitation

As the author mentions in Van Altena (2013)[1], Astrometry is *"one of the oldest branches of astronomy"*, which purpose is to study the positions and motions of celestial bodies like asteroids, planets, stars, and galaxies, using measurement techniques.

4.1 Definitions and Terminology

- The Point Spread Function (PSF) is a metric that quantifies the response of an optical system to a point light source. The shape projected on the detector is defined by the characteristics of the system, including the aperture shape, image distance, and light wavelength.
- In the context of an optical system comprising an aperture and a detector, the Resolution limit of the system is defined by the Full Width at Half Maximum (FWHM), as defined by the following Equation 4.1:

$$\mathrm{FWHM}_\theta = 1.025\frac{\lambda}{D}, \tag{4.1}$$

  where λ is defined as the light (center) wavelength and D represents the system aperture diameter.
- The methodology employed in this study involves the use of point-like light sources. In optics, these sources produce a typical image pattern known as the Airy disk when they are well focused on the detector through a circular aperture. The theoretical definition of the Airy disk is based on its intensity I, as in Equation 4.2.

$$I(x) = I_0\left[\frac{2J_1(x)}{x}\right]^2, \tag{4.2}$$

  where I_0 is the maximum intensity at its center, x is the radial distance to its center and $J_1(x)$ is the Bessel function of the first kind. An example of an ideal PSF with an Airy disk profile is illustrated in Figure 4.1.

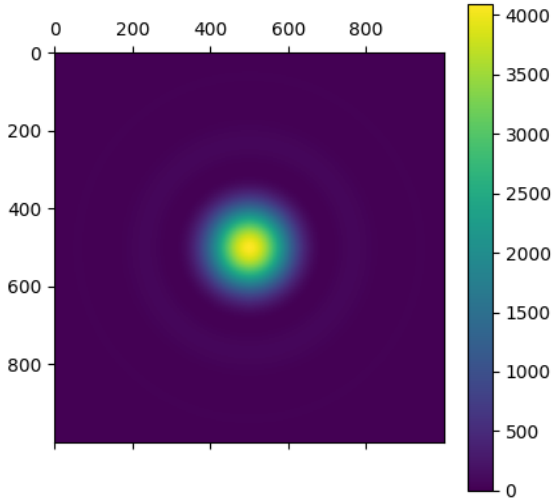

Figure 4.1: Parameters: area of 1000 pixels times 1000 pixels, $I_0(x_c, y_c) = 4094$, center coordinates $(x_c, y_c) = (500, 500)$, and radius $R_z = 200$px.

In the Airy pattern, the first zero is defined as a dark ring at a distance R_z from its center, as described by the following Equation 4.3:

$$R_z = 1.22\frac{\lambda}{D}. \tag{4.3}$$

- For a detector that receives light from multiple sources, it is advantageous to define a Region of Interest (ROI). The image generated by the CMOS detector utilized in this study has a full size of 1200 pixels vertically and 1920 pixels horizontally; it includes background light and can display unknown noise that is distant from the point-like light sources (the subject of study) images that can be disregarded by selecting small windows: the ROIs. The size of the ROIs must be appropriate to contain a reasonable portion of the PSF while excluding other objects.

- Analog-to-Digital Units (ADUs): the sensor of digital detectors, such as CCDs and CMOS, are composed of an array of active pixels and several stages to convert from the incident photons to the signal reported in ADUs or Digital Number (DN). This quantity reports the signal level in each pixel and its maximum is defined by the "ADC resolution" of the detector. As can be seen in the book by Janesick (2007)[30], many quantities are involved but it will be enough to consider just the ADC Gain K_{ADC}.

- One crucial parameter to be aware of when studying astronomical images is the Signal-to-Noise ratio (SNR). This value is frequently employed in scientific and engineering contexts to assess the quality of the signal under investigation in relation to the all the observation noises. Formally defined as it follows:

$$\text{SNR} = \frac{\text{Signal(S)}}{\text{Noise(N)}}$$

In the context of our study, which assumes point-like light sources and an unitary detector gain, it is possible to define the signal S as the total number of (photo-) electrons generated in the detector by object-impacting photons during an exposure time T and over a total of n_{px} pixels.[31] The quantity n_{px} is defined as the number of pixels contained in the signal aperture, as the following Equation 4.4 states:

$$n_{px} = \pi \left(3\sigma_{px}\right)^2, \tag{4.4}$$

these "pixels" are spread as a circle centered in the maximum counts pixel of each ROI with a radius of $3\sigma_{px}$ pixels. The value of σ_{px} is given by the standard deviation of the Gaussian curve assumed as a profile for the PSF.

To quantify the total noise N, every relevant source of noise is sum in quadrature as in the following equation 4.5:

$$N = \sqrt{S + n_{px}(S_b + S_d + \mathrm{RON}^2)}, \tag{4.5}$$

where S_b is the (squared) sky-background Poisson noise, S_d is the (squared) shot noise by dark current and RON^2 is the (squared) readout noise. The Poisson noise from the source itself is $\sqrt{S}$. The term n_{px} is used because the values of S_b, S_d and R^2 are defined for one pixel, unlike S that is defined by the entire aperture.

It is necessary to note that the quantities S and S_b are both originally dependent on the exposure time T (in seconds) of each observation and the gain G (in ADU / photo-e^-). The signal S and the background S_b originate from the fluxes of the object light F and the sky-background light F_b (in photons / second), respectively. The dark current signal S_d is dependent solely on the exposure time, but with modern electronics, it is negligible even for large values of T. The fourth term RON comes from the detector electronics; it depends on the manufacturer fabrication processes and is reported in terms of e^-[RMS]. All four quantities are expressed in terms of ADUs.

4.2 Methodology

In this study, the location algorithms of each object refer to the estimation method used to obtain the star coordinates from the observations obtained through the optical experiment described in Chapter 3. All computations were conducted using the programming language *Python 3.11* on a personal computer with the Windows 10 operating system.

A general algorithm was employed to obtain the star location data, following the subsequent steps:

1. Initial coordinates
2. Analysis parameters
3. 1D Marginal sums with Gaussian fit
4. Background estimation

5. Threshold step
6. SNR estimation
7. Location methods
8. Recover detector reference and barycentric coordinates

4.2.1 Initial coordinates

The initial coordinates refer to the horizontal (X) and vertical (Y) pixels of each star under study, with respect to the detector array. These coordinates were selected manually for each batch of images using the AstroImageJ software, as illustrated in Figure 4.2. A suitable sample frame was opened and visualized for each image, and for each star, the pixel with the maximum value was selected as the initial guess for the position of each corresponding star and therefore the analysis ROI center for the next step.

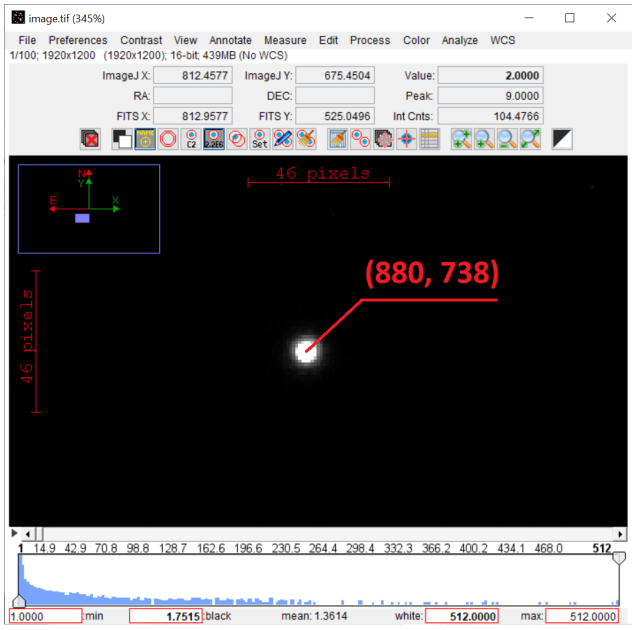

Figure 4.2: Initial coordinates selection.

4.2.2 Analysis parameters

In order to select an appropriate ROI size ΔROI, it is necessary to reach an appropriate balance between the amount of information received, photons from the source, and the noise from pixels that are too far from those that received the greater part of the signal, the aperture pixels. A preliminary estimation was made, taking into account the theoretical PSF for point-like light sources with the actual optical experiment: the Airy pattern and its FWHM. A square ROI is an appropriate choice in this controlled experiment, as we anticipate just circular shapes for the PSF. This implies that no particular direction is preferred. Finally, the criteria to define the ΔROI value was a direct requisite from the next Steps.

The resolution limit FWHM in this system, defined by the light wavelength λ and the optics aperture diameter D, was needed to compute the Cramér-Rao Lower Bound. The light used to illuminate the masks is characterized by its wavelength $\lambda = 625$ nm, for the red light. The aperture diameter, given by the lens aperture, is D = 51.6 mm. Then, the FWHM for the optical system is defined, in terms of pixel size, by Equation 4.6 as:

$$\text{FWHM}_{px} = \text{FWHM}_{\theta}\frac{r}{\Delta px} = \left(1.025\frac{\lambda}{D}\right)\frac{r}{\Delta px}, \tag{4.6}$$

where r is the image distance from lens interface (aperture) to detector (focal plane), and Δpx is the pixel size.

A commonly used model for the PSF is the Gaussian distribution; it is used for some analysis parameters in the next step. Its standard deviation σ can be estimated from the FWHM value by a simple conversion:[7]

$$\text{FWHM} = 2\sqrt{2\ln 2}\sigma \Rightarrow \sigma = \text{FWHM} \cdot 0.629791625024239$$

.

4.2.3 1D Marginal sums with Gaussian fit

This marginal sums technique from astrometry analysis was employed as a preliminary estimation to provide initial parameters for the more powerful location methods. For each ROI, the pixel values were added in both the horizontal and vertical directions, resulting in a one-dimensional sum of rows and columns, respectively. This procedure yields one array for each direction, with the pixel coordinate exhibiting the maximum value selected as the initial estimate for the star position: (x_0, y_0). This estimate is derived independently for each direction. An example of the marginal sums is illustrated in Figure 4.3.

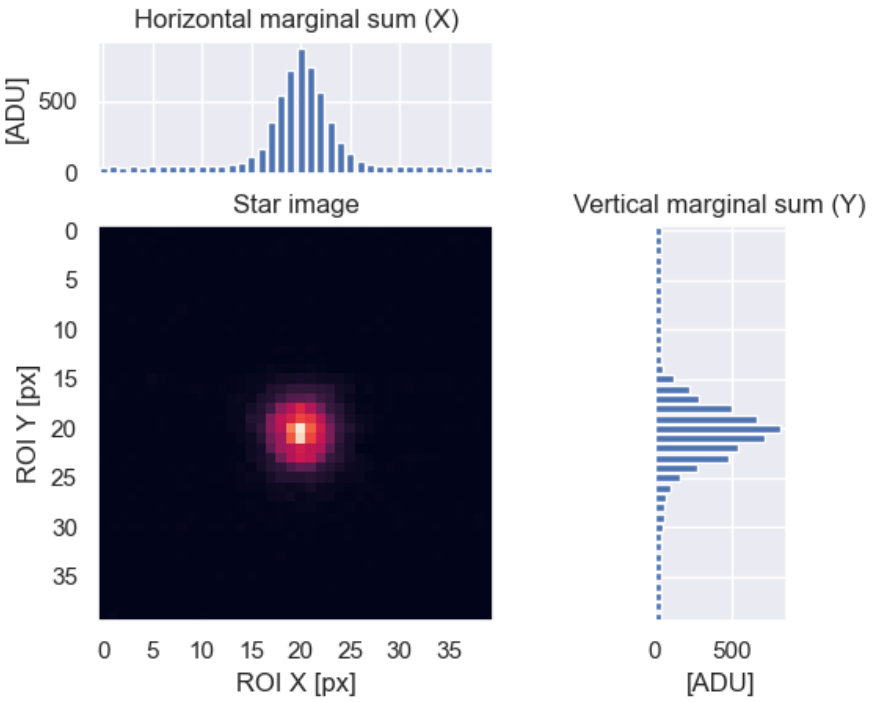

Figure 4.3: Step 3: 1D Marginal sums with Gaussian fit

Once an initial position, (x_0, y_0), was defined for each star, a one-dimensional Gaussian curve fit was applied to each marginal sum by Least Squares (LSQ), as the ones illustrated in Figure 4.3. This process yielded a parameter σ_{1D}, which was used to define suitable apertures for estimating the background and signal from each ROI.

4.2.4 Background estimation

There are a number of different approaches that can be taken to define a background noise for an image. In the field of astronomy, it is customary to utilize the root-mean-square (RMS) value of a ring encompassing a surface with radii of 3σ and 4σ in the image, centered on the initial guess position of the star, (x_0, y_0). This method assumes an Airy disk for the PSF of the light source and employs a Gaussian curve fit to approximate it. The value of σ_{1D} is then determined by the Gaussian curve standard deviation. The justification for this approach is primarily based on the assumption that beyond the $3\sigma_{1D}$ radius, there is no discernible signal from the light source photons ($< 99.5\%$). It is possible to assume the vast majority of the signal is confined inside the $3\sigma_{1D}$ radius aperture.

The marginal sums from the previous step were employed to fit a one-dimensional Gaussian curve in each direction. Finally, the mean of $\sigma_{1D}a$ from each direction was used to define the area Θ_{bg}, which was assumed to represent the background for the corresponding star. The intensity I from each pixel inside this area was used to estimate the background as in Equation 4.7.

$$S_b = \sqrt{\langle I(x,y)^2 \rangle} : (x,y) \in \Theta_{bg}, \tag{4.7}$$

where Θ_{bg} is defined as the ring containing the pixels between radii of $3\sigma_{1D}$ and $4\sigma_{1D}$, centered in the initial coordinates (x_0, y_0) of each star.

An example of the background pixels aperture selection is illustrated in Figure 4.4.

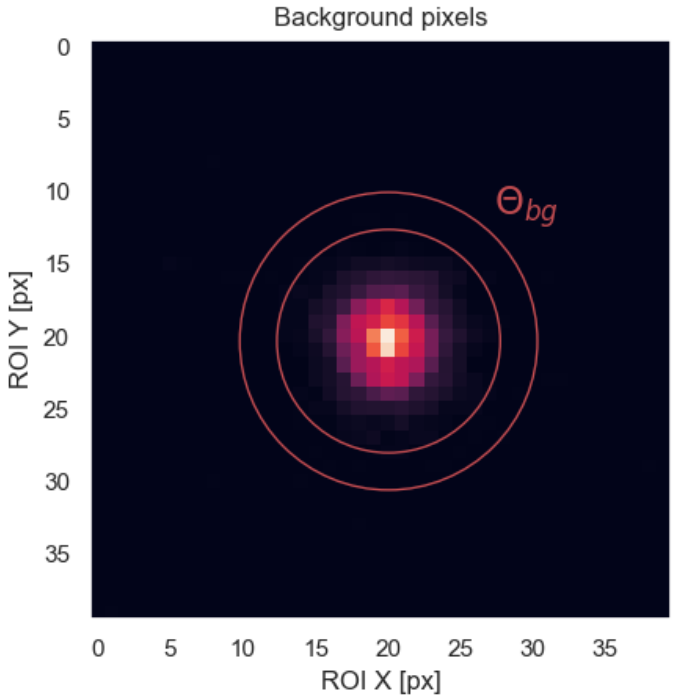

Figure 4.4: Background RMS estimation.

4.2.5 Threshold step

In the literature, there are studies such as that of Stone (1989)[13] that demonstrate the advantage of employing a threshold step prior to the execution of localization algorithms. This approach was utilized in this context. The threshold step comprises a simple filter applied to each ROI, with two parameters: the RMS background value (S_b), and a factor $k < 1$. The latter is contingent upon the specific case in question. The formula is defined by Equation 4.8.

$$I_{th}(x,y) = \begin{cases} I(x,y) - S_b & : \ I(x,y) \geq T \\ 0 & : \ I(x,y) < T \end{cases} \tag{4.8}$$

where $T = k \cdot S_b$ and $0 < k < 1$.

To define an exact value for k, it became necessary to revisit the definitions of background

noise and the Gaussian one-dimensional fit from the previous steps. The objective of apply a threshold to the image is to eliminate the background without removing the signal. Therefore, the proportion of the signal present inside the ring with radii of $3\sigma_{1D}$ and $4\sigma_{1D}$, previously defined as Θ_{bg}, provides a useful indication. According to the normal distribution, just a proportion of $S_{3\sigma_{1D}-4\sigma_{1D}} \leq 0.00527\%$ of the signal is contained beyond the $3\sigma_{1D}$ radius. No signal is present beyond the $4\sigma_{1D}$ radius. This indicates that the discrepancy between the expected signal S and the pixel values $I(x, y)$ can be attributed to almost pure background. In consideration of this behavior and the assumption of a PSF with a Gaussian profile, a commonly accepted approximation, it is possible to define the value of k as follows:

$$k = 1 - S_{3\sigma_{1D}-4\sigma_{1D}} = 0.9947.$$

4.2.6 SNR estimation

A common way to define the quality of an image is through the use of its SNR, which was defined in 4.1. In this thesis, the formal definition for each ROI is given by the following Equation 4.9:

$$\text{SNR} = \frac{S}{N} = \frac{S}{\sqrt{S + n_{pix}(S_b + S_d + \text{RON}^2)}} \approx \frac{S}{\sqrt{S + n_{pix}(S_b + \text{RON}^2)}} \tag{4.9}$$

The quantities involved were estimated using the following:

1. S_b was defined using Equation 4.7.
2. S_d is neglected due to the controlled environment and detection conditions. For modern electronic detectors this is the usual.
3. RON^2 is defined from the detector characteristics by $\text{RON} \leq 7.0e^-[RMS]$. See in B.5. To avoid overestimation of the SNR, the maximum value of RON was used.

To have a consistent analysis, the RON, reported in $e^-[RMS]$, must be converted to "ADU". To this, it is necessary to use the K_{ADC} factor, which can be estimated considering the "Full Well Capacity" and the "ADC resolution" of the detector; both quantities are presented in Tables B.4, and B.5, respectively. The Equation 4.10 shows a simple conversion to obtain the K_{ADC}.

$$K_{ADC} = \frac{\text{Full Well Capacity}[e^-]}{2^{\text{ADC resolution}}[ADU]} \tag{4.10}$$

Then, the RON reported in ADU is given by $RON_{ADU} = RON/K_{ADC}$; assuming a linear behavior in the entire dynamic range.

The signal S is defined as the sum of intensity pixel values over a circular aperture, denoted by Θ_{sig}, centered at the initial star location, (x_0, y_0), with a radius of $r = 3 \cdot \sigma_{1D}$; Equation

4.11 was used to compute this value. The threshold image, as defined in the previous step, is utilized in this process. An example of this signal aperture Θ_{sig} is illustrated in Figure 4.5.

$$S = \sum_{(x,y)\in\Theta_{sig}} I_{th}(x,y) \tag{4.11}$$

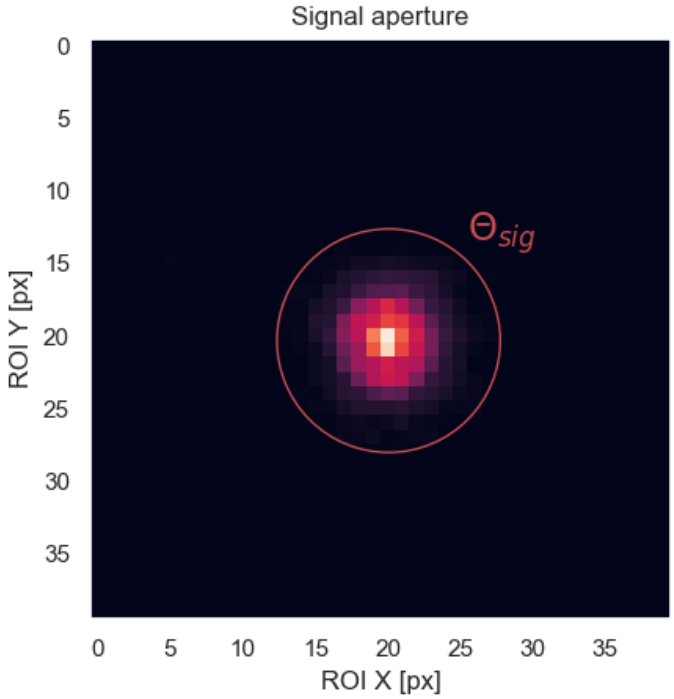

Figure 4.5: Signal aperture Θ_{sig}.

At this point, the images are prepared for processing by the location algorithms to obtain the wanted data.

4.2.7 Location methods

1. Center of Mass

   The "Center of Mass" or "Center of Gravity" is often conceived as a mechanical concept. However, in this analogous case, the definition adopted uses the counts of each pixel (intensity) as the mass, which yields to the mathematical definition given by Equation 4.12.

$$(x_{com}, y_{com}) = \frac{\sum_{(x,y)\in\text{ROI}} I_{th}(x,y)\cdot(x,y)}{\sum_{(x,y)\in\text{ROI}} I_{th}(x,y)}, \tag{4.12}$$

   where $I_{th}(x,y)$ is the intensity value at the pixel coordinates (x,y), defined in the corresponding ROI.

2. Gaussian model fit by LSQ

   The 2D Gaussian model was initiated with the Astropy library.[32] Here, the two-dimensional Gaussian curve is fit on each ROI using the *LevMarLSQFitter* Astropy fitter based on *Levenberg-Marquardt algorithm and least squares statistics* also from the Astropy library.

   To initialize the 2D Gaussian model, an initial guess for its parameters is needed. Those are summarized in the following Table 4.1:

Table 4.1: Initial values for Gaussian model fit by LSQ.

Parameter	Value	Initial guess
Amplitude	I_0	$\max_{(x,y)\in ROI} I_{th}(x,y)$
Mean position	(x_0, y_0)	$\arg\max_{(x,y)\in ROI} I_{th}(x,y)$
Standard deviation	σ_{1D}	From Step 4.2.3

3. Moffat model fit by LSQ

   In astronomy, the Moffat curve is often employed as model to fit a PSF from a point-like light source due to its distinct behavior from the Gaussian model. The Moffat curve offers an advantage over the Gaussian curve in that it employs two parameters, a core width, γ, and a power index, α, to shape the curve, rather than relying solely on the standard deviation, σ. As in the Gaussian fit, the model and the fitter were employed from the Astropy library.[32] The initial parameter values are presented in Table 4.2.

Table 4.2: Initial values for Moffat model fit by LSQ.

Parameter	Value	Initial guess
Amplitude	I_0	$\max_{(x,y)\in ROI} I_{th}(x,y)$
Mean position	(x_0, y_0)	$\arg\max_{(x,y)\in ROI} I_{th}(x,y)$
Core width	γ	1.0 (default)
Power index	α	1.0 (default)

4. Airy Disk model fit by LSQ

   In the theoretical ideal case of a point light source seen through a circular aperture, the resulting pattern on the detector is that of an Airy disk. For purposes of comparison, this model was also fit to the data. The Astropy library[32] was employed in a manner analogous to the previous two models. The initial parameter values are presented in Table 4.3.

Table 4.3: Initial values for Airy disk model fit by LSQ.

Parameter	Value	Initial guess
Amplitude	I_0	$\max_{(x,y)\in ROI} I_{th}(x,y)$
Mean position	(x_0, y_0)	$\arg\max_{(x,y)\in ROI} I_{th}(x,y)$
Radius	R	$1.22\frac{\lambda}{D}$ (from Equation 4.3)

4.2.8 Recover detector reference and barycentric coordinates

Once the star location coordinates have been calculated using the methods described above, it is essential to restore the original reference coordinates, which are those of the detector pixels array itself. The following Table 4.4 presents a summary of the five most important parameters.

Table 4.4: Parameters to recover detector-referenced coordinates from star k in frame j.

Parameter	Definition
Detector origin	$(0, 0)$
Initial star coordinates	$(x_0, y_0)_k$
ROI size	ΔROI
Computed star coordinates	$(x_c, y_c)_{k,j}$
Detector star coordinates	$(x_c^d, y_c^d)_{k,j}$

The recovery of coordinates referenced to the detector pixels array constitutes a common vector algebra problem. The star k detector-coordinates vector $(x_c^d, y_c^d)_{k,j}$ is a function of the vectors defined by the other four parameters. The following Equation 4.13, provides a formal method for obtaining the star k coordinates vector $(x_c^d, y_c^d)_{k,j}$ in frame j:

$$(x_c^d, y_c^d)_{k,j} = (x_c, y_c)_{k,j} + (x_0, y_0)_k - (\Delta\text{ROI}/2, \Delta\text{ROI}/2) \tag{4.13}$$

Once the star k coordinates $(x_c^d, y_c^d)_{k,j}$ were computed with the detector origin reference $(0, 0)$, a final step is necessary to eliminate the common mode perturbations that may affect the entire pixels array. The barycentric coordinates, denoted by $(x_c^{bc}, y_c^{bc})_{k,j}$, are defined as coordinates that do not utilize the detector origin as a reference point, but rather the barycenter $(x^{bc}, y^{bc})_j$ of the entire n stars set. The barycenter for the kth star in frame j is given by the following Equation 4.14:

$$(x^{bc}, y^{bc})_{k,j} = \frac{\sum_{\substack{i=1 \\ i \neq k}}^{n} (x_{i,c}^d, y_{i,c}^d)_j}{n} \tag{4.14}$$

The barycentric coordinates $(x_c^{bc}, y_c^{bc})_{k,j}$ for star k in frame j are given by Equation 4.15.

$$(x_c^{bc}, y_c^{bc})_{k,j} = (x_c^d, y_c^d)_{k,j} - (x^{bc}, y^{bc})_{k,j} \tag{4.15}$$

4.2.9 Cramér-Rao Lower Bound

The astrometric problem of estimating the location of a star, based on a set of observations in a discrete electronic detector array, such as a CCD or CMOS, is inherently a statistical problem. As the author in Echeverria (2016)[6] describes, the Cramér-Rao bound *"provides*

a lower bound for the variance that can be achieved to estimate (with an unbiased estimator) the position of a point source." This statistical tool, the Cramér-Rao Lower Bound (CRLB), can be computed by utilizing known observational conditions, such as the diffraction limit (FWHM).

The formal definition of the CRLB for the one-dimensional case, is presented in the articles by Méndez (2013; 2014)[4][5]. A generalization is then presented in Bouquillon (2017)[7], valid for two-dimensional detector pixel arrays. The latter provides a set of equations for computing the CRLB for a two-dimensional detector based on various quantities and parameters extracted from observational conditions and the observations themselves.

This thesis revisits the work of Bouquillon (2017)[7] in order to provide a comprehensive overview of the two-dimensional CRLB definition. First, the parameters required for the calculation are summarized in Table 4.5.

Table 4.5: Parameters to estimate CRLB.

Parameter	Definition	Comment
Gaussian standard deviation	σ in px	Directly related to the optical system diffraction limit (FWHM).
Pixel size	Δx in px	Previously defined as Δpx in μm.
Number of pixels	n_x and n_y	HxV
Dark current	D in ADU	$D \approxeq 0$
Readout Noise	RON in ADU	Given by the detector properties.

Subsequently, three quantities must be estimated from observations: $\tilde{F}$, b, and $\tilde{B}$. These were actually previously computed in Steps 4.2.4 and 4.2.6. The notation employed in this thesis differs slightly from that used in the cited work, then the equivalent terms are summarized in Table 4.6.

Table 4.6: Variables to estimate CRLB.

Quantity	Bouquillon definition	Used definition
Accumulated Signal	$\tilde{F}$ in ADU	S, from Equation 4.11 .
Accumulated Sky-brightness	b in ADU	S_b, from Equation 4.7.
Accumulated Background	$\tilde{B}$ in ADU	$\tilde{B} = b\Delta x^2 + D + \mathrm{RON}^2_{ADU}$.

It is important to note that the accumulated signal, S, was estimated from images that had undergone a thresholding operation, while the accumulated sky brightness, S_b, was estimated from images that had not undergone a thresholding operation. Both estimations were conducted using the mean image, which was obtained by averaging the values of each set of one hundred frames.

The CRLB in Equation 4.16 is defined for a single dimension using two-dimensional data. Added to the fact that the pixels are squares and there is no difference between the horizontal and vertical directions for this system, the CRLB is identical in each direction, i.e. $\sigma_{CR_y} = \sigma_{CR_x}$.

$$\boxed{\sigma^2_{CR_y} = \sigma^2_{CR_x} = \frac{4\pi^2\sigma^4}{\tilde{F}^2} \frac{1}{\sum_{j=1}^{n_y} \sum_{i=1}^{n_x} \frac{(F^j N_i)^2}{D_i^j}}} \tag{4.16}$$

The terms F^j, N_i, D_i^j, and I_i are defined in Bouquillon (2017)[7] and are explicitly defined in the Appendix subsection C.1.1.

Barycentric CRLB

To achieve a consistent comparison of experimental precision (σ) from the star location distributions and the CRLB (σ_{CR}), the barycenter plays a crucial role once more. Through a brief analysis of error propagation, it is possible to include the effect of the barycentric correction to the CRLB, as was employed to the star location coordinates computed in the Step 4.2.8.

In accordance with Equation 4.15, the location coordinate precision σ_k for star k is influenced by common mode perturbation, so the barycentric correction is required. This precision σ_k is redefined in Equation 4.17 as the corresponding version for barycentric coordinates; the frame number is omitted. Consequently, the same applies to the Cramér-Rao Lower Bound, resulting in its barycentric version, $\sigma^{bc}_{CR,k}$, in Equation 4.18.

$$\sigma_k^{bc} = \sqrt{\sigma_k^2 + \frac{\sum_{\substack{i=1 \\ i\neq k}}^{n} \sigma_i^2}{n}} \tag{4.17}$$

$$\sigma_{CR,k}^{bc} = \sqrt{\sigma_{CR,k}^2 + \frac{\sum_{\substack{i=1 \\ i\neq k}}^{n} \sigma_{CR,i}^2}{n}} \tag{4.18}$$

4.3 Results

4.3.1 Analysis parameters

The initial results presented in this chapter pertain to the anticipated optical conditions that would be expected from the experiment. The combination of a light source (LED), mask, lenses, and electronic detector constitutes an optical system with specific parameters, which depend on the LED wavelength, mask pinhole diameters, lens aperture diameter, and pixel array electronic characteristics. These parameters were then used to initiate the analysis with a known model: the Gaussian PSF for point-like light sources, as well as the Airy disk pattern, their values are presented in Table 4.7.

Table 4.7: Optical experiment images analysis parameters. All values are reported in terms of pixel units. Just the FWHM_θ is reported in radians, which represents the angle from the aperture that projects the image onto the pixels array.

Parameter	Value
Diffraction limit	$\text{FWHM}_\theta = 1.24$ rad $\text{FWHM}_{px} = 1.48$ px
Gaussian PSF standard deviation	$\sigma = 0.63$ px
Airy disk radius (first zero)	$R_z = 1.77$ px
ROI size	$\Delta\text{ROI} = 40$ px
Max SNR	198
Max pixel intensity ratio (registered vs possible)	$1663/4095 = 0.406$
ADC Gain	$\text{K}_{ADC} = 7.32$ ADU/e^-
Readout Noise	$\text{RON}_{ADU} = 0.96$ ADU

4.3.2 Star location distributions

As previously stated in the Results section of Chapter 3, the images captured in configuration 1 were deemed sufficient and the only ones suitable for the analysis of astrometry precision limitation. Consequently, all the results presented here are based upon the optical experiment setting and the acquired images. The following subsections present a series of statistical graphs that illustrate the performance of the centering methods under varying conditions, including image quality, background flux, signal-to-noise ratio, and exposure time.

The Cramér-Rao Lower Bound is presented against the standard deviation or precision from each star location distribution, thereby demonstrating the actual experimental limitation in comparison to the expected theoretical performance. The results were grouped by dataset, with each dataset characterized by its exposure time, which was identical for each of the one hundred frames acquired in each image stack. The detailed data obtained for each dataset individually is presented just for exposure times of 500 ms, 100 ms, and 50 ms; additional exposure times are presented in the appendix section C.2.

Distributions by Method

Four violin plots are presented for each dataset, one for each centering method. These plots provide a concise representation of the distributions of each target computation, specifically the star location. The SNR indicated for each star is the mean value of the one hundred frames. The distributions are separated by detector coordinate, X (horizontal) and Y (vertical). Additionally, the CRLB is shown as a reference for each star location distribution precision. These results are presented in Figures 4.6, 4.7, and 4.8. Additional exposure times are presented in the appendix Figures C.1, C.2, C.3, and C.4.

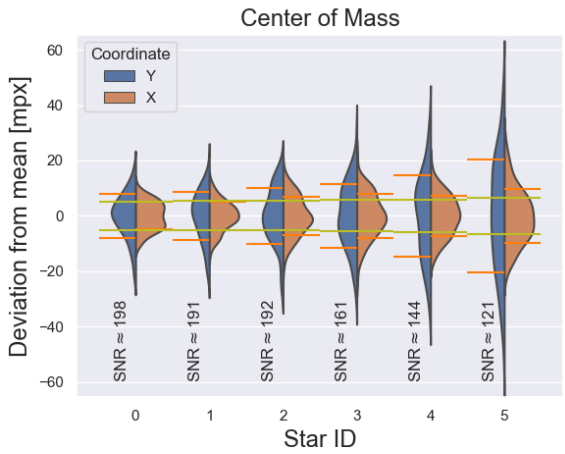

(a) Center of Mass.

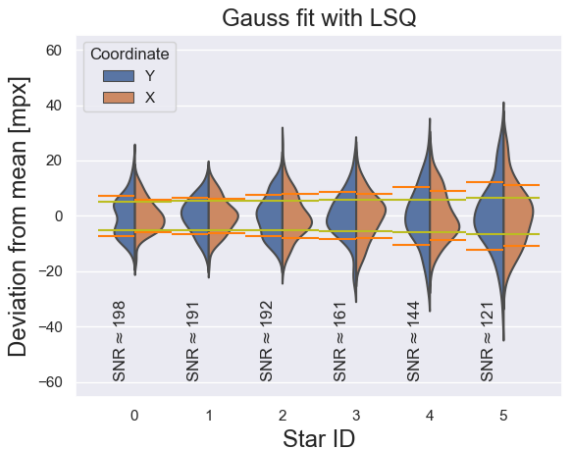

(b) Gauss profile fit by LSQ.

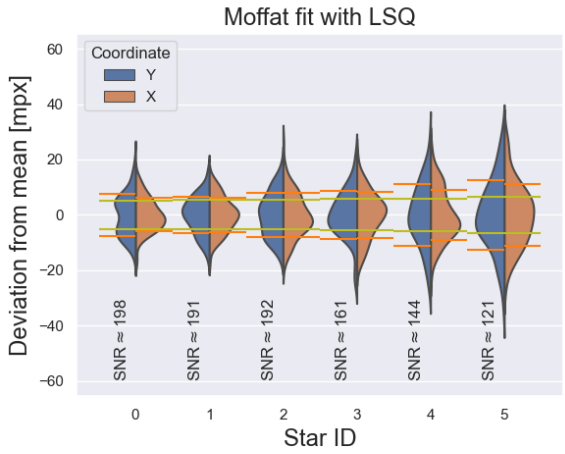

(c) Moffat profile fit by LSQ.

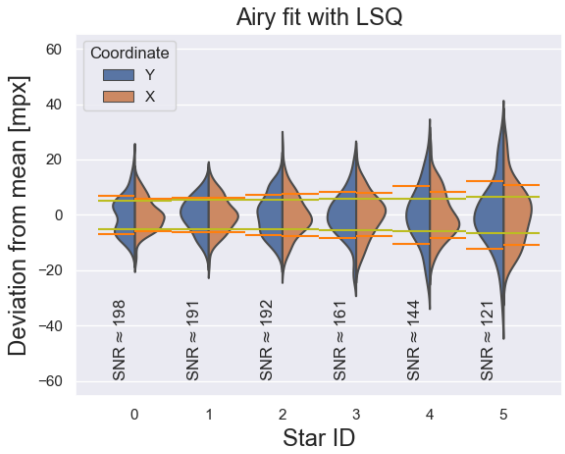

(d) Airy disk profile fit by LSQ.

Figure 4.6: Star location distributions by centering method for an exposure time of 500 ms. The green lines represent the CRLB (σ_{CR}) for the corresponding star, while the orange lines represent the experimental precision (σ) of the star location distribution obtained through a centering method.

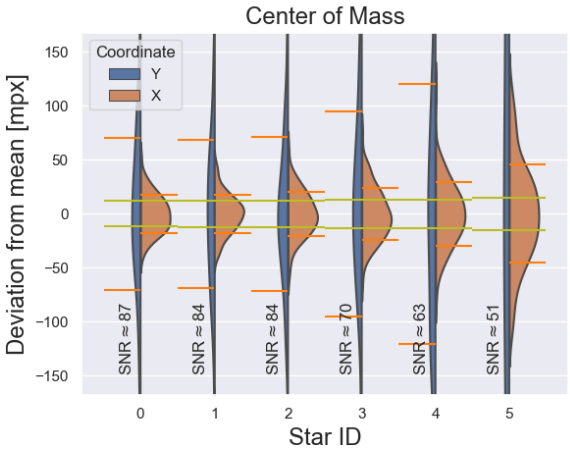

(a) Center of Mass.

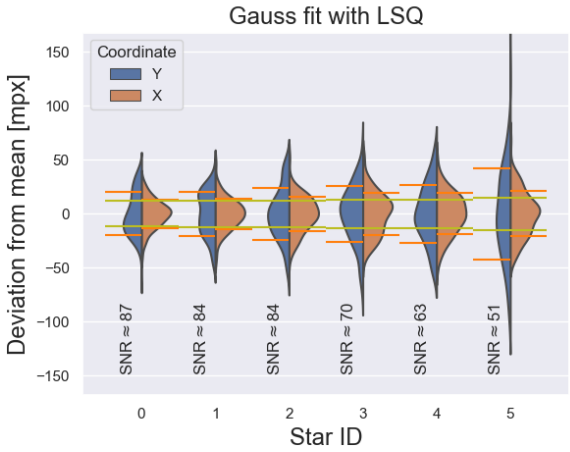

(b) Gauss profile fit by LSQ.

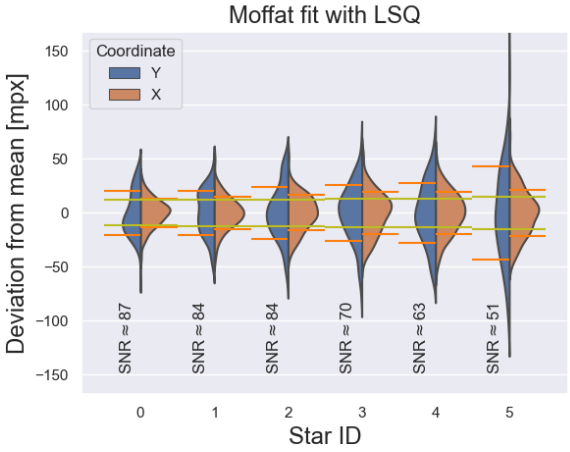

(c) Moffat profile fit by LSQ.

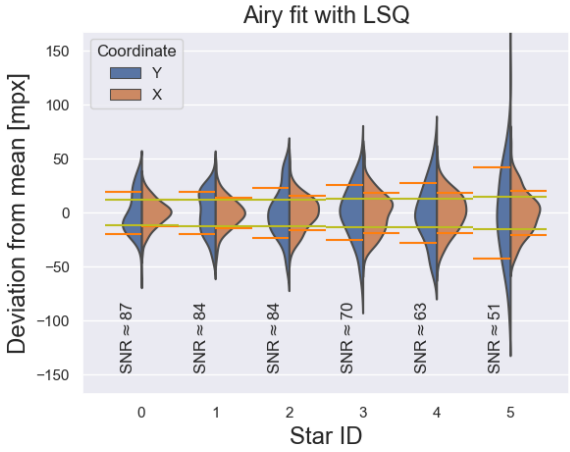

(d) Airy disk profile fit by LSQ.

Figure 4.7: Star location distributions by centering method for an exposure time of 100 ms. The green lines represent the CRLB (σ_{CR}) for the corresponding star, while the orange lines represent the experimental precision (σ) of the star location distribution obtained through a centering method.

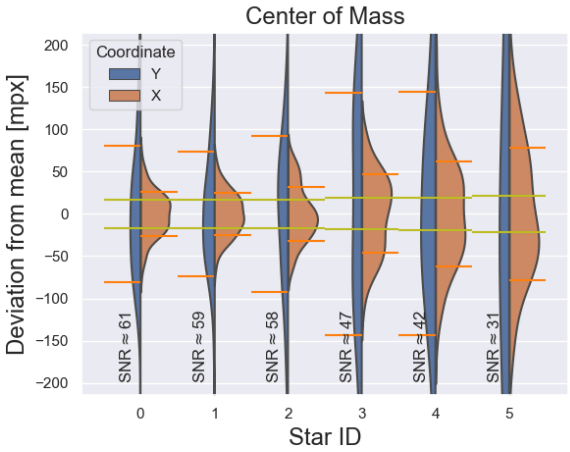

(a) Center of Mass.

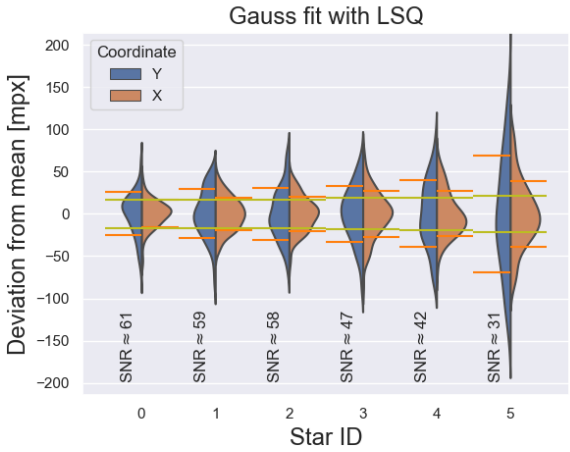

(b) Gauss profile fit by LSQ.

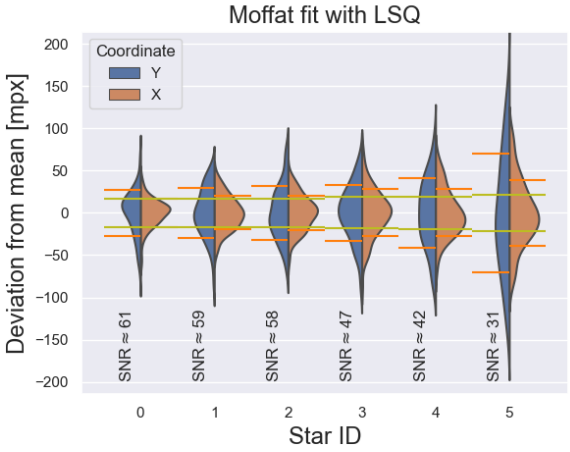

(c) Moffat profile fit by LSQ.

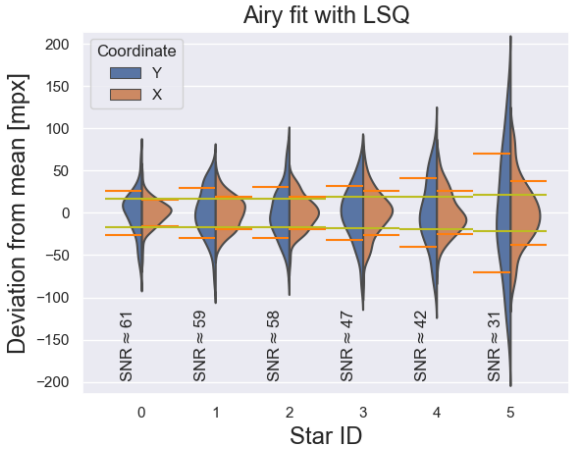

(d) Airy disk profile fit by LSQ.

Figure 4.8: Star location distributions by centering method for an exposure time of 50 ms. The green lines represent the CRLB (σ_{CR}) for the corresponding star, while the orange lines represent the experimental precision (σ) of the star location distribution obtained through a centering method.

Location precision

The results from this subsection present the distributions precision σ and its comparison against the CRLB σ_{CR}. A summary of this comparison for all datasets is illustrated in Figure 4.9.

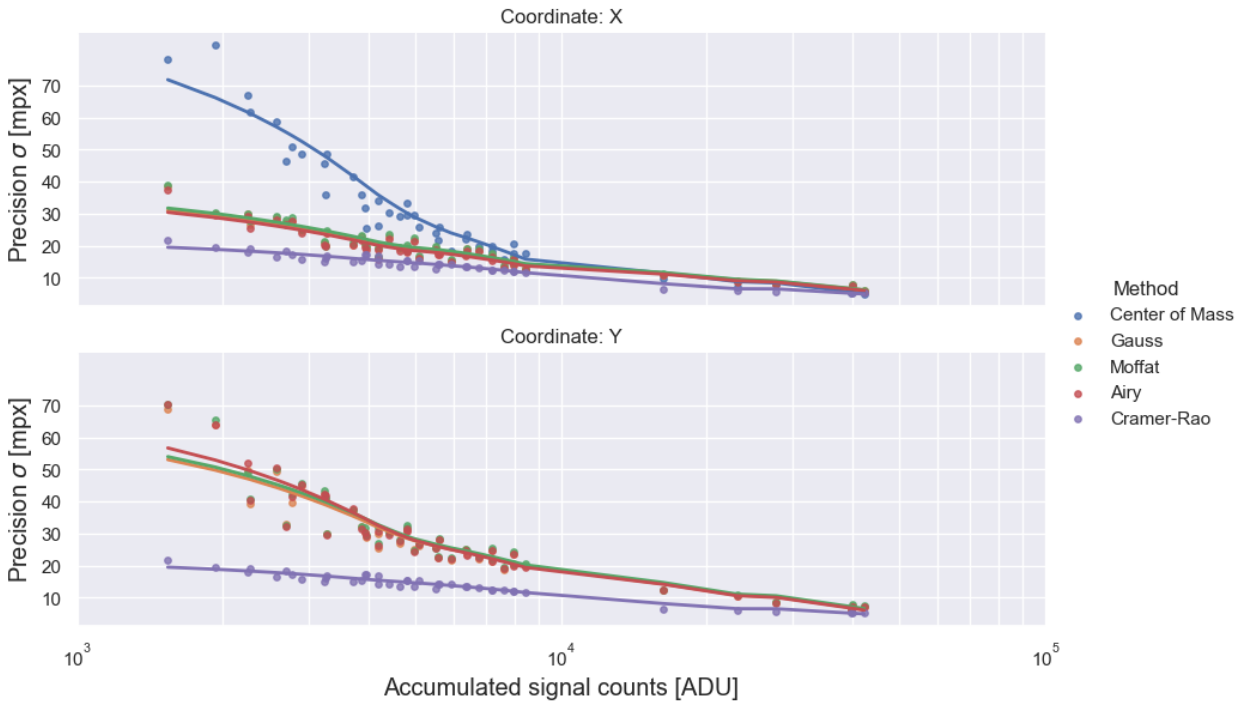

Figure 4.9: The graph compares the center coordinates distribution precision from various location methods with respect to CRLB. These results are presented as a function of the mean accumulated signal counts in ADU, which is expected to dominate the CRLB value. For the Y coordinate, the results from the Center of Mass method were omitted due to its markedly higher value, which is not represented on the chart.

As previously stated in the methodology section, the centering methods employed for this experiment use the same data and algorithms for each coordinate, X and Y. Only the X coordinate data is presented herein, because it presents the best values and an additional noise source in the Y direction was detected, which will be discussed in the corresponding section. Tables 4.8, 4.9, and 4.10 present the ratios of each distribution precision σ to the CRLB σ_{CR}. Additional exposure times are presented in the appendix Tables C.1, C.2, C.3, and C.4.

Table 4.8: Distribution precision by method to CRLB ratios. Exposure time: 500 ms.

Star	SNR	σ_{CR} [mpx]	σ_{CoM}/σ_{CR}	$\sigma_{Gauss}/\sigma_{CR}$	$\sigma_{Moffat}/\sigma_{CR}$	$\sigma_{Airy}/\sigma_{CR}$
0	198	5.25	0.95	1.12	1.15	1.09
1	192	5.30	0.98	1.18	1.18	1.17
2	192	5.30	1.30	1.48	1.50	1.43
3	161	5.70	1.37	1.42	1.44	1.37
4	145	5.97	1.22	1.49	1.52	1.42
5	122	6.57	1.49	1.68	1.70	1.66

Table 4.9: Distribution precision by method to CRLB ratios. Exposure time: 100 ms.

Star	SNR	σ_{CR} [mpx]	σ_{CoM}/σ_{CR}	$\sigma_{Gauss}/\sigma_{CR}$	$\sigma_{Moffat}/\sigma_{CR}$	$\sigma_{Airy}/\sigma_{CR}$
0	88	11.79	1.50	1.10	1.09	1.05
1	85	11.92	1.47	1.20	1.23	1.18
2	85	11.91	1.74	1.36	1.38	1.31
3	70	12.85	1.86	1.51	1.53	1.47
4	63	13.41	2.18	1.43	1.45	1.38
5	52	14.82	3.07	1.41	1.45	1.36

Table 4.10: Distribution precision by method to CRLB ratios. Exposure time: 50 ms.

Star	SNR	σ_{CR} [mpx]	σ_{CoM}/σ_{CR}	$\sigma_{Gauss}/\sigma_{CR}$	$\sigma_{Moffat}/\sigma_{CR}$	$\sigma_{Airy}/\sigma_{CR}$
0	61	16.92	1.54	0.97	0.98	0.93
1	59	17.10	1.48	1.14	1.16	1.11
2	59	17.11	1.87	1.19	1.21	1.14
3	48	18.49	2.52	1.48	1.51	1.44
4	42	19.29	3.21	1.38	1.44	1.32
5	32	21.60	3.62	1.79	1.79	1.74

Location by Frame

When each image frame is regarded as one observation of the experiment, it is beneficial to present the results, from each centering method, frame by frame. Figures 4.10, 4.11, and 4.12 illustrate the star location computed by each method and the CRLB is presented as a reference for comparison of data dispersion. Additional exposure times are presented in the appendix Figures C.5, C.6, C.7, and C.8.

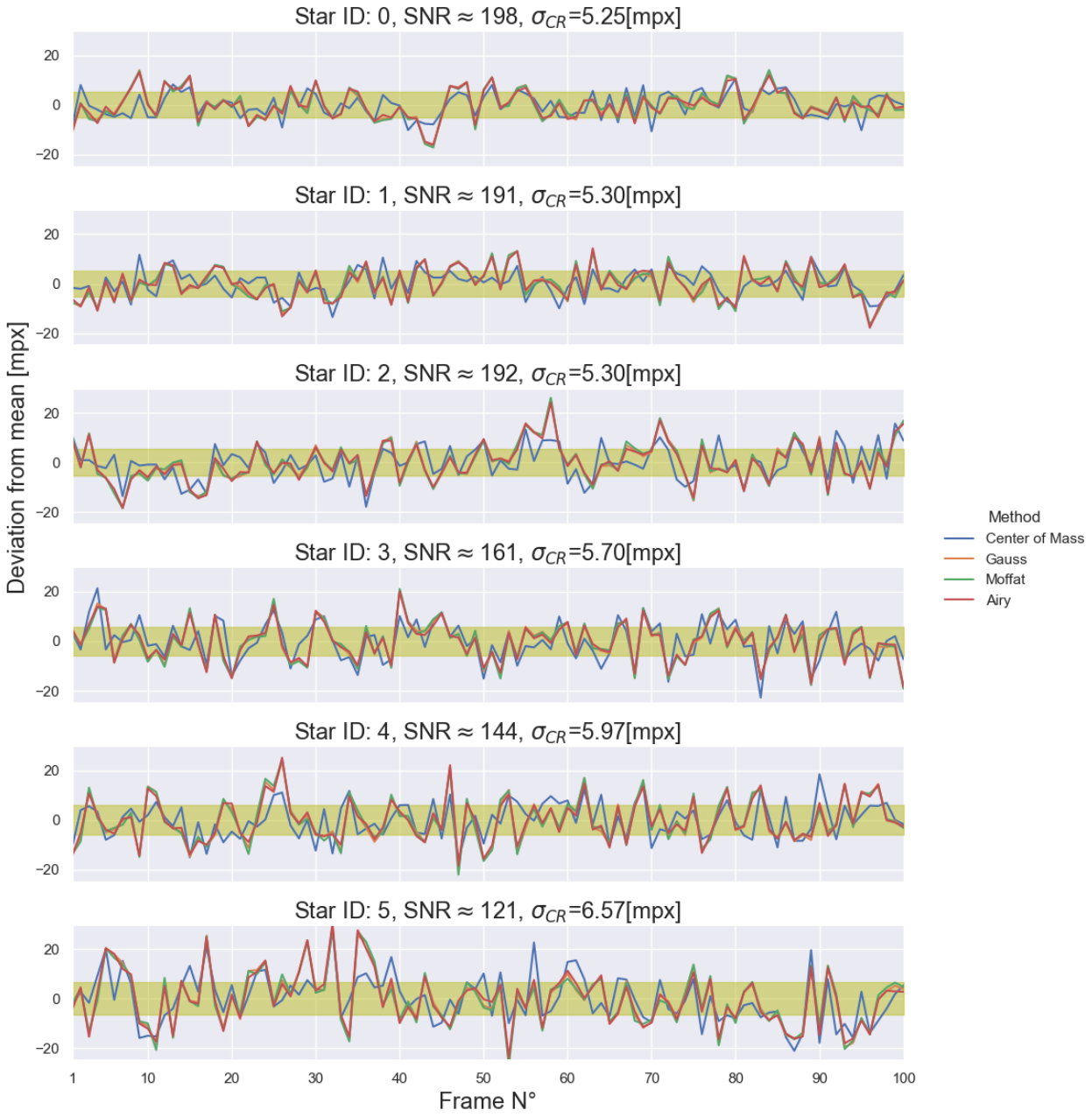

Figure 4.10: Location deviation of stars from its corresponding mean value. The green strips covers the $\pm\sigma_{CR}$ range. It is easily noted that lowering the SNR results in more dispersed location. Exposure time: 500 ms.

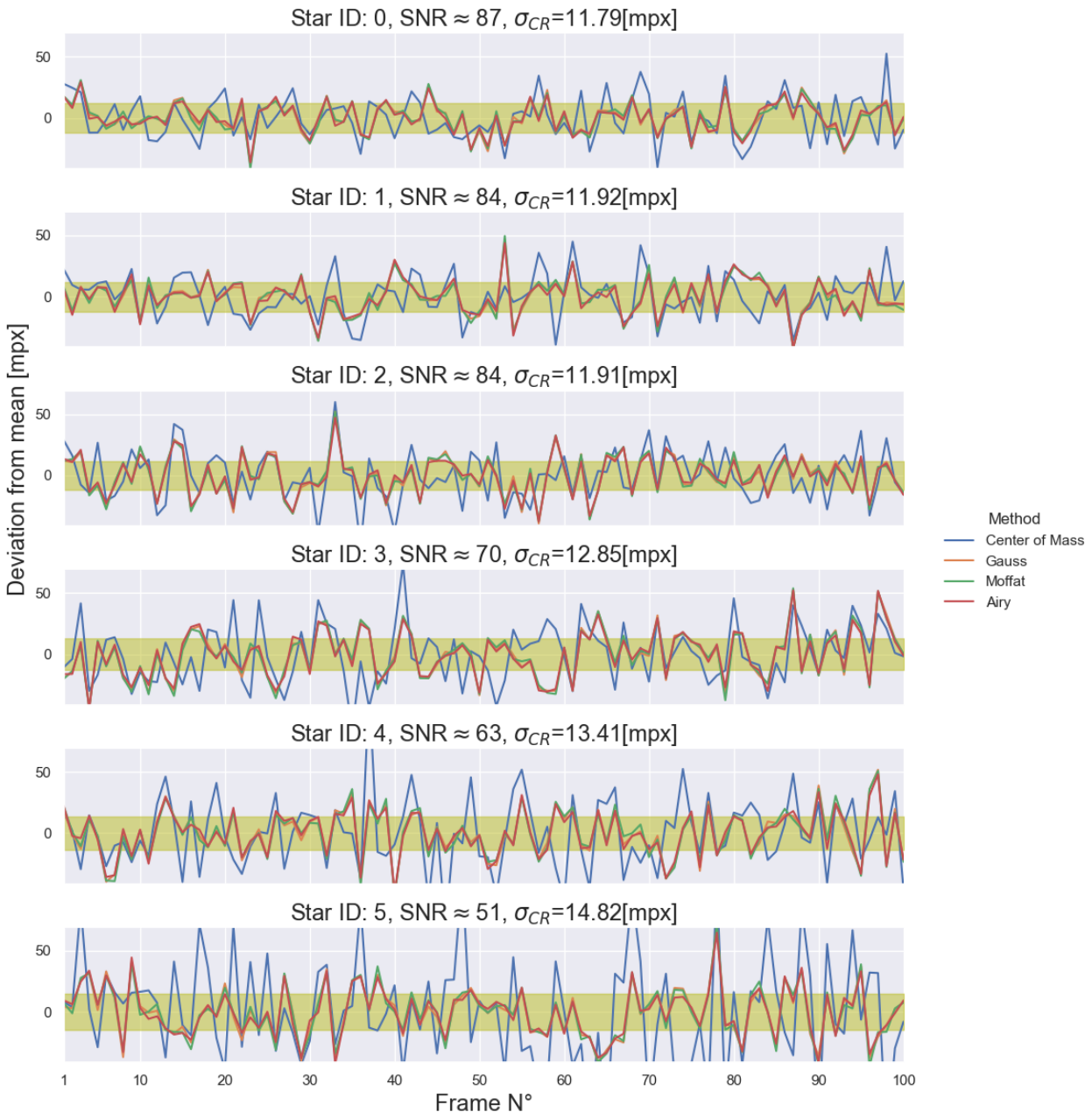

Figure 4.11: Location deviation of stars from its corresponding mean value. The green strips covers the $\pm\sigma_{CR}$ range. It is easily noted that lowering the SNR results in more dispersed location. Exposure time: 100 ms.

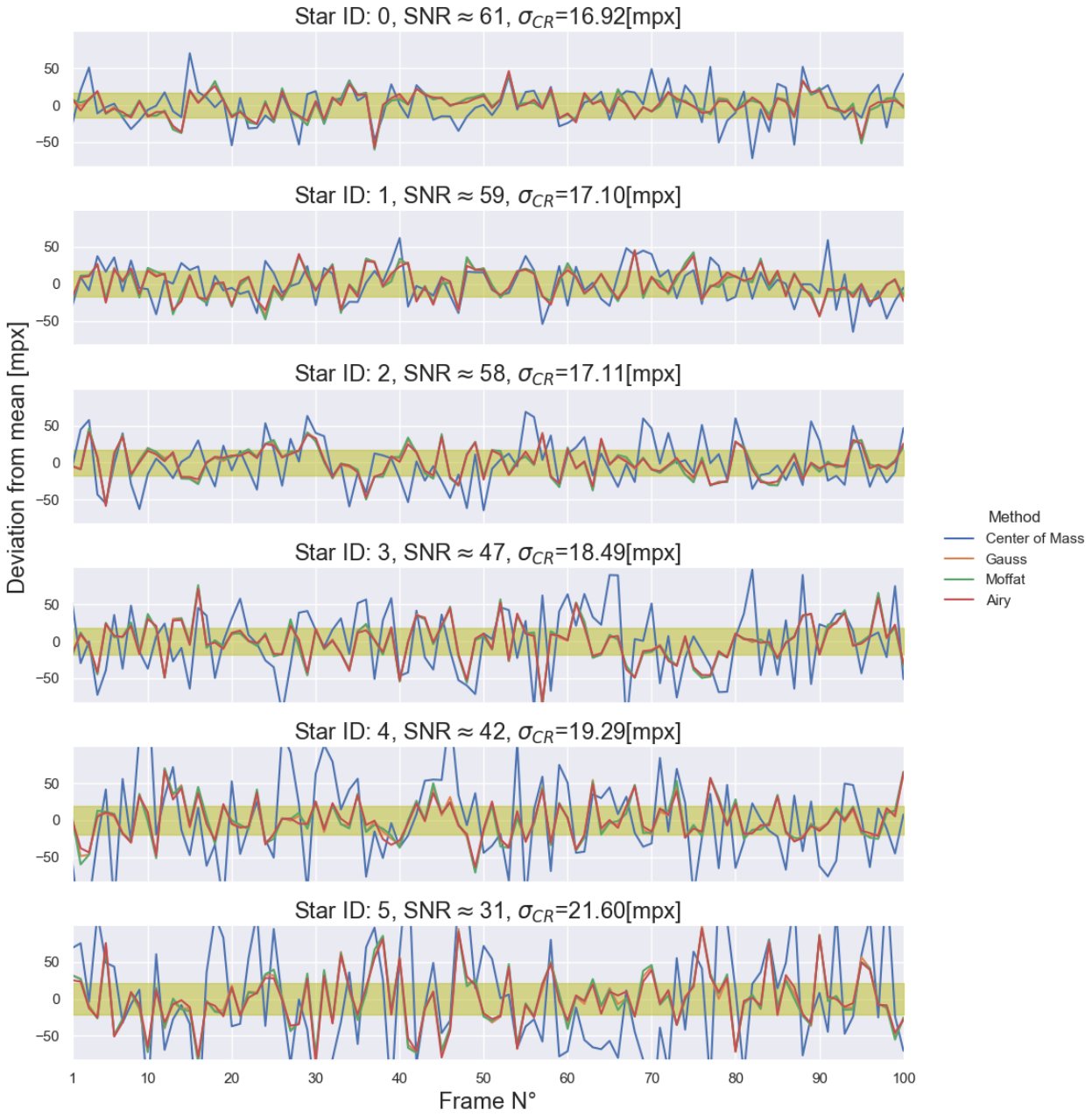

Figure 4.12: Location deviation of stars from its corresponding mean value. The green strips covers the $\pm\sigma_{CR}$ range. It is easily noted that lowering the SNR results in more dispersed location. Exposure time: 50 ms.

CRLB relation to SNR and accumulated Signal

Finally, the insight provided by the CRLB must be considered in conjunction with its relationship to the parameters utilized in the estimation of the requisite quantities for its computations, specifically the accumulated signal counts. Moreover, it is beneficial to examine the relationship between the CRLB and the SNR. This data is presented in Figure 4.13. Each exposure time is associated with a specific SNR, and Accumulated signal counts. This

provides quantitative information about the image quality used to compute the location methods as well as the CRLB. The curve for the 500 ms dataset is presented in Figure C.9.

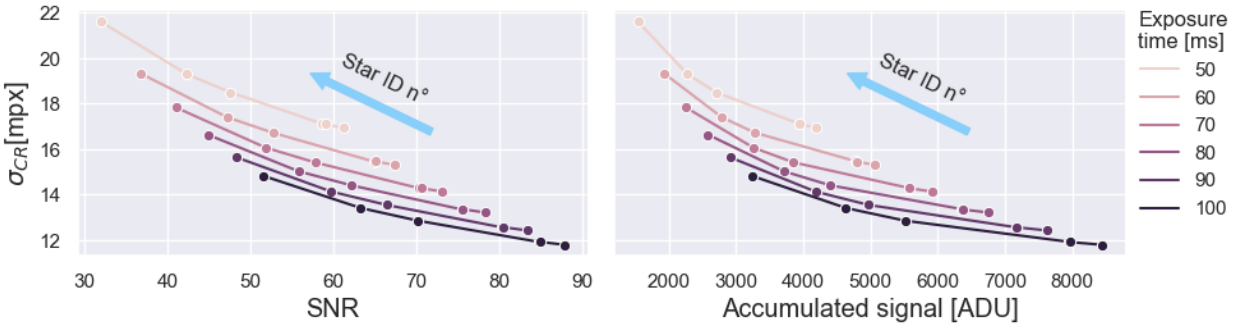

Figure 4.13: Each color represents a different dataset (exposure time in milliseconds). Each point represents the CRLB in function of a representative value of each dataset: mean SNR, and mean Accumulated signal counts, for the corresponding one hundred frames image stack. The second point from right to left in each curve is actually two points, i.e. different stars with the same SNR and Accumulated signal values.

4.4 Discussion

4.4.1 Analysis parameters

The analysis initial parameters presented in Table 4.7 are the direct result of the optical experiment described in Chapter 3. It is possible to infer the effects of changing them by adjusting some experimental parameters:

- Light wavelength λ: the system resolution limit, or FWHM, is directly proportional to λ. An increase in the value of λ will result in a larger resolution limit, leading to a larger PSF. This implies that the photons received from a single light source will be more spread on the detector pixels array, i.e. the same amount of photons are distributed in more pixels. This last affirmation may be interpreted as a change in the ratio between the pixel size and the FWHM, which may result in variations of the CRLB value. The same happens when decreasing the wavelength, resulting in a smaller PSF and focusing the photons coming from one light source in less pixels.
- Aperture size D: this parameter have the opposite effect than λ. Here the relation between D and FWHM is an inverse proportionality.
- ROI size ΔROI: it was proposed that the pixels number must be balanced to ensure sufficient light is captured while avoiding the inclusion of additional light sources from outside the target area. In the methodology, the idea was to initially define an appropriate value by utilizing a multiple of the FWHM or the experimental Gaussian $\sigma_{1D}^{\sim}$. However, the analysis demonstrated that no improvement could be achieved in terms of the ROI size above a certain value. The optimal value, from an information

and computational cost point of view, was found to be a factor of eight times the real Gaussian standard deviation ($8 \cdot \sigma_{1D}$), which was computed in the Step 3 of the Methodology (section 4.2.3). This decision was reached following the testing of various ROI sizes and that in the Steps 4 and 5 (sections 4.2.4 and 4.2.6), the pixels aperture size to compute background (Equation 4.7) and signal (Equation 4.11), respectively, became a requirement as was explained in the Methodology.

- SNR: the value of this parameter is defined in slightly different ways in the literature, depending on the context. The definition employed here is derived from the literature by McLean (2008)[31], which represents a synthesis of the definitions from engineering and astronomy. Two values were fixed to compute the SNR in each case, the Dark current noise ($\sqrt{S_d} = 0$) and the Readout noise ($RON = 7e^{-}[RMS]$). The value of background noise was found to be less than the RON for the longest exposure time (500 ms). Consequently, the value of the SNR may be ultimately defined by the signal noise itself: SNR $\approxeq \frac{S}{\sqrt{S}} = \sqrt{S}$.
- Detector pixel intensity range: the last row in Table 4.7 indicate that just about the 4.06% of the maximum pixel value was registered, this may indicate that no more than the 50% of the pixel intensity range was effectively used.

4.4.2 Distributions by Method

One of the objectives of this study was to gather sufficient data on the artificial stars location to analyze the statistical distribution of these data depending on the method used to compute them. Four distinct methods were employed for this study: The center of mass, Gaussian model fit by LSQ, Moffat model fit by LSQ, and Airy model fit by LSQ. All four of them were applied to the one hundred frames image stack, resulting in the distributions presented in the Results subsection 4.3.2.

It is possible to make some observations regarding these distributions results:

1. In general, it is possible to declare that every method in every dataset proved to achieve nearly normal distributions, but a few exceptions. Also, it is observed that in each dataset, lowering the SNR resulted in increased data dispersion, i.e. worse location precision.
2. The horizontal coordinate X exhibits a markedly lower degree of dispersion (better location precision) than the vertical coordinate Y. This indicates that some form of unexpected noise or distortion may have affected the latter. In fact, this phenomenon was anticipated based on the observation of random rows exhibiting elevated values in the original images, as can be seen in Figure 3.12. The nature of this pattern suggested that it would not affect the horizontal coordinate results, at least not in a relevant degree. Therefore, the course of action was to focus the discussion and conclusions on the best results: the horizontal coordinate X.
3. The sole methodological distinction between the three models fit by LSQ (Gauss, Moffat, and Airy) was the model to be fitted. The fit method entailed the application

of a Least Squares algorithm to each of the datasets. It was expected that the results would exhibit minimal variation, and this was indeed observed in the results.

4. In the existing literature, there is evidence that the center of mass method may be less accurate than the model fitting method by LSQ. The observed difference in the location precision data was consistent with the findings of previous studies. However, discrepancies were identified in the higher SNR images, which suggests that the two methodologies used exhibited similar levels of precision. Figure 4.6 (Exposure time: 500 ms) indicates that for SNR values greater than 100 (strong sources), the dispersion observed may be comparable and even smaller for the Center of Mass distribution, and its accuracy closer to the CRLB. This phenomenon was not observed for distributions derived from images with exposure times less than 100 ms.

5. The mask utilized in the first configuration of the optical experiment consisted of nine distinct pinholes, with some exhibiting markedly smaller diameters than the others. This discrepancy led to disparate PSF shapes and light intensities for each light source. For exposure times below the threshold of 70 ms, four light sources exhibited a SNR below 30, which posed a major difficulty for the numerical algorithms employed in the methodology. To fix this issue, it was decided to remove the four faintest artificial stars; this led to more consistent data.

4.4.3 Distributions precision and CRLB

The manner in which the star location data is distributed depends on the specific parameters and methods employed. In Figure 4.9 the experimental precision of each distribution is plotted against the mean Signal counts of each one-hundred frames image stack. The observations presented in this summary may suggest a potential trend within the observed range. However, it is not possible to make any assertions about the global behavior of faint light sources or those with higher background counts. The following points are the most relevant:

1. A notable outcome is that as the accumulated signal counts increases, the discrepancy between the distribution precision and the CRLB diminishes.

2. As previously stated, the star location vertical coordinate Y exhibits a greater degree of dispersion, thus the necessity to focus on the horizontal coordinate X results is reaffirmed.

3. For accumulated signal counts below 8000 ADU, all distribution exhibit a tendency to improve their precision for higher counts until they reach a point of similarity. For values above 8000 ADU, the same tendency maintains but the Center of Mass method presents an unexpected better precision reaching the estimated CRLB.

4. The discrepancy from the expected behavior, better precision for the models fitting by LSQ, suggests a more detailed study is needed for data from images with the characteristics of those with accumulated signal counts above 8000 ADU (strong light sources and exposure times above 100 ms). As can be seen in Figure 4.9, less data was gathered for this range.

After the summary of distributions precision and CRLB respect to accumulated signal counts, Tables 4.8, 4.9, and 4.10 present the ratios of each method distribution precision with respect to estimated CRLB. These ratios basically present how far the experimental precision is from the theoretical limit indicated by the CRLB. Some specific observations about this data are presented in the next points:

1. It can be restated that as the accumulated signal is lowered, the data dispersion increases. This behavior is consistent across all datasets and exposure times.
2. For an exposure time of 500 ms, the CRLB is between 5.25 mpx and 6.57 mpx in a SNR range of 122 to 198. For SNR values above 100, each σ from the distributions maintains a value below 1.71 times σ_{CR}, for any location method. The standard deviation for the Center of Mass method indicate it is the least dispersed data, while the other three methods exhibit slightly higher dispersion. The Airy disk is the optimal model for LSQ fitting.
3. For an exposure time of 100 ms, the CRLB is between 11.79 mpx and 14.82 mpx in a SNR range of 52 to 88. Unlike the previous dataset, this one presents better precision for the models fitting methods, with a difference of $\sim 36\%$ between the Gaussian model fit and the Center of Mass method. Interestingly, the model fitting methods almost reach the estimated CRLB, indicating their optimal performance in this observational regime. Also, the Airy disk model presents the best performance.
4. For exposure times below 100 ms, the observed performances of all four methods employed are similar to the latter case, even reaching the estimated CRLB for the best star (Star ID: 0, SNR= 61). The degradation of the star location precision by lowering the signal level is restated.
5. For exposure times below 80 ms, it is observed higher CRLB values and higher data dispersion for every location method. Nevertheless, the ratios are higher, which indicates that for worse theoretical precision limit, the experimental precision degrades at an "accelerated" rate.

4.4.4 Location by frame

Although the analysis is focused on the distributions of star location data, observing the experiment observations frame by frame provides insight into the behavior of the data. In Figures 4.10, 4.11, and 4.12 the location deviation from the mean of each star is presented frame by frame. It is also worth noting that the data exhibits the following characteristics:

1. As previously observed, the precision of the data is degraded when the accumulated signal counts is low. This phenomenon is evident in all datasets.
2. In the methodology, the Step 8 described in 4.2.8 involved the computation of star locations by their barycentric coordinates with respect to the barycenter of all the light sources. The objective of this technique was to remove any common mode perturbation present, which may result from random alterations of environmental conditions in the

experiment, such as vibrations or rapid small atmospheric changes. These graphs demonstrate the absence of residual noise resulting from the aforementioned potential perturbations.

4.4.5 CRLB relation to SNR and accumulated Signal

Finally, the behavior of the CRLB must be analyzed with respect to the variables that define its values for each dataset. Figure 4.13 illustrates the relationship between the CRLB and the mean values of SNR, and accumulated signal counts, for each one-hundred frames image stack and light source. It reveals a certain degree of correlation with respect to each of these variables. These can be summarized as follows:

1. Upon observation of the different light sources present in each dataset, it was found that the CRLB value decreased with an increase in the SNR and signal counts i.e. better precision may be reached for stronger light sources for the same exposure time.
2. When comparing the same light source in different datasets, it is observed that for higher exposure times, the accumulated signal counts increase almost linearly as it should be expected from a linear detector.
3. The relationship between SNR and CRLB follows the same trend as for accumulated signal and CRLB.
4. A detailed analysis of Equation 4.16 suggests that the CRLB value may have an inverse proportionality to the accumulated signal counts, which is exactly what is observed in the right graph of Figure 4.13.

In the articles cited, such as those by Méndez (2013; 2014)[4][5], and Bouquillon (2017)[7], the relationship between the signal from the light source and the CRLB, was determined to be evident for bright sources ($\tilde{F}/\tilde{B} \gg 1$): when the source dominates over the background, the CRLB variance is inversely proportional to the signal ($\sigma^2_{CR} \propto \tilde{F}^{-1}$). This behavior was observed in the data from this section, which indicates a consistent analysis from the methodology used, respect to the literature.

Chapter 5

Conclusions

5.1 Photo-mask fabrication

The Chapter 2 was completely a preparatory stage for the focus of this thesis, the astrometry precision analysis. The novel idea of employing optical lithography to fabricate a photo-mask as a fundamental component for the optical experiment represented a potential improvement to be tested.

The results of this chapter demonstrated that, with the available technology, it was possible to create photo-masks with different configurations, including a wide range of pinhole diameters and pinhole separation, as well as various shapes for the pinhole array. These masks may even replicate portions of the sky, based on stellar catalogs, translating the stellar magnitudes into pinhole diameters and the angular distances into linear distances. This may provide an astrometric reference for spatial and ground-based telescopes.

The fabrication results could not be fully tested until the photo-masks were used in the optical experiment. At that point, only parameters such as the diameters and separations of the pinholes were checked in the laboratory. In contrast, the reflectance of the photo-mask could not be tested at this early stage.

5.2 Optical experiment

The objective of Chapter 3 was to gather empirical data. To this end, an experiment was designed and implemented, comprising a variety of hardware and software components, some were off-the-shelf and some were custom-made. The latter included the masks and controller software, both of which required significant time and effort to develop, but were considered to be fundamental processes from both a pedagogical and a practical perspective.

The results were divided into three sections, each corresponding to a specific configuration of the experiment. As previously discussed, the first configuration was the only one that proved to provide suitable images for the astrometry precision analysis, which do not happened

for the second configuration. This may indicate the presence of systematic issues in the second configuration, such as images that are poorly focused or a lack of modifications to adapt the experiment for a different type of light.

With regard to the third configuration, the objective was to test the hypothesis that a photo-lithography manufactured mask would be an effective solution to replicate an artificial far-stellar field. However, this approach presented one crucial problem: the reflectance of the glass-chromium plate was not sufficiently high, resulting in high background light intensity from the LED image projected on the detector pixels array, i.e. a high fraction of transmitted light from the source mixed with the light from the photo-mask pinholes.

The issue mentioned in the previous paragraph was a direct consequence of the Low Reflective Coating (LRC: 8% @ 450 nm) of the original glass material, not from the fabrication process, so it opens the door for potential improvement making a simple change: use a High Reflective Coating (HRC: $>$ 48% @ 450 nm.) This HRC glass plate is available from the same supplier used in this realization. Also, it is possible to fabricate this glass plate in the same laboratory used for the photo-lithography process, but first employing a metal vaporization deposition technique. This improvement is fundamental to achieve lower background and higher SNR. Despite the unfavorable outcome in the immediate term, the images demonstrated that the artificial far-stellar field is feasible with this technology. Consequently, in future applications and developments, a more favorable outcome is possible.

The spatial noise was not removed in this stage, represented in Figure 3.12, and its origin was not effectively identified. Therefore, this phenomenon and the appropriate solution is retained for further investigation in future developments and realizations of the experiment.

5.3 Astrometry precision limitation

In Chapter 4, four experimental analysis parameters were discussed: light wavelength, aperture size, ROI size and SNR.

The influence of light wavelength and aperture size, in the CRLB and the experimental precision achieved, was a direct consequence of their relation to the diffraction limit. From the equations presented in the methodology section, it is clear how they may be changed to test different setups: the use of other wavelengths allow to get results in different bands of the electromagnetic spectrum, and the increase in aperture size will result in a sharper PSF for the same observed objects.

The ROI size parameter demonstrated that its value primarily affects the computational cost of the location algorithms. Smaller ROI size values result in more efficient computations. Conversely, this results in a reduction in the quantity of information fed to the algorithms, which may lead to the generation of poor-quality data. The determination of its value for a specific experiment is an iterative process that may result in an appropriate balance between the quantity of information and the computational cost, although this may require a number of iterations.

The fourth parameter, the SNR, proved to be a pivotal value in determining the quality of the ROI image and the precision of the location results. The images utilized exhibited low background brightness, meaning its value could be neglected for the determination of the SNR value and the CRLB. This does not imply that it can be excluded from the remainder of the analysis. Rather, in this specific observational context, its impact was minimal. However, it may potentially increase in conditions with high background intensities.

Recalling that it was observed that about 50% of the detector pixel intensity range was effectively used, it is possible that the actual configuration of the optical experiment may reach higher SNR values, as higher than 400. For future realizations, the use of the full pixel intensity range will allow the investigation of the experimental precision limit and the CRLB for brighter artificial stars.

The star location distributions revealed significant differences in performance between the algorithms, with LSQ demonstrating superior results for weaker light sources and all algorithms performing similarly for stronger light sources. This highlights the need to consider the specific observational conditions when selecting an optimal method, as no single algorithm can be assumed to be universally superior. An interesting pattern emerges from the data: for weaker sources or less favorable observational conditions, e.g. lower SNR, in all algorithms the experimental precision quickly degrades, "faster" than the theoretical limit.

Each dataset was distinct in terms of its exposure time, yet the number of observations remained consistent at one hundred frames. This allowed for the generation of statistically reliable results. For further analysis, it may be advantageous to increase the number of observations, which could result in enhanced experimental precision. The increase in the number of observations with the same exposure time allows for the testing of a greater range of imaging conditions with different light sources.

The barycentric coordinates proved to be a valuable tool that should be employed in future developments. If this step is not included, it may result in the introduction of common mode perturbations, which could potentially alter the data.

The spatial noise present in the analyzed images was not treated, which resulted in an increased noise in the data. However, it may be possible to reduce the impact of this perturbation by filtering the images or by frame removal, effectively mitigating the observed increase in the data dispersion at the vertical coordinate. Furthermore, it would be beneficial to test whether this affects the horizontal coordinate.

The results of comparing the experimental precision achieved and the theoretical maximum precision achievable (the CRLB) for location algorithms in the context of astrometry demonstrated that the latter can be effectively utilized as an useful "benchmark" tool. To compute this value, it was necessary to know only the diffraction limit of the optical system and the prior information regarding the expected signal, or light intensity. The first is accessible for every instrument to be planned or already in use, and the second may be obtained from stellar catalogs. Consequently, it is possible to evaluate the astrometry precision limit for almost any observational project before the actual observations are conducted.

5.4 General conclusions

Recalling what has been found in the literature, the results of this thesis contribute with a completely experimental approach to the study of the astrometric precision limit. The understanding of the CRLB allowed its estimation from available data of the same observations, which confirmed its usefulness not only from a theoretical point of view, but also from an empirical one.

The methodology tested in this study may be beneficial for observational astronomy and instrumentation planning. It is possible to replicate an analogous portion of the sky with well-known celestial objects in a photo-mask manufactured by the same optical lithography technology from a research laboratory or industry suppliers. The photo-mask dimensions may be as small as a few squared millimeters, containing tens of pinholes (stars) at a distance of a few tens of millimeters from the detector. This results in an equivalent of hundreds of squared milli-arcseconds (mas^2) of sky being replicated in a small space. Subsequently, with an appropriate design, this may be utilized as an astrometric reference on-board for any telescope, thereby enabling the instrument to be calibrated in-situ in real time with controlled observational conditions and information a priori of the objects seen by the instrument.

5.5 Outline

Looking back to the State of the Art section 1.2, there must be noted that some important points were ignored in this thesis, but should be addressed in a future study. For example, in the study by Méndez (2014)[5] it is mentioned that the proximity of the source to the pixel boundaries affects the astrometric precision. The use of the BCR mentioned in the article by Echeverria (2016)[6] may be an interesting alternative to explore. Additionally, the calibration and pixel response characterization of the detector itself may be a critical point, as proposes the author in Lin (2021)[18], specially for high-precision astrometry.

In summary, it is recommended that future realizations include the following improvements and changes: the employment of a high reflectance photo-mask, an extension of the images sample size (number of frames by dataset), the extension of the detector dynamic range usage, the use of already tested software for image processing (e.g. *photutils* photometry library for Python), the test of different experimental setups (e.g. different light wavelengths and bandwidths), the use of different star centering algorithms (e.g. ePSF, and ML), and the use of modern CMOS sensor calibration procedures.

Bibliography

[1] W. F. Van Altena, ed., *Astrometry for astrophysics: methods, models, and applications*. Cambridge: Cambridge University Press, 2013.

[2] K. A. Winick, "Cramer-rao lower bounds on the performance of CCD optical position estimators," in *Annual Meeting Optical Society of America*, p. FI2, Optica Publishing Group, 1986.

[3] H.-M. Adorf, "Limits to the Precision of Joint Flux and Position Measurements on Array Data," in *Astronomical Data Analysis Software and Systems V*, vol. 101 of *Astronomical Society of the Pacific Conference Series*, Jan. 1996.

[4] R. A. Mendez, J. F. Silva, and R. Lobos, "Analysis and Interpretation of the Cramér-Rao Lower-Bound in Astrometry: One-Dimensional Case," *Publications of the Astronomical Society of the Pacific*, vol. 125, pp. 580–594, May 2013.

[5] R. A. Mendez, J. F. Silva, R. Orostica, and R. Lobos, "Analysis of the Cramér-Rao Bound in the Joint Estimation of Astrometry and Photometry," *Publications of the Astronomical Society of the Pacific*, Aug. 2014.

[6] A. Echeverria, J. F. Silva, R. A. Mendez, and M. Orchard, "Analysis of the Bayesian Cramér-Rao lower bound in astrometry: Studying the impact of prior information in the location of an object," *Astronomy & Astrophysics*, vol. 594, p. A111, Oct. 2016.

[7] S. Bouquillon, R. A. Mendez, M. Altmann, T. Carlucci, C. Barache, F. Taris, A. H. Andrei, and R. Smart, "Characterizing the astrometric precision limit for moving targets observed with digital-array detectors," *Astronomy & Astrophysics*, vol. 606, p. A27, Oct. 2017. arXiv:1707.01447 [astro-ph].

[8] M. Gai, D. Carollo, M. Delbò, M. G. Lattanzi, G. Massone, F. Bertinetto, G. Mana, and S. Cesare, "Location accuracy limitations for CCD cameras," *Astronomy & Astrophysics*, vol. 367, pp. 362–370, Feb. 2001.

[9] T. Yano, H. Araki, N. Gouda, Y. Kobayashi, T. Tsujimoto, T. Nakajima, N. Kawano, S. Tazawa, Y. Yamada, H. Hanada, K. Asari, and S. Tsuruta, "CCD Centroiding Experiment for Correcting a Distorted Image on the Focal Plane," *Publications of the Astronomical Society of the Pacific*, vol. 118, pp. 1448–1454, Oct. 2006.

[10] C. San Martin, R. A. Méndez, and M. Gai, "Experimental study of the astrometric Cramér-Rao limit on bidimensional digital detectors," 2021.

[11] M. Gai, A. Vecchiato, A. Riva, D. Busonero, M. Lattanzi, B. Bucciarelli, M. Crosta, and Z. Qi, "Astrometric Precision Tests on TESS Data," *Publications of the Astronomical Society of the Pacific*, vol. 134, p. 035004, Mar. 2022.

[12] R. Gil Otero, R. Mackie, C. Greenaway, T. Lemon, P. Jerram, and J. Pratlong, "Capella: CIS120 general purpose CMOS sensor for space applications," in *International Conference on Space Optics — ICSO 2020* (Z. Sodnik, B. Cugny, and N. Karafolas, eds.), (Online Only, France), p. 28, SPIE, June 2021.

[13] R. C. Stone, "A comparison of digital centering algorithms," *The Astronomical Journal*, vol. 97, p. 1227, Apr. 1989.

[14] C. L. Lu, "Digital Image Centering with the Maximum Likelihood Method," *Astronomy and Astrophysics*, vol. 275, p. 349, Aug. 1993.

[15] C. Zhai, M. Shao, R. Goullioud, and B. Nemati, "Micro-pixel accuracy centroid displacement estimation and detector calibration," *Proceedings of the Royal Society A: Mathematical, Physical and Engineering Sciences*, vol. 467, pp. 3550–3569, Dec. 2011.

[16] R. A. Lobos, J. F. Silva, R. A. Mendez, and M. Orchard, "Performance Analysis of the Least-Squares Estimator in Astrometry," *Publications of the Astronomical Society of the Pacific*, vol. 127, pp. 1166–1182, Nov. 2015.

[17] S. Espinosa, J. F. Silva, R. A. Mendez, R. Lobos, and M. Orchard, "Optimality of the maximum likelihood estimator in astrometry," *Astronomy & Astrophysics*, vol. 616, p. A95, Aug. 2018.

[18] F. R. Lin, Q. Y. Peng, Z. J. Zheng, B. F. Guo, and Y. J. Shang, "Investigation and application of fitting models for centering algorithms in astrometry," *Astrophysics and Space Science*, vol. 366, p. 59, June 2021.

[19] M. Altmann, S. Bouquillon, F. Taris, I. A. Steele, R. L. Smart, A. H. Andrei, C. Barache, T. Carlucci, and S. G. Els, "GBOT - ground based optical tracking of the Gaia satellite," in *Observatory Operations: Strategies, Processes, and Systems V* (A. B. Peck, C. R. Benn, and R. L. Seaman, eds.), (Montréal, Quebec, Canada), p. 91490P, Aug. 2014.

[20] B. Holl, L. Lindegren, and D. Hobbs, "Characterizing the Astrometric Errors in the Gaia Catalogue," *EAS Publications Series*, vol. 45, pp. 117–122, 2010.

[21] L. Lindegren, U. Lammers, D. Hobbs, W. O'Mullane, U. Bastian, and J. Hernández, "The astrometric core solution for the *Gaia* mission: Overview of models, algorithms, and software implementation," *Astronomy & Astrophysics*, vol. 538, p. A78, Feb. 2012.

[22] P. Naulleau, "Optical Lithography," in *Comprehensive Nanoscience and Nanotechnology*, pp. 387–398, Elsevier, 2019.

[23] Y. Wang, M.-H. Chi, J. J.-C. Lou, and C.-Z. Chen, eds., *Handbook of Integrated Circuit Industry*. Springer Nature Singapore, 2024.

[24] C. A. Mack, *Field Guide to Optical Lithography*. SPIE, Jan. 2006.

[25] ThorLabs, *M625L4 SpecSheet*. Available online at https://www.thorlabs.com/thorproduct.cfm?partnumber=M625L4.

[26] ThorLabs, *MWWHL4 SpecSheet*. Available online at https://www.thorlabs.com/thorproduct.cfm?partnumber=MWWHL4.

[27] ThorLabs, *LEDD1B SpecSheet*. Available online at https://www.thorlabs.com/thorproduct.cfm?partnumber=LEDD1B.

[28] ThorLabs, *Visible Achromatic Doublets catalog*. Available online at https://www.thorlabs.com/thorProduct.cfm?partnumber=AC508-400-A&pn=AC508-400-A#4602.

[29] ThorLabs, *Compact Scientific Digital Cameras User Guide*. Available online at https://www.thorlabs.com/thorproduct.cfm?partnumber=CS235MU.

[30] J. R. Janesick, *Photon transfer: DN [lambda]*. Bellingham, Wash: SPIE, 2007. OCLC: ocn140101564.

[31] I. S. McLean, *Electronic Imaging in Astronomy*. Berlin, Heidelberg: Springer Berlin Heidelberg, 2008.

[32] Astropy Collaboration and Astropy Project Contributors, "The Astropy Project: Sustaining and Growing a Community-oriented Open-source Project and the Latest Major Release (v5.0) of the Core Package," *The Astrophysical Journal*, vol. 935, p. 167, Aug. 2022.

Annexes

Annex A

Optical Lithography

A.1 Methodology

A.1.1 Clean Room Equipment and Supplies

- Clean Room: located within the FCFM Physics Department, at Universidad de Chile. The facility is equipped with a Class 1000 clean room, which houses a range of optical lithography equipment, including the MLA100, spin coaters, bench fume hoods, chemical supplies, compressed clean air pistols.
- Maskless Aligner: MLA100 from Heidelberg Instruments, see Figure A.1a. This machine enables the user to expose a computer-aided design (CAD) directly to the substrate without the necessity of a conventional photo-mask. In this instance, the substrate was a glass plate, which was employed as the photo-mask. The Table A.1 below presents the main parameters of the machine.

Table A.1: Optical lithography Maskless machine (MLA) technical specifications. Source: MLA100 Fact Sheet.

Parameter	Value
Minimum Figure Size	1 μm
Light Source	LED: 10 W @ 365 nm
Substrate Size	5x5 mm^2 up to 152x152 mm^2

- Glass Plates: the substrate used as the material into which the photo-mask CAD was exposed and developed; it is illustrated in Figure A.1b. The specifications of its properties are fundamental to understand what can be achieved and how the results can be improved. The untreated glass plates have a length and width of 4 in x 4 in / 101.6 mm x 101.6 mm. The specific details of the material components are presented in Table A.2. These glass plates were acquired from the supplier TELIC Company.

Table A.2: Untreated glass plate technical specifications by the supplier. Source: TELIC Company web page.

	Material	Thickness	Reflectivity
Substrate	Soda Lime Glass	0.9 in / 0.2286 cm	NA
Film	Chrome (Vacuum Deposited)	1100 Å	LRC: 8% @ 450 nm
Photo-resist	AZ1500	1500 Å	NA

- Substrate Cutting Tool: a hand cutting tool for substrates, useful to perform straight cuts on silicon wafers and glass plates; illustrated in Figure A.1c.

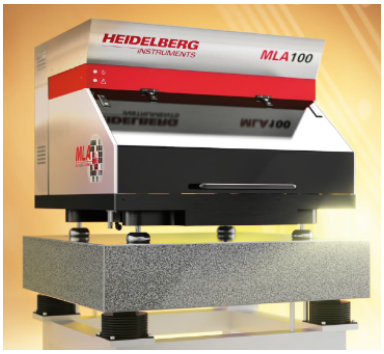

(a) MLA100. Source: MLA100 Fact Sheet.

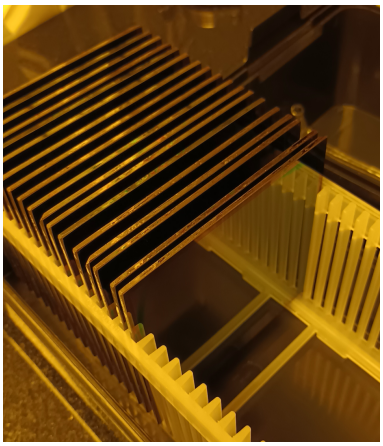

(b) Untreated glass plates from TELIC.

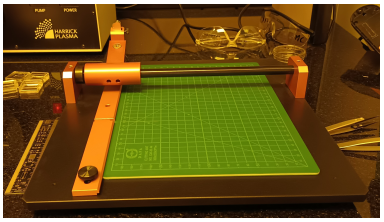

(c) Substrate Cutting Tool.

Figure A.1: Some laboratory equipment, tools, and supplies used in the photo-masks fabrication.

- Tweezers: the glass plates were handled with the utmost care, employing two kind of laboratory tweezers to prevent scratching and the deposition of undesirable materials on the photo-masks. Figure A.2a illustrates the carbon fiber with stainless steel tweezers used for exposure and development process. Figure A.2b illustrates the Teflon tweezers used for the chromium etching process.

(a) Metallic Tweezers.

(b) Teflon tweezers.

Figure A.2: Laboratory Tweezers.

- Laboratory Flasks: the development process and the chromium etching process required mixing and containment of chemicals, including the Developer and the Chromium

Etcher. The flasks utilized were manufactured from Borosilicate glass; they are depicted in Figure A.3 and are listed below:

- 1 Beaker of 100 mL.
- 2 Beaker of 250 mL.
- 2 Graduated Cylinders of 100 mL.
- 1 Erlenmeyer Flask of 250 mL.
- 1 Glass container, large enough to fully immerse the glass plates into the Chromium Etcher.

Figure A.3: Flasks used in the Development and Etching processes.

- Containers: the glass plates must be stored in proper storage boxes and handled with Petri dishes inside the Clean Room. Figure A.4 illustrates in A.4a the custom-made 3D-printed PLA boxes of 55 mm x 55 mm designed to store the photo-masks and in A.4b the gel boxes of 27 mm x 27 mm to store the photo-masks samples used in the calibration process.

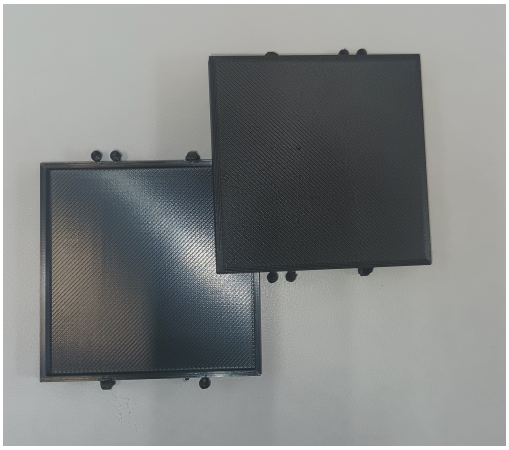

(a) PLA custom-made box, 3D printed. Inside dimensions: 55 mm x 55 mm.

(b) Gel Box. Inside dimensions: 27 mm x 27 mm.

Figure A.4: Containers for photo-masks and samples.

- Compressed air: ideally, the gas should be nitrogen, and breathable air can also be used with the appropriate filters, which was the case in this fabrication process. The compressed air must be delivered by a hand-held pistol.
- Deionized Water: As a universal solvent, it was needed to dilute the Developer. The photo-masks had to be in direct contact to the water, so it was mandatory to avoid any impurities. The purified water was used also to neutralize the chemical action of the Developer and the Chromium Etchant to control the development and etching time, respectively.
- Developer: this chemical is commonly used in optical lithography fabrication processes. Its purpose is to remove the exposed photo-sensitive resin on the substrate. In this case, the developer was prepared using a magnetic mixer, dissolving Sodium Hydroxide (NaOH) into deionized water reaching a volumetric concentration of 2%.
- Chromium Etchant: it is an acidic chromium based solution used to remove metals layers from substrates; commonly used in the electronics industry. A fundamental characteristic of the etchant used, is its Etch Rate of 40 Å/s. The etchant used in the laboratory was acquired from Sigma-Aldrich[1]. It is imperative that this material be handled with the extreme care and that the appropriate personal protective equipment (PPE) be utilized within the clean room environment.
- Microscope: a laboratory-grade *Motic* microscope was employed to visually inspect the resulting photo-masks. The zoom lenses available included: X5, X10, X50. These zoom values allowed the correct inspection of the photo-masks, from searching scratches to verify pinhole diameters and distances.

[1]Sigma-Aldrich webpage: www.sigmaaldrich.com

A.1.2 Fabrication Protocols

Exposure

1. Dress with standard "Clean Room PPE": the first step is to dress with a controlled environment coverall, nitrile gloves, face mask and shoe covers, prior to enter to the clean room.

2. Load the design in the controller PC: in the clean room, load the *.dxf* file CAD design into the MLA Interface computer in the software folder.

3. Prepare MLA: open the compressed air valve, turn on the MLA machine and start the interface software.

4. Prepare exposure job in the software: select the design in the *.dxf* file, input the substrate approximate dimensions (large, width and thickness), select the job mode (dose/defocus test or single exposure), check the software design interpretation, select the XOR box in the Expose Options, save the job and continue with the substrate loading step.

5. Prepare untreated glass plate: using the safe wafer handling tweezers, carefully take one glass plate from the supplier container box and put it on the glass cutting tool aligned with the reference graduated mat and the guiding rails. Therefore, the glass plate must be cut at the desired dimensions, in this case the treated photo-masks needed to be approximately 50[mm]x50[mm] so four equal pieces could be obtained.

6. Load the substrate: in the software select the Load Substrate option, then open the MLA lid and using the tweezers put the glass plate on the MLA exposure bed and properly align. Secure the compressed air lock, close the lid and select the next step in the software. The MLA checks the substrate alignment and dimensions and the check must be accepted.

7. Initiate exposure: the exposure options of Dose and Defocus must be selected and carry out a final checking of the parameters. Finally, start the exposure and wait for the software to announce the accomplishment.

8. Take out the exposed substrate: after the exposure ended, open the MLA lid and turn off the compressed air lock. Take the substrate with the tweezers and leave it on a clean Petri dish.

Development

1. Prepare neutralizer water flask: pour deionized water on a small beaker; it should be large enough to completely submerge the exposed substrate.

2. Measure developer components: using two Graduated cylinders, one for water and one for concentrated developer, measure exactly the amount needed of each liquid to reach the required volumetric concentration.

3. Mix developer components: pour the measured water into an Erlenmeyer flask, subsequently pour the measured concentrated developer. Then, carefully shake the flask for a few seconds to dilute the developer, this is the usable developer liquid for the process.
4. Prepare developer flask: pour the developer liquid into a small beaker; it should be large enough to completely submerge the exposed substrate.
5. Prepare bench fume hood: leave the compressed air pistol, tweezers, stopwatch, water flask, developer flask, and exposed substrate (in its Petri dish) in the bench.
6. Set the stopwatch: set the required time plus ten seconds in the stopwatch and leave it close to the developer flask; this extra time have the purpose to give chance to take the substrate and position it over the developer flask without rushing it.
7. Develop substrate: start the stopwatch, take the developed substrate with the tweezers and submerge it in the developer flask without releasing. Gently shake the substrate until timer stops.
8. Stop developer: remove the substrate from the developer and quickly submerge it into the water flask for at least 30 s.
9. Clean the substrate: finally, remove the substrate from the water and quickly dry it with the compressed air. Leave the clean exposed substrate in the Petri dish.

Etching

1. Prepare neutralizer water flasks: pour deionized water on two small beakers; they should be large enough to completely submerge the developed substrate.
2. Place glass container: clean with deionized water a large glass container, dry it and place it close to the water beakers.
3. Prepare emergency supplies: take the skin shower and eye shower and place them close to the working bench. These are needed in case of a skin or eye direct exposure to the etchant.
4. Prepare Teflon tweezers and paper: place the Teflon tweezers over a clean paper. Also, place generous paper close to the water tap. Metallic tweezers cannot be used due to the acid etchant function of metal removal.
5. Set the stopwatch: this must be set with enough time to submerge the substrate plus time to take the substrate with the tweezers. The suggested time is 45 s.
6. Wear specialized Personal Protective Equipment: before taking the chromium etchant, in addition to the standard clean room PPE, specialized equipment must be wore: chemical resistant gloves, safety googles, chemical apron and face shield.
7. Prepare chromium etchant: take the chromium etchant bottle and carefully pour enough on the glass container. The level of the etchant must be able to completely submerge the substrate.

8. Remove chromium: start the stopwatch and using the Teflon tweezers take the developed substrate to submerge it on the chromium etchant for 30 s to 35 s. Shake the glass container gently to make the etchant flow inside.
9. Stop the etchant process: take out the substrate and now submerge it on the first water flask. Shake gently and leave for at least two minutes.
10. Store the etchant: pour back the chromium etchant to the glass bottle and close the lid. Clean the exterior of the bottle with water, dry, and store.
11. Clean the substrate: take out the substrate and submerge it on the second water flask for at least one minute. Take out again the substrate and dry it quickly with the compressed air pistol. Leave the substrate over a clean paper.
12. Clean and store equipment: each flask and container must be cleaned with water three times. Tweezers also must be cleaned with water.
13. Check work bench: check for residual etchant and clean with water.
14. Remove PPE: remove the dedicated PPE and check for any etchant residue; in case of its presence, remove with paper and clean with water.

A.1.3 Protocols Calibration

Exposure

1. A sample pattern is drawn into a test *.dxf* file. This sample must include the smallest structures to be in the final pattern to expose into the photo-mask and its total area should be no more than a 10% of the substrate usable area.
2. The standard Exposure process is followed and the *dose/defocus test* must be selected.
3. In the final step of the job setup, the Defocus and Dose series parameters are selected.
4. Dose: the distance step size is defined in a proper way to leave enough space to physically separate subsequent iterations; it should be greater than the sample pattern correspondingly dimension (X). The start and end values define the dose range to be tested. The dose step size defines the resolution of values in the dose range.
5. Defocus: the distance step size is defined in a proper way to leave enough space to physically separate subsequent iterations; it should be greater than the sample pattern correspondingly dimension (Y). The start and end values defines the defocus range to be tested. The defocus step size defines the resolution of values in the defocus range.
6. After the Exposure process, the Development process must be followed to observe the results. In consequence, the development time, dose and defocus are variables that might need a few iterations to achieve acceptable results.
7. After the Development process, the substrate must be checked under the microscope. The best results can be identified and cross-reference through the Dose/Defocus setup used. This way, the best configuration can be selected.

Development

1. Take the developer and dilute with deionized water to a proper concentration lower that 2.0%.
2. Expose a substrate sample using a dose/defocus test with previously calibrated parameters. The square design to expose allows to directly observe the results without a microscope.
3. Follow the development protocol with different development times. The minimum development time should not be lower than 2 seconds and the maximum development time should not exceed the 10 seconds.
4. Check the substrate and identify the patterns exposed. They should be easily seen by naked eye. If no pattern is seen, it means the development was not enough and the process must be repeated with longer development times (or higher development concentration).
5. Check the substrate under the microscope. The patterns should be easily differentiated from the non exposed photo-resist.

A.2 Masks Designs

A.2.1 Mask 1

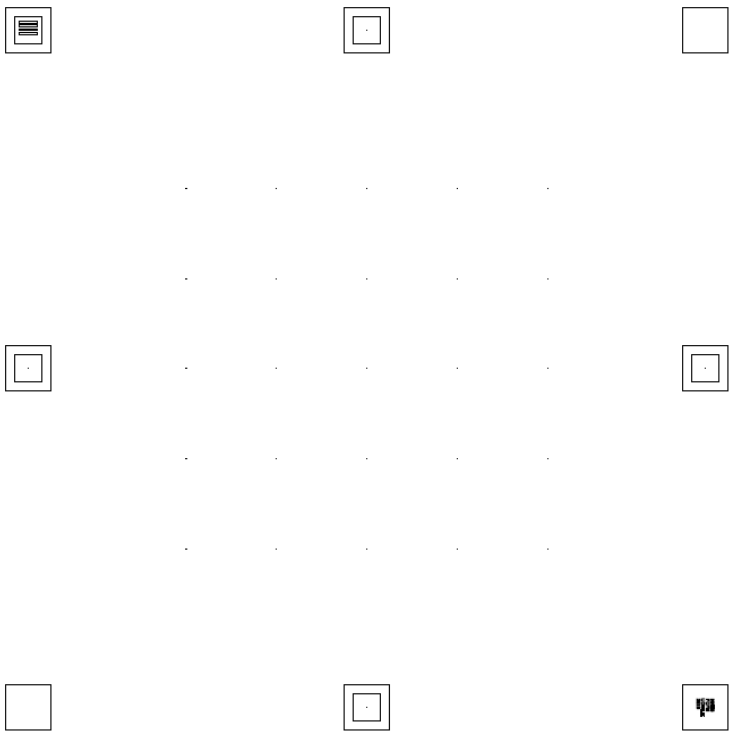

Figure A.5: Mask design 1.

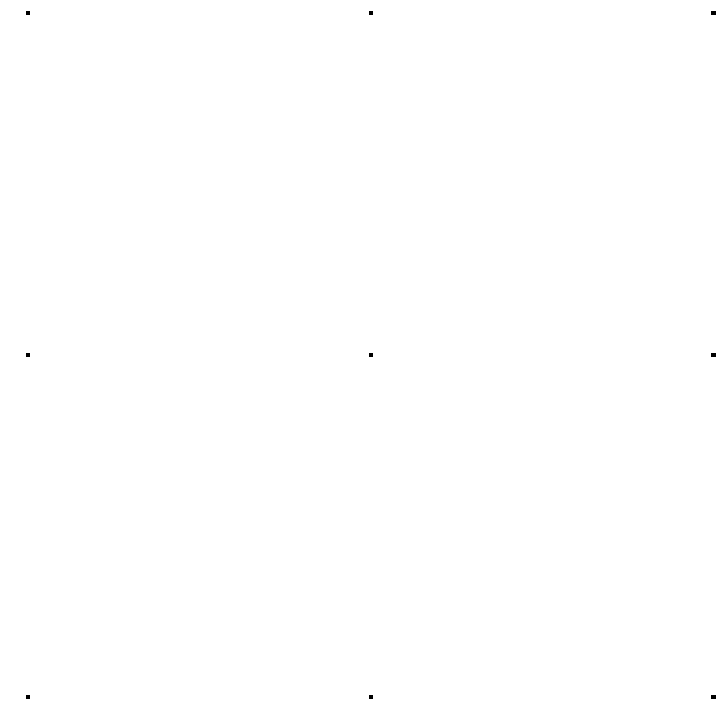

Figure A.6: Mask design 1, zoomed.

A.2.2 Mask 2

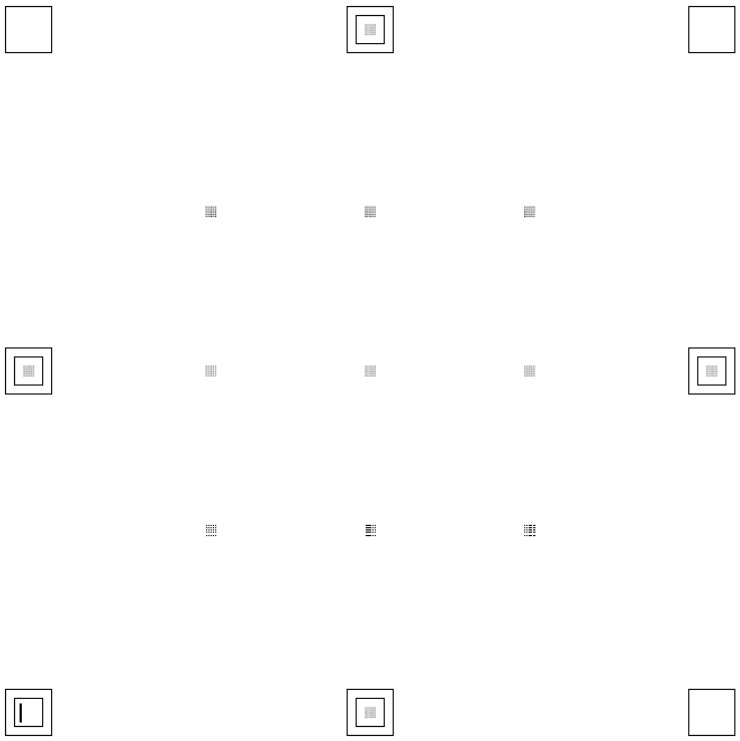

Figure A.7: Mask design 2.

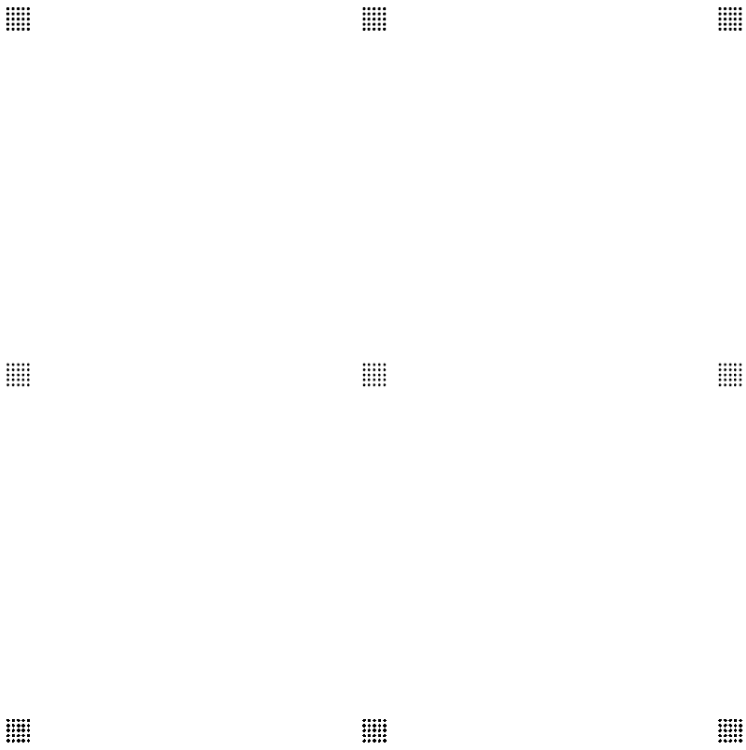

Figure A.8: Mask design 2, zoomed.

A.2.3 Mask 3

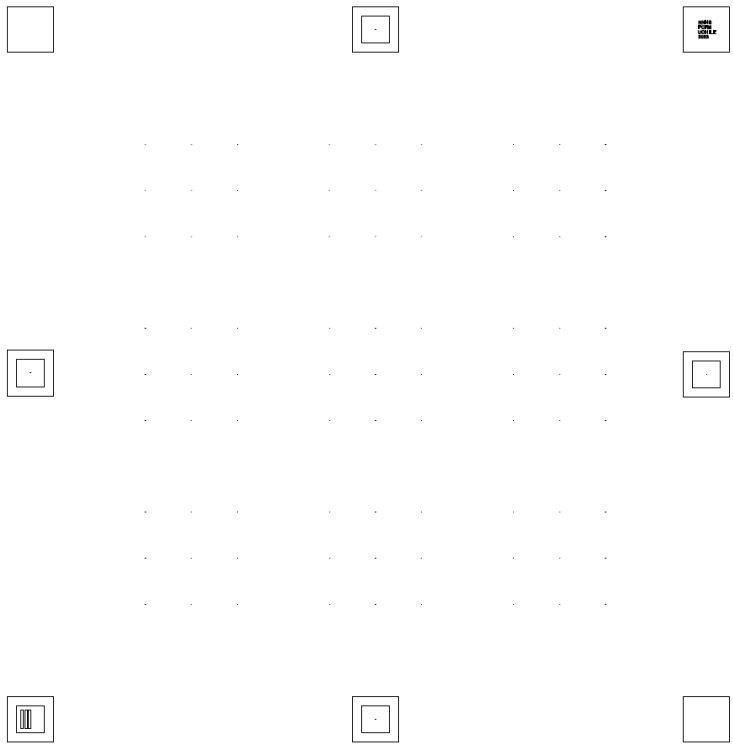

Figure A.9: Mask design 3.

Annex B

Optical Experiment

B.1 Experiment Design

B.1.1 Hardware components and instruments

Light Source

Table B.1: Specifications data from ThorLabs M625L4 SpecSheet.[25]

Specification	Value
Color	Red
Nominal Wavelength	625 nm
Bandwidth (FWHM)	17 nm
Viewing Angle (Full Angle)	80°
Maximum Current (CW)	1000 mA
Electrical Power (max current)	2500 mW
LED Power Output (typical)	920 mW
Forward Voltage (typical)	2.5 V

Table B.2: Specifications data from ThorLabs MWWHL4 SpecSheet.[26]

Specification	Value
Color	Warm White
Correlated Color Temperature	3000 K
Viewing Angle (Full Angle)	120°
Maximum Current (CW)	1000 mA
Electrical Power (max current)	3000 mW
LED Power Output (typical)	640 mW
Forward Voltage (typical)	2.85 V

(a) M625L4. (b) MWWHL4.

Figure B.1: ThorLabs Mounted LEDs. Source: ThorLabs M625L4 and MWWHL4 SpecSheets.[25][26]

LED Driver

Table B.3: Specifications data from ThorLabs LEDD1B SpecSheet.[27]

Specification	Value
LED Current Range	0 - 1200 mA
LED Current Limit Range	200 - 1200 mA
LED Forward Voltage	min. 11 V; typ. 12 V
Current Ripple	8 mA
Current Ripple Frequency	570 kHz
Modulation Input Impedance	10 kΩ

Figure B.2: LEDD1B LED Driver. Source: ThorLabs LEDD1B SpecSheet.[27]

CMOS Detector

Figure B.3: A Kiralux CMOS Compact Scientific Camera by ThorLabs. Source: ThorLabs CS235MU User Guide.[29]

Table B.4: Specifications data from ThorLabs Compact Scientific Digital Cameras User Guide.[29]

Sensor Type	CMOS Monochrome
Number of Active Pixels	1920 (H) X 1200 (V) (∼2.3 MP)
Pixel Size	5.86 μm x 5.86 μm
Optical Format	1/1.2" Format (11251 μm x 7032 μm)
Peak Quantum Efficiency	78% at 500 nm
Dynamic Range	Up to 75 dB
Full Well Capacity	$\geq$ 30,000e$^-$
Shutter Type	Global

Table B.5: Specifications data from ThorLabs Compact Scientific Digital Cameras User Guide.[29]

Exposure Time	0.034 to 15167 ms
Exposure Time resolution	0.020 ms
ADC Resolution	12 bits
Vertical and Horizontal Binning	1 x 1 to 16 x 16
Region of Interest (Width x Height)	92 x 4 Pixels to 1920 x 1200 Pixels, rectangular
Read Noise	$\leq$7.0 e$^-$ RMS
Overlapped Exposures	Frames per Trigger = Continuous Only

B.1.2 Experiment controller

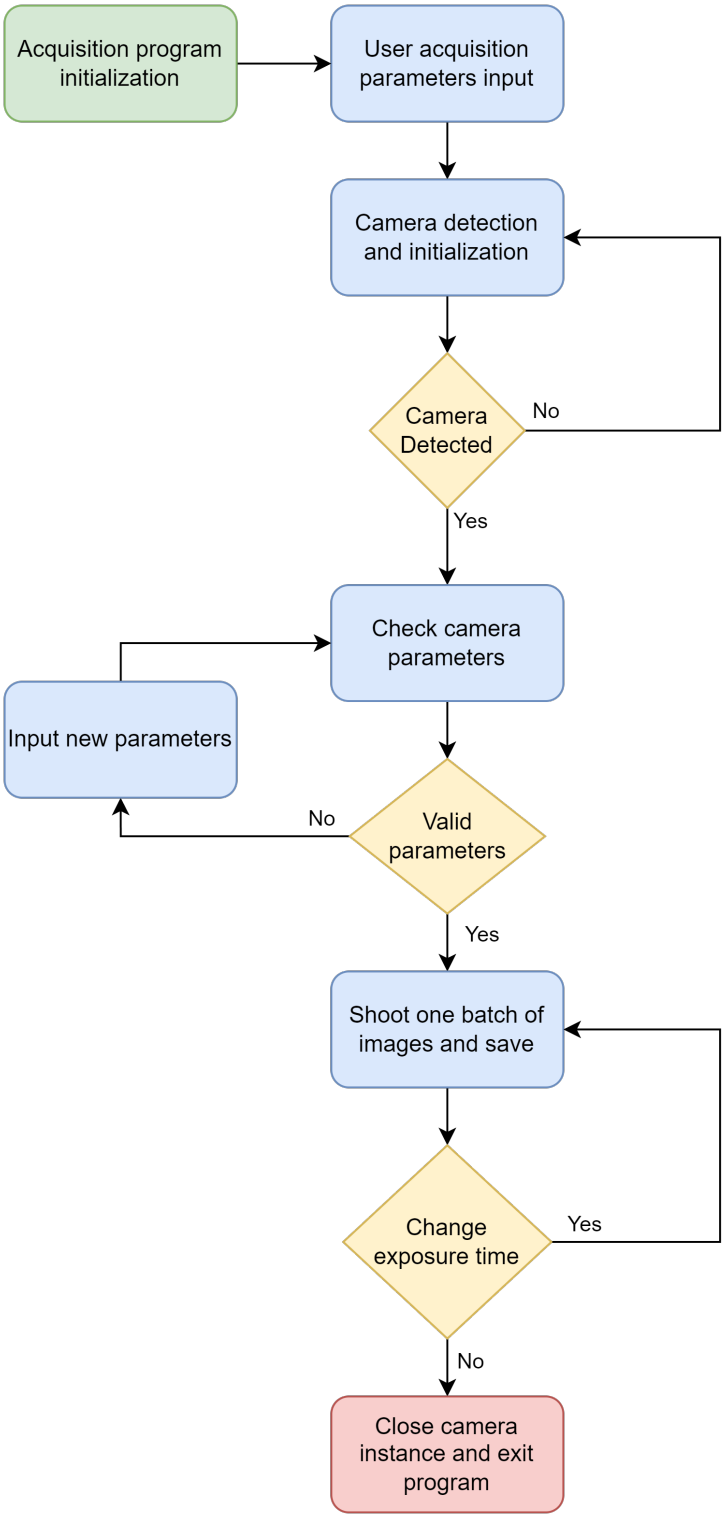

Figure B.4: Vertical presentation of Figure 3.2.

Annex C

Astrometric precision limitation

C.1 Methodology

C.1.1 Cramér-Rao Lower Bound

The following equations define terms used in the computation of the Cramér-Rao Lower Bound:

$$F^j = \frac{\sqrt{2\pi}\sigma}{2}\left[P\left(\frac{y_j^+ - y_c}{\sqrt{2}\sigma}\right) - P\left(\frac{y_j^- - y_c}{\sqrt{2}\sigma}\right)\right] \tag{C.1}$$

$$N_i = \exp\left(-\frac{1}{2}\left(\frac{x_i^+ - x_c}{\sigma}\right)^2\right) - \exp\left(-\frac{1}{2}\left(\frac{x_i^- - x_c}{\sigma}\right)^2\right) \tag{C.2}$$

$$D_i^j = \tilde{B} + \frac{\tilde{F}}{2\pi\sigma^2}F^j I_i \tag{C.3}$$

$$I_i = \frac{\sqrt{2\pi}\sigma}{2}\left[P\left(\frac{x_i^+ - x_c}{\sqrt{2}\sigma}\right) - P\left(\frac{x_i^- - x_c}{\sqrt{2}\sigma}\right)\right] \tag{C.4}$$

The function $P(\cdot)$ in Equations C.1 and C.4 is the Gauss error function, as described by Equation C.5.

$$P(z) = \frac{2}{\sqrt{\pi}}\int_0^z e^{-t^2}dt \tag{C.5}$$

C.2 Results

C.2.1 Star location distributions

Distributions by Method

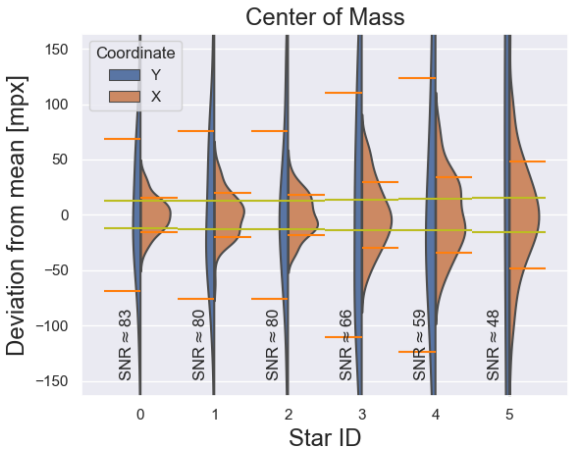

(a) Center of Mass.

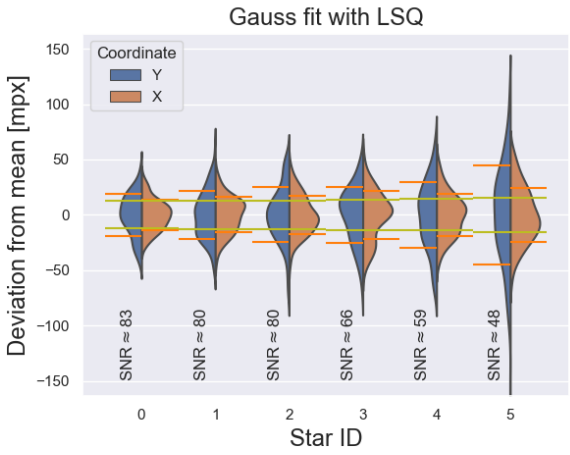

(b) Gauss profile fit by LSQ.

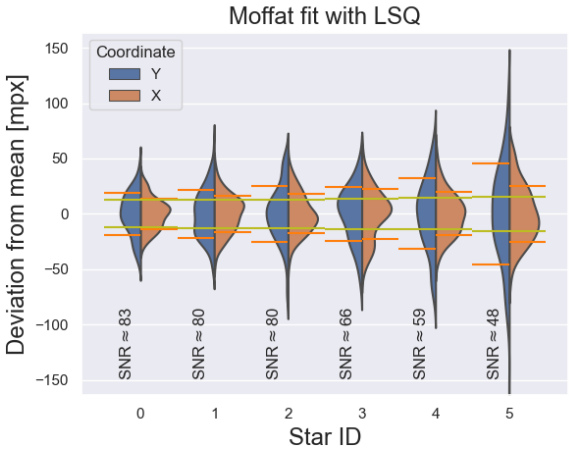

(c) Moffat profile fit by LSQ.

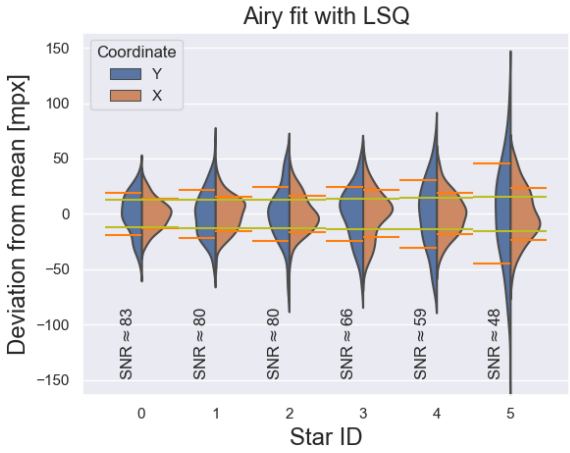

(d) Airy disk profile fit by LSQ.

Figure C.1: Star location distributions by centering method for an exposure time of 90 ms. The green lines represent the CRLB (σ_{CR}) for the corresponding star, while the orange lines represent the experimental precision (σ) of the star location distribution obtained through a centering method.

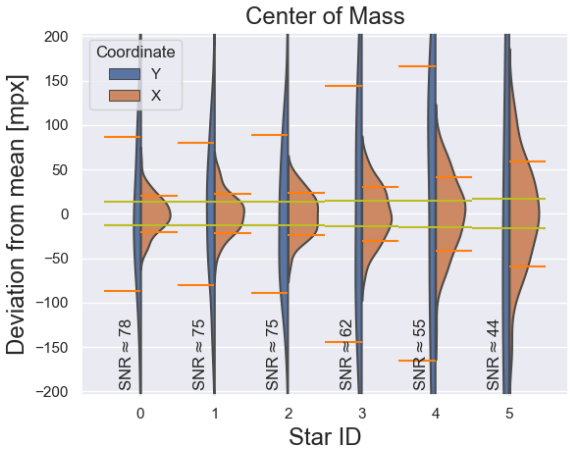

(a) Center of Mass.

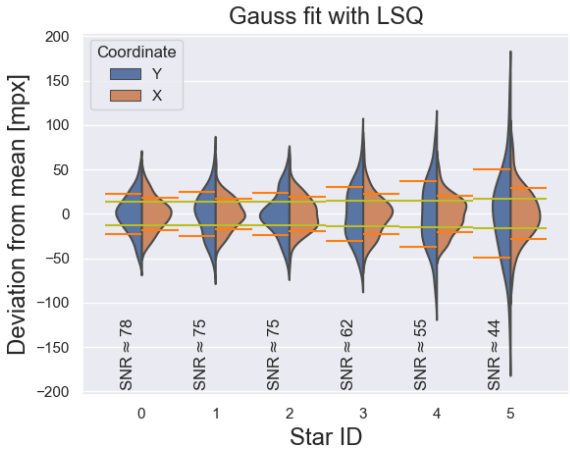

(b) Gauss profile fit by LSQ.

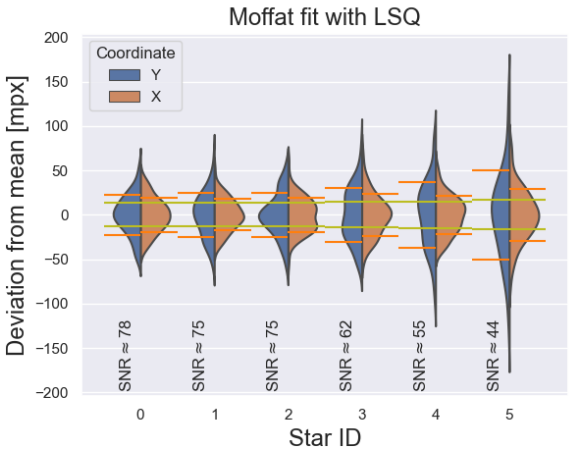

(c) Moffat profile fit by LSQ.

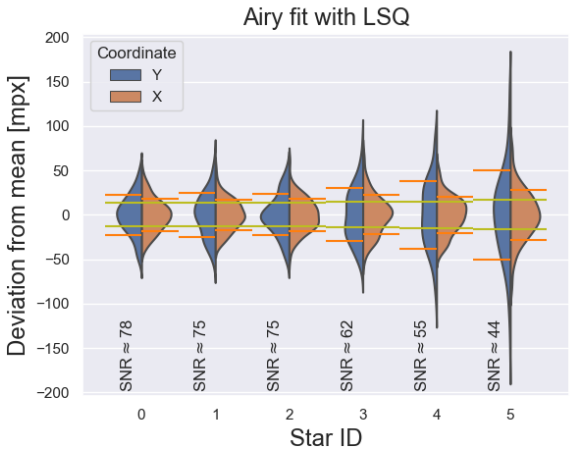

(d) Airy disk profile fit by LSQ.

Figure C.2: Star location distributions by centering method for an exposure time of 80 ms. The green lines represent the CRLB (σ_{CR}) for the corresponding star, while the orange lines represent the experimental precision (σ) of the star location distribution obtained through a centering method.

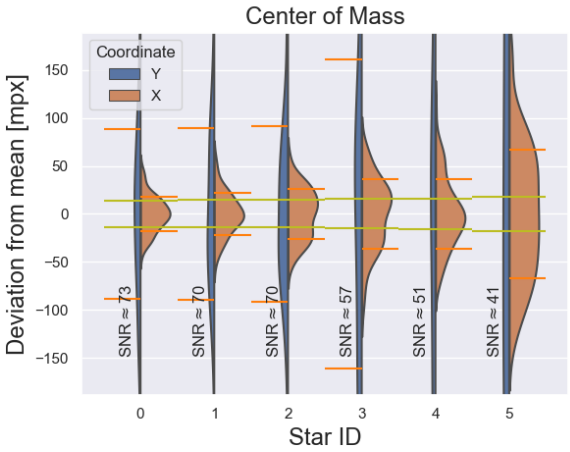

(a) Center of Mass.

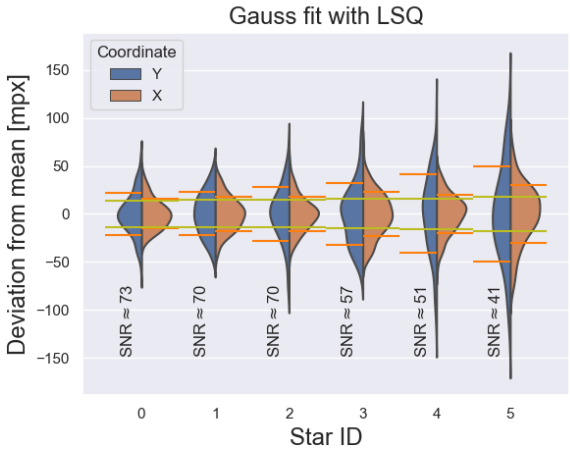

(b) Gauss profile fit by LSQ.

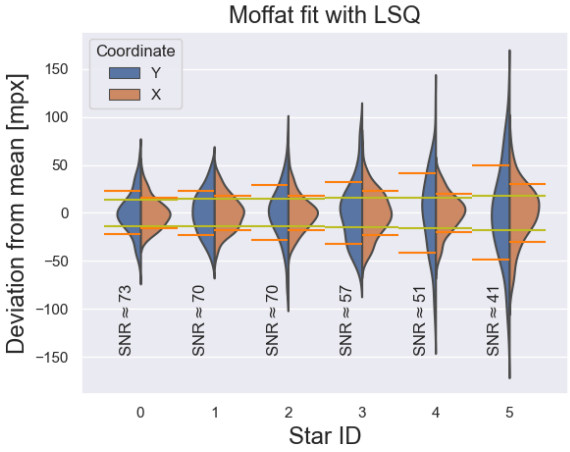

(c) Moffat profile fit by LSQ.

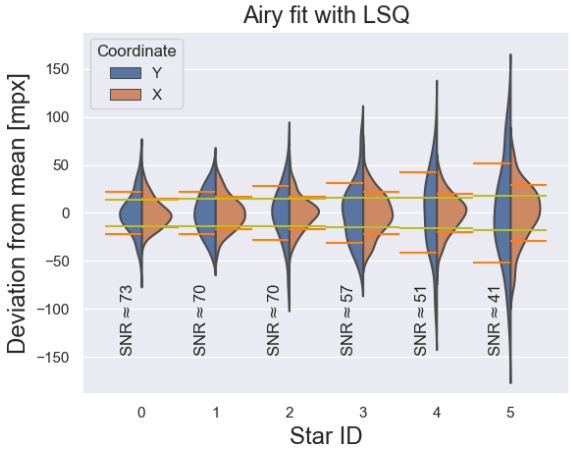

(d) Airy disk profile fit by LSQ.

Figure C.3: Star location distributions by centering method for an exposure time of 70 ms. The green lines represent the CRLB (σ_{CR}) for the corresponding star, while the orange lines represent the experimental precision (σ) of the star location distribution obtained through a centering method.

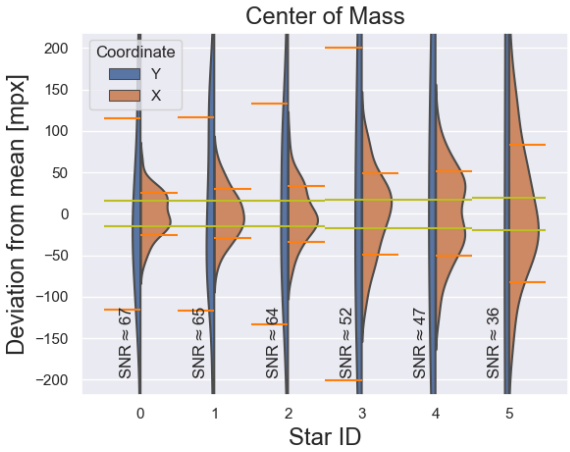

(a) Center of Mass.

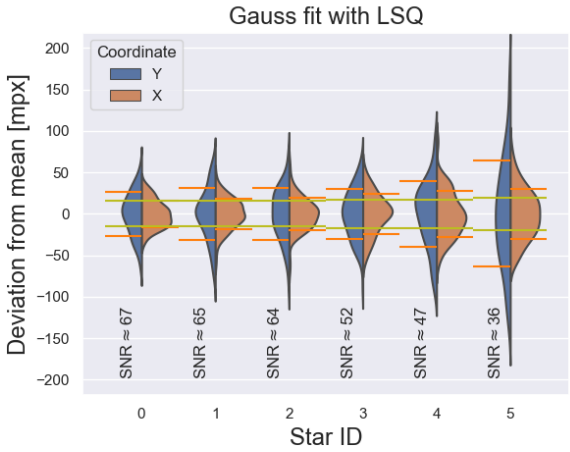

(b) Gauss profile fit by LSQ.

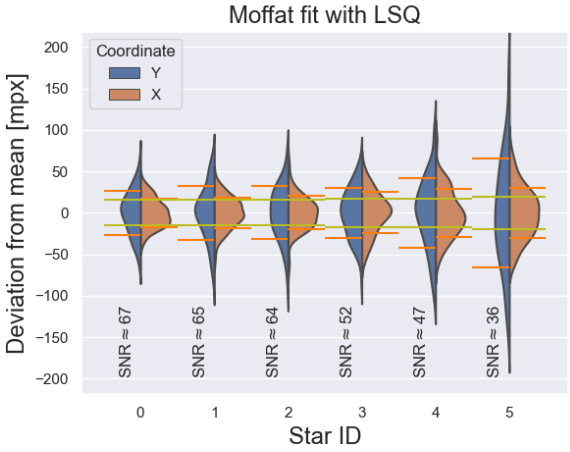

(c) Moffat profile fit by LSQ.

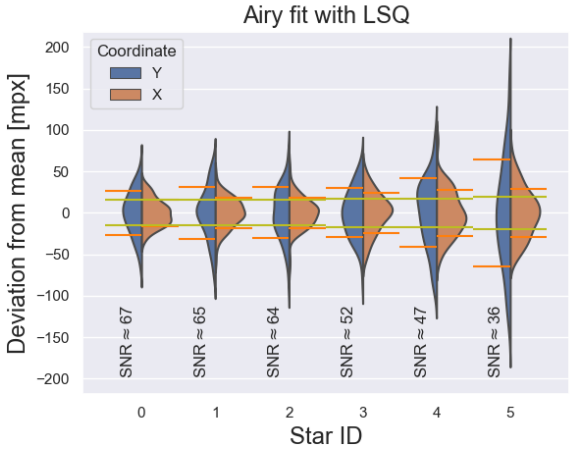

(d) Airy disk profile fit by LSQ.

Figure C.4: Star location distributions by centering method for an exposure time of 60 ms. The green lines represent the CRLB (σ_{CR}) for the corresponding star, while the orange lines represent the experimental precision (σ) of the star location distribution obtained through a centering method.

Location precision

Table C.1: Distribution precision by method to CRLB ratios. Exposure time: 90 ms.

Star	SNR	σ_{CR} [mpx]	σ_{CoM}/σ_{CR}	$\sigma_{Gauss}/\sigma_{CR}$	$\sigma_{Moffat}/\sigma_{CR}$	$\sigma_{Airy}/\sigma_{CR}$
0	83	12.42	1.28	1.10	1.11	1.07
1	80	12.56	1.58	1.27	1.32	1.23
2	80	12.56	1.47	1.38	1.40	1.32
3	66	13.54	2.20	1.59	1.65	1.57
4	60	14.13	2.42	1.36	1.38	1.32
5	48	15.63	3.10	1.57	1.62	1.52

Table C.2: Distribution precision by method to CRLB ratios. Exposure time: 80 ms.

Star	SNR	σ_{CR} [mpx]	σ_{CoM}/σ_{CR}	$\sigma_{Gauss}/\sigma_{CR}$	$\sigma_{Moffat}/\sigma_{CR}$	$\sigma_{Airy}/\sigma_{CR}$
0	78	13.21	1.52	1.40	1.44	1.38
1	76	13.35	1.66	1.30	1.33	1.28
2	75	13.34	1.76	1.44	1.44	1.37
3	62	14.40	2.11	1.57	1.64	1.53
4	56	15.02	2.78	1.36	1.41	1.36
5	45	16.63	3.54	1.73	1.75	1.70

Table C.3: Distribution precision by method to CRLB ratios. Exposure time: 70 ms.

Star	SNR	σ_{CR} [mpx]	σ_{CoM}/σ_{CR}	$\sigma_{Gauss}/\sigma_{CR}$	$\sigma_{Moffat}/\sigma_{CR}$	$\sigma_{Airy}/\sigma_{CR}$
0	73	14.13	1.30	1.09	1.11	1.06
1	71	14.28	1.52	1.23	1.28	1.21
2	70	14.27	1.81	1.25	1.27	1.20
3	58	15.41	2.33	1.48	1.50	1.41
4	52	16.07	2.24	1.25	1.24	1.23
5	41	17.82	3.77	1.69	1.69	1.64

Table C.4: Distribution precision by method to CRLB ratios. Exposure time: 60 ms.

Star	SNR	σ_{CR} [mpx]	σ_{CoM}/σ_{CR}	$\sigma_{Gauss}/\sigma_{CR}$	$\sigma_{Moffat}/\sigma_{CR}$	$\sigma_{Airy}/\sigma_{CR}$
0	67	15.29	1.69	1.06	1.09	1.04
1	65	15.46	1.91	1.18	1.20	1.16
2	65	15.45	2.16	1.27	1.30	1.20
3	53	16.71	2.91	1.44	1.49	1.43
4	47	17.40	2.93	1.60	1.65	1.60
5	37	19.32	4.28	1.54	1.56	1.52

Location by Frame

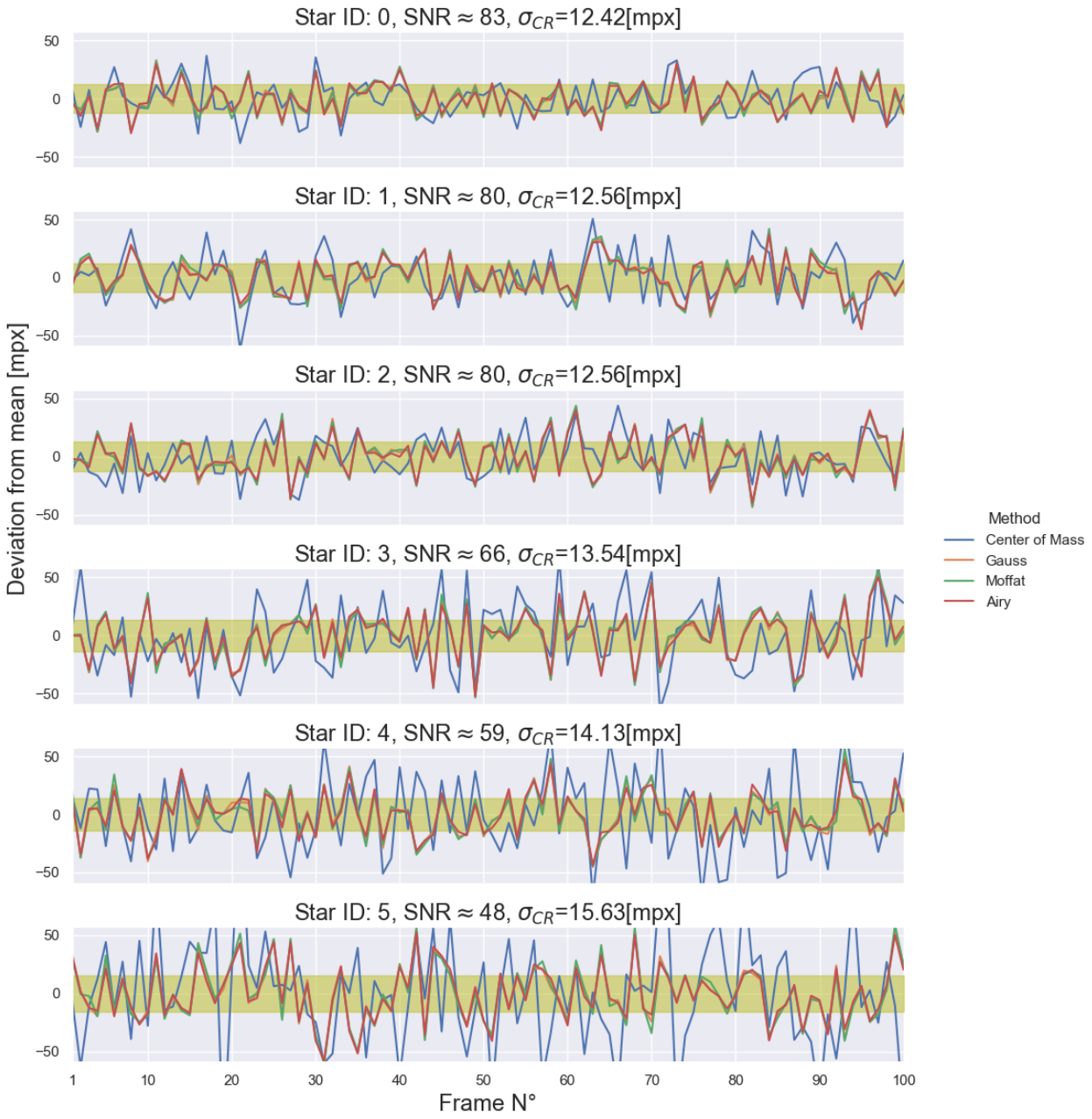

Figure C.5: Location deviation of stars from its corresponding mean value. The green strips covers the $\pm\sigma_{CR}$ range. It is easily noted that lowering the SNR results in more dispersed location. Exposure time: 90 ms.

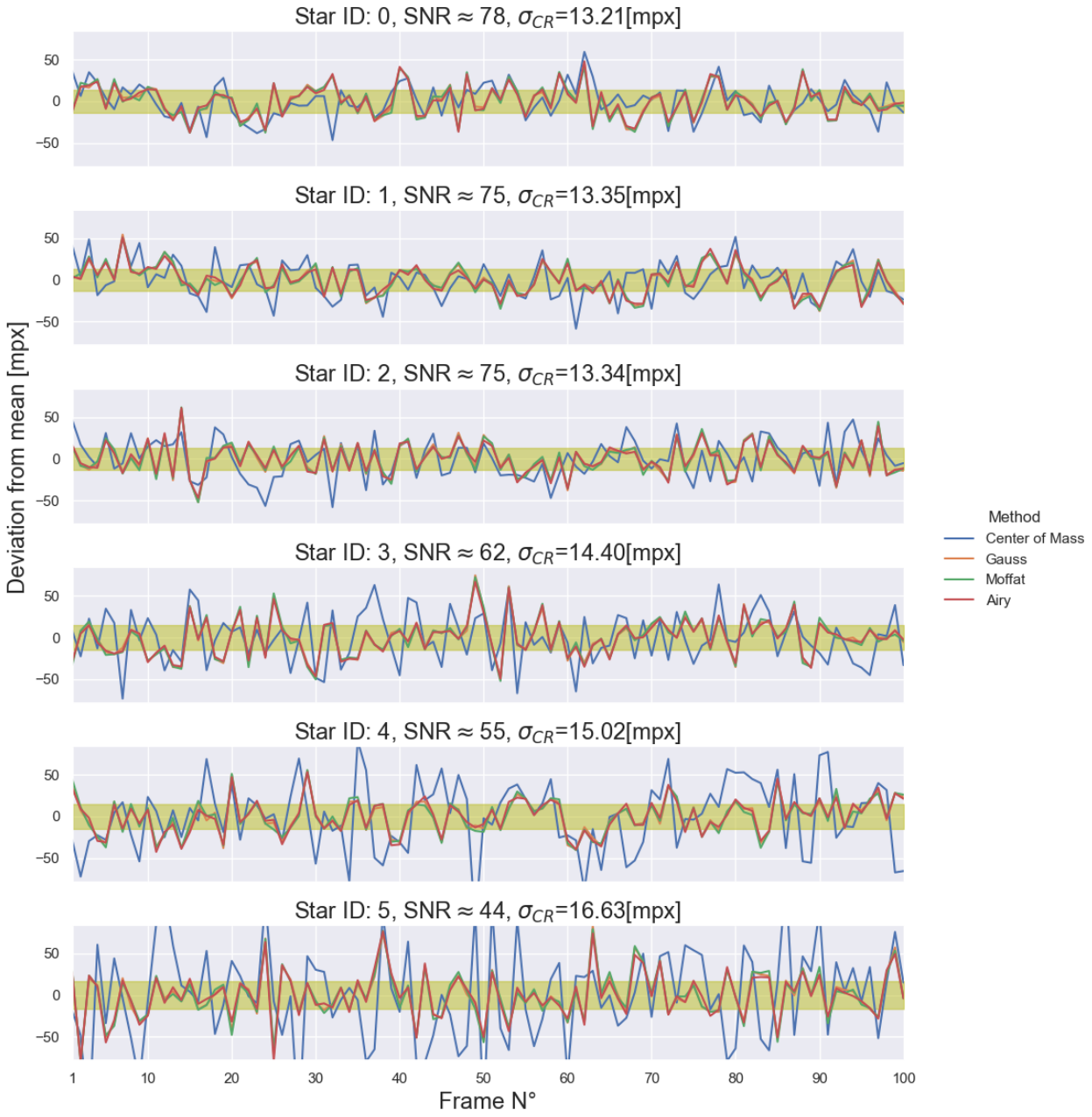

Figure C.6: Location deviation of stars from its corresponding mean value. The green strips covers the $\pm\sigma_{CR}$ range. It is easily noted that lowering the SNR results in more dispersed location. Exposure time: 80 ms.

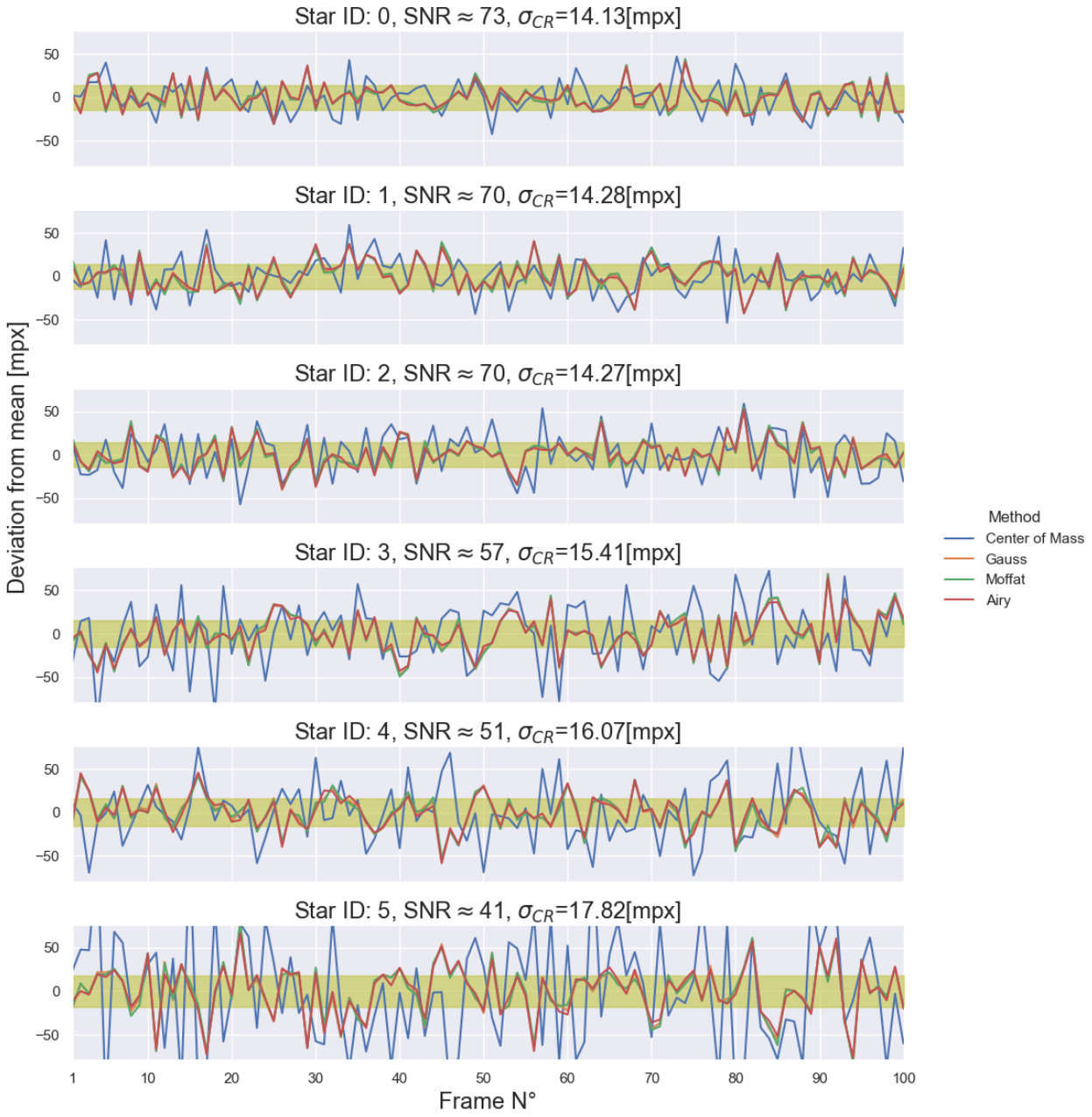

Figure C.7: Location deviation of stars from its corresponding mean value. The green strips covers the $\pm\sigma_{CR}$ range. It is easily noted that lowering the SNR results in more dispersed location. Exposure time: 70 ms.

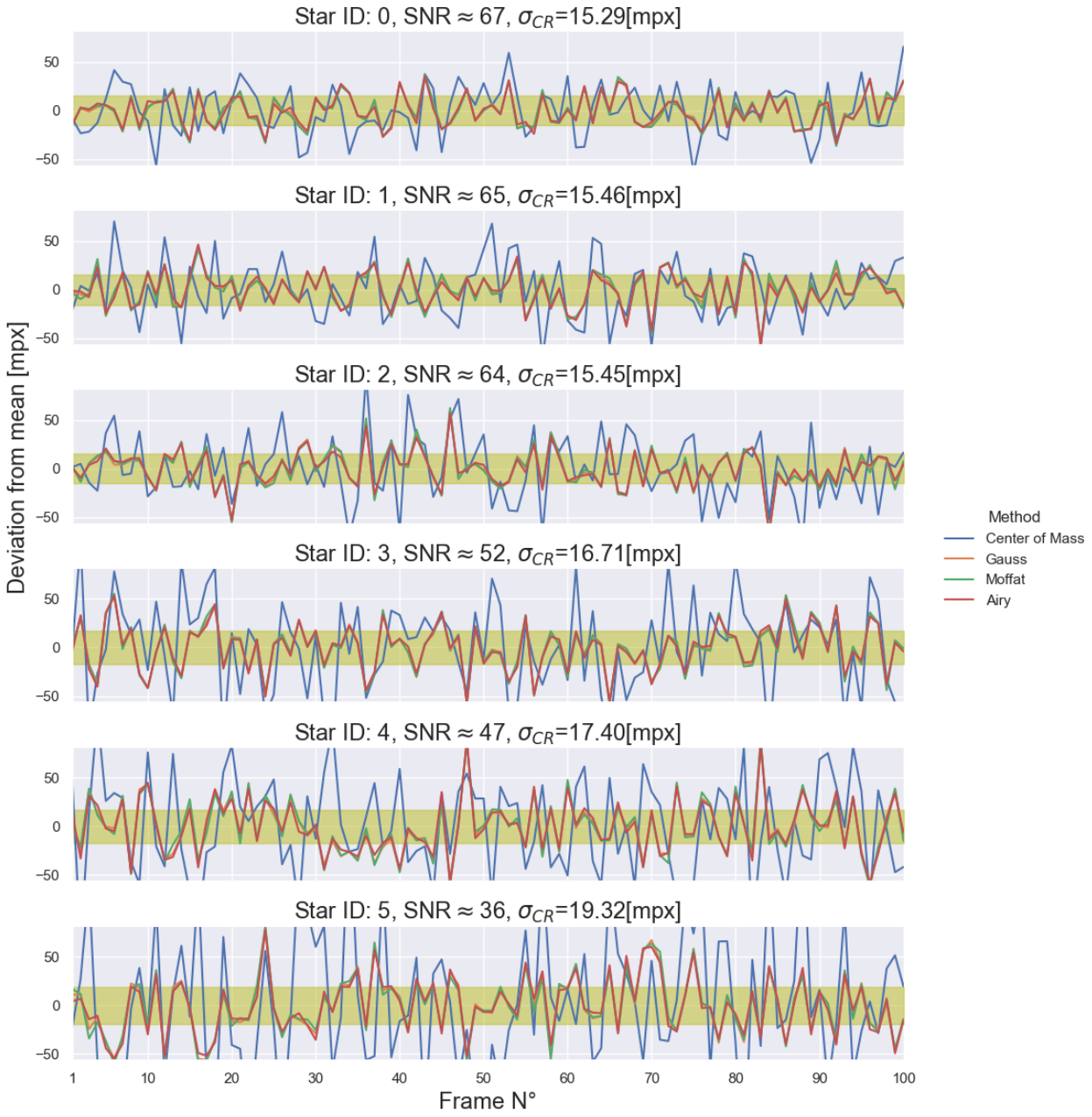

Figure C.8: Location deviation of stars from its corresponding mean value. The green strips covers the $\pm\sigma_{CR}$ range. It is easily noted that lowering the SNR results in more dispersed location. Exposure time: 60 ms.

C.2.2 CRLB relation to SNR and accumulated Signal

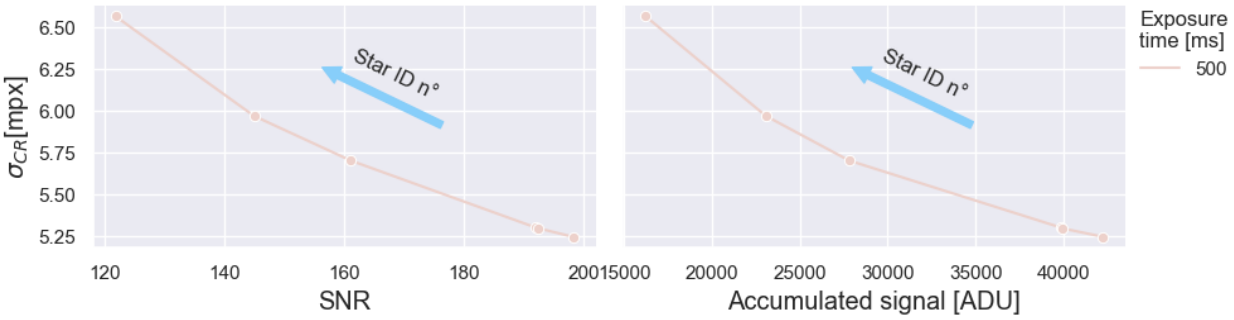

Figure C.9: Each point represents the CRLB in function of a representative value of the 500 ms dataset: mean SNR, and mean Accumulated signal counts, for the corresponding one hundred frames image stack.

Annex D

Extended abstract

Estudio de la limitación de la precisión astrométrica mediante un experimento de campo estelar lejano artificial

En astrometría, el límite de precisión de un instrumento que observa un objeto celeste puede servir para indicar si se puede investigar la validez de cierta hipótesis. Para estudiar este concepto, se empleó un esquema de experimento óptico previamente diseñado para comparar la precisión astrométrica empírica con el límite de precisión astrométrica teórico, el "Límite Inferior de Cramér-Rao"; esta comparación amplía la comprensión de la relación entre ambos. Además, se sugiere una modificación al experimento óptico.

Se realizó un experimento óptico para simular un campo estelar lejano artificial. A continuación se analizaron las imágenes de las fuentes luminosas puntuales. La ubicación central de las estrellas artificiales se calculó utilizando cuatro algoritmos diferentes que se mencionan habitualmente en la literatura, para obtener la precisión astrométrica empírica. El límite inferior se calculó utilizando las fórmulas mencionadas en estudios anteriores sobre el tema. Se realizó un análisis comparativo entre la precisión empírica y su límite teórico, utilizando los datos de las imágenes capturadas. La mejora propuesta para el experimento óptico se implementó en una de las configuraciones para recopilar datos sobre su rendimiento.

La localización de cada estrella se calculó mediante los algoritmos propuestos, lo que dio lugar a datos estadísticos para siete conjuntos de datos diferentes con un tamaño de muestra de cien. El límite de precisión empírica presentó valores cercanos al "Límite Inferior" estimado y, en determinadas condiciones, incluso alcanzó este límite teórico. Se observó que la señal acumulada de un objeto observado domina el "Límite Inferior" en proporcionalidad inversa, en condiciones de bajo fondo. En cuanto a la mejora propuesta para el experimento, los resultados no fueron satisfactorios debido a la baja reflectancia de la foto-máscara.

Se investigó la relación entre la precisión astrométrica empírica y su límite teórico, y se llegó a la conclusión de que la máxima precisión astrométrica de localización alcanzable puede estimarse utilizando la información previa comúnmente disponible sobre el instrumento

astronómico y el objeto celeste bajo estudio; se confirmó que la precisión experimental se aproxima a este límite. La mejora propuesta al experimento no cumplió las expectativas, pero las conclusiones al respecto llevaron a formular nuevos cambios que pueden probarse en futuras realizaciones con un resultado prometedor.

An astrometric precision limitation study using an artificial far-stellar field experiment

In astrometry, the precision limit of an instrument observing a celestial object may serve to indicate whether the validity of a hypothesis can be investigated. To study this concept, a previously designed optical experiment scheme was employed to compare the empirical astrometric precision to the theoretical astrometric precision limit, the Cramér-Rao Lower Bound; this comparison expands the understanding of the relationship between the two. In addition, a modification is suggested for the optical experiment.

An optical experiment was conducted to simulate an artificial far-stellar field. The images of point-like light sources were then analyzed. The artificial stars location was calculated using four different algorithms that are commonly mentioned in the literature to obtain empirical astrometric precision. The "Lower Bound" was calculated using the formulas reported in previous studies in the field. A comparative analysis was conducted between the empirical precision and its theoretical limit, using the data from the images captured. The proposed improvement to the optical experiment was implemented in one of the setups to gather data about its performance.

The star location was computed through the proposed algorithms, resulting in statistical data for seven different datasets with a sample size of one hundred. The empirical precision limit presented values that were near the estimated Lower Bound, and in certain conditions, even reached this theoretical limit. It was observed that the accumulated signal of an observed object dominates the Lower Bound in inverse proportionality, under low background conditions. With regard to the proposed improvement to the experiment, the results were not satisfactory due to the low reflectance of the photo-mask.

The relationship between empirical astrometric precision and its theoretical limit was investigated. It was concluded that the maximum attainable astrometric location precision can be estimated by using commonly available prior information about the astronomical instrument and the celestial object under study; it was confirmed that the experimental precision approaches this limit. The proposed improvement to the experiment did not meet the expectations, but the conclusions about it led to formulate new changes that can be tested in future realizations with a promising outcome.